



# Politecnico di Bari

Repository Istituzionale dei Prodotti della Ricerca del Politecnico di Bari

Combustion processes modeling: numerical investigations of an engine equipped with a Turbulent Jet Ignition system and of a scramjet combustor

This is a PhD Thesis

*Original Citation:*

*Availability:*

This version is available at <http://hdl.handle.net/11589/240300> since: 2022-06-04

*Published version*

<http://hdl.handle.net/11589/240300>  
DOI: 10.60576/poliba/iris/cassone-egidio\_phd2022

*Terms of use:*

Altro tipo di accesso

(Article begins on next page)



Politecnico  
di Bari

Department of Mechanics, Mathematics and Management  
MECHANICAL AND MANAGEMENT ENGINEERING

Ph.D. Program

SSD: ING-IND/08–FLUID MACHINERY

**Final Dissertation**

---

Combustion processes modeling:  
numerical investigations of an engine  
equipped with a Turbulent Jet Ignition  
system and of a scramjet combustor

---

by

Egidio Cassone:

---

Referees:

Prof.ssa Emma Frosina

Prof.ssa Teresa Castiglione

Supervisors:

Prof. Riccardo Amirante

Prof. Elia Distaso

*Coordinator of Ph.D Program:*

*Prof. Giuseppe Pompeo Demelio*

---

To my family and to my son, Lorenzo. I wish to leave him a better world and to transmit him the wish to know.

*It doesn't matter how beautiful your theory is, it doesn't matter how smart you are. If it doesn't agree with experiment, it's wrong.*

Richard Feynman

The present work contains all the relevant results arising from the three years PhD course. The research activity was focused on the numerical modeling of reacting flow and particular attention was paid at combustion. The main research activities were, indeed, related to the analysis of a Turbulent Jet Ignition device for spark ignition engines and to the analysis of the mixing and combustion processes involved in a scramjet combustor, fueled with Hydrogen, for hyper-sonic flight proposal.

The thesis opens with a general introduction on combustion and on its importance in energy application at the present day. Moreover, the main alternatives are introduced and rapidly discussed, concluding that combustion will maintain a crucial role in the transition period toward carbon-neutrality.

Then, a rapid introduction on combustion modeling is performed. Essentially, combustion can be numerically approached by solving all the chemical reaction describing the phenomena (e.g., the fuel oxidation). Anyway, such approach often requires a high amount of computing resources. An alternative is represented by the so-called simplified chemistry model, as the G-equation model here also employed. Such a model employs an analytical correlation to describe the flame propagation speed, avoiding the need of excessively dense meshes but is only suitable for pre-mixed combustion (thus not employable in the scramjet simulations). The numerical simulations were performed by means of a commercial software, CONVERGE CFD, with the inclusion of some User Defined Functions. The validations of the developed numerical models were performed against selected sets of experimental data presented in Chapter 3-The experimental data. Here the experimental setups are described, and the acquired data analyzed. Regarding the engine, an optically accessible research engine was employed. Such an engine, fueled with Methane, has been tested both with the TJI apparatus and with a standard spark plug. The experiments were carried out in similar conditions (e.g., equivalence ratio, throttle and engine speed). In this way, a direct comparison between the experiments could be performed. The experimental campaign was carried out by our partner, Istituto motoristico CNR, in Naples. On the other hand, the scramjet data were acquired in the high enthalpy shock tunnel of Gottingen, simulating a flight at  $M=7.4$  at an altitude of 28 km, and retrieved from literature.

Chapter 4-Modeling approach describes the modelling approach for the engine, modeled both with and without the TJI apparatus, and the scramjet combustor.

Chapter 5-Engine simulations results and 6-Scramjet simulations results present and discuss the results obtained by the numerical simulations. In particular, a detailed analysis of the main phenomena characterizing a TJI system is performed in Chapter 5. Such an analysis was aimed at providing new insights on the main charge ignition and on the overall combustion evolution. The working phases of the pre-chamber were investigated singularly with a particular attention on the pre-chamber scavenging, filling and mixing. Then, the combustion stages were investigated, focusing the attention on the species conversion pathways in the pre and main chamber. Such an analysis concluded that the rich combustion occurring in the pre-chamber makes available a great amount of energy and reactive material for the main charge ignition. Indeed, the main charge ignition is obtained by a synergic effect of both chemical and thermodynamic properties of the jets arising from the pre-chamber. Finally, a comparison between the computed emissions of both engines is performed, concluding that the pre-chamber engine behaves, globally, better in respect to the standard.

The scramjet simulations results are given in the next Chapter, Chapter 6-Scramjet simulations results. After an overall analysis showing some of the complex flow features typical of crossflow injections, deeper investigations on the flow field structure and on the combustion development and evolution are performed. In cross-flow injection combustor, the mixture ignition and the combustion stability are strictly related to the

mixing between fuel and oxidizer. The coherent structures proper of this kind of flow-fields plays crucial roles in achieving reasonable mixing times favorable for mixture ignition. Moreover, a recirculation bubble forming ahead of the injector seems to be responsible for flame stabilization.

Globally, the present work offered deep investigations of the phenomena involved in the operation of a TJI system for spark ignition internal combustion engines and on the mixing, ignition and combustion phases of a scramjet combustor. Much of the involved phenomena were analyzed by multiple perspective with the aim of offering an holistic point of view on the various (and quite un-conventional) events involved in a Turbulent Jet Ignition system and in a scramjet combustor.

Above the conclusions given in Chapter 5 and 6, the author's sake is purposing food for thought for future works, research and analysis on internal combustion engines, scramjets and fluid machinery in general.

Combustion is at the base of many energy production processes and, today like never before, research is involved in maximizing combustion efficiency and reducing the pollution deriving from it. Thanks to the high specific energy of fuels, combustion processes will still have a role in the future, especially in the transportation sector. Therefore, increasing Internal Combustion Engines (ICE) efficiency and reducing their polluting emissions has become an imperative object. Among all the non-conventional ignition systems that are being purposed by research, Turbulent Jet Ignition (TJI) seems to be one of the most promising capable to achieve leaner combustion and higher thermal efficiency in spark ignited engine. In a TJI system a jet of high-energy reactive gases is generated by means of a pilot combustion in a pre-chamber and used to initiate the main combustion event in the cylinder. By virtue of this, TJI devices are able to achieve a more stable combustion also with more problematic fuels, such as Methane.

In the present work, a deep and innovative analysis approach is purposed and applied to a TJI prototype installed on a Methane fueled optically accessible spark ignition research engine. By means of 3D numerical simulations, the behavior of such engine has been monitored and analyzed over a whole engine cycle. Attention has been paid especially on the scavenging, filling and combustion phases in the pre-chamber. Moreover, the jets characteristics and species distribution and evolution are analyzed in order to study the reactive-jet-induced ignition mechanism of the main charge and the associated fuel conversion mechanism. Attention is also given to pollutant species formation and in-cylinder distribution. The purposed approach allowed the characterization of the main phenomena involved in the operation of such system as well as the evaluation of different parameters, such as combustion duration, flame evolution and pre-chamber ignition energy release. The same engine without the pre-chamber has been modeled as well and used for comparison. The bench test data recorded by Istituto Motori di Napoli CNR were employed both to tune the model and to compare the performance increase due to the TJI device.

Parallely, CFD studies on a scramjet combustor for hypersonic flight purposes fueled with Hydrogen were also carried out. After having validated the model against a set of in-flight representative data, the main physical mechanisms involved in the mixing and combustion processes were analyzed. Moreover, various information about the complex flow patterns and structure were retrieved.

# Contents

---

|  |             |
|--|-------------|
| <b>ACRONYMS .....</b>  | <b>III</b>  |
| <b>LIST OF FIGURES .....</b>   | <b>IV</b>   |
| <b>LIST OF TABLES .....</b>  | <b>VIII</b> |
| <b>1. INTRODUCTION .....</b>   | <b>1</b>    |
| 1.1 Recent trend in Internal Combustion Engine research: the Turbulent Jet Ignition system ..... | 1           |
| 1.2 Hydrogen combustion: scramjets applications for hypersonic flights .....                     | 3           |
| <b>2. FUNDAMENTALS OF COMBUSTION MODELING.....</b>   | <b>4</b>    |
| 2.1 The species transport equation .....   | 4           |
| 2.2 The scalar transport equation .....  | 4           |
| 2.3 Turbulence transport equation .....  | 5           |
| 2.3.1 RANS turbulence modeling: the <i>RNG</i> $k - \varepsilon$ model .....                     | 5           |
| 2.3.2 LES turbulence modeling: the Dynamic Smagorinsky Sub Grid Scale model .....                | 6           |
| 2.4 Combustion modeling .....  | 7           |
| 2.4.1 SAGE detailed chemical kinetic solver.....   | 8           |
| 2.4.2 Combustion modeling of premixed flames: the G-equation approach.....                       | 9           |
| <b>3. THE EXPERIMENTAL DATA .....</b>  | <b>12</b>   |
| 3.1 Experimental Engine data .....   | 12          |
| 3.2 Experimental scramjet data .....   | 16          |
| 3.3 Conclusions of chapter 3 .....   | 19          |
| <b>4. MODELING APPROACH.....</b>   | <b>20</b>   |
| 4.1 Engine model setup.....  | 20          |
| 4.1.1 The crevice model .....  | 22          |
| 4.2 Scramjet model setup .....   | 24          |
| 4.3 Conclusions of chapter 4 .....   | 26          |

|  |           |
|--|-----------|
| <b>5. ENGINE SIMULATIONS RESULTS.....</b>                | <b>27</b> |
| 5.1 The standard engine .....                            | 27        |
| 5.2 The pre-chamber engine .....                         | 28        |
| 5.2.1 Preliminary analysis.....                          | 29        |
| 5.2.2 The filling and scavenging phases .....            | 34        |
| 5.2.3 The mixing phase.....                              | 35        |
| 5.2.4 Combustion phase.....                              | 37        |
| 5.2.5 The expulsion phase and pollutant production ..... | 49        |
| 5.2.6 Compressibility effects .....                      | 52        |
| 5.3 Engine out emissions .....                           | 53        |
| 5.4 Flame shape and radius evaluation .....              | 54        |
| 5.5 Future work outlook .....                            | 58        |
| 5.6 Conclusions of chapter 5 .....                       | 62        |
| <b>6. SCRAMJET SIMULATIONS RESULTS .....</b>             | <b>63</b> |
| 6.1 Overall flow analysis .....                          | 63        |
| 6.2 Detailed flow analysis .....                         | 67        |
| 6.3 Combustion regime.....                               | 72        |
| 6.4 Conclusions of chapter 6 .....                       | 80        |
| <b>7. SUMMARY AND OUTLOOK .....</b>                      | <b>81</b> |
| <b>8. BIBLIOGRAPHY .....</b>                             | <b>83</b> |

## Acronyms

---

|       |                                     |
|-------|-------------------------------------|
| AMR   | Adaptive Mesh Refinement            |
| ATDC  | After the Top Dead Center           |
| BTDC  | Before the Top Dead Center          |
| CAD   | Crank Angle Degree                  |
| CVP   | Counter rotating Vortex Pair        |
| EVO   | Exhaust Valve Opening               |
| HRR   | (net/apparent)Heat Release Rate     |
| IaHRR | Integrated apparent Heat Released   |
| ICE   | Internal Combustion Engine          |
| IMEP  | Indicated Mean Effective Pressure   |
| IVC   | Intake Valve Closing                |
| LES   | Large Eddy Simulations              |
| LHS   | Left Hand Side                      |
| PFI   | Port-Fuel Injection                 |
| RANS  | Reynolds Averaged Navier-Stokes     |
| RHS   | Right Hand Side                     |
| RNG   | ReNormalized Group turbulence model |
| SGS   | Sub-Grid Scale                      |
| SI    | Spark Ignition                      |
| SOI   | Start Of Injection                  |
| TFI   | Takeno Flame Index                  |
| TJI   | Turbulent Jet Ignition              |
| WOT   | Wide-Opened Throttle                |

## List of Figures

|  |    |
|--|----|
| Figure 1 - Scheme of a premixed turbulent flame [89] .....   | 7  |
| Figure 2 - Flow diagram for stoichiometric Methane oxidation [91] .....  | 9  |
| Figure 3 - Conceptual structure of a flame with the G-equation approach .....  | 10 |
| Figure 4 - The pre-chamber assembly .....  | 12 |
| Figure 5 - Representation of the optical setup.....  | 13 |
| Figure 6 - Experimental pressure and HRR traces .....  | 14 |
| Figure 7 - Experimental flame visualizations. Top, the standard engine; Bottom the pre-chamber engine. .   | 15 |
| Figure 8 - Flame radius evaluation .....   | 15 |
| Figure 9 - Flame radius evolutions .....   | 15 |
| Figure 10 - The back-to-back combustor configuration .....   | 16 |
| Figure 11 - The model installed in the HEG wind tunnel [97] .....  | 16 |
| Figure 12 - Symmetry plane cut of the HyShot II assembly.....  | 17 |
| Figure 13 – Normalized experimental pressure and heat-flux for the 28 km test. $P_{t2}=142$ kPa, $q_{t2}=4.38$ Mw/m <sup>2</sup> [97]. In blue, the data employed in this work. ....   | 17 |
| Figure 14 - Example of fixed embedding in a region of the domain and on a boundary .....   | 20 |
| Figure 15 - Example of spherical fixed embedding ad AMR.....   | 20 |
| Figure 16- Computational domain for the standard engine (a) and the pre-chamber engine (b).....  | 21 |
| Figure 17- Computational grid during the intake stroke. The AMR effect is noticeable in the intake duct and around the valve angle. ....   | 22 |
| Figure 18- The spherical density boxes around the pre-chamber orifices and spark plug at spark time. ....  | 22 |
| Figure 19 - Schematization of the crevice model regions .....  | 23 |
| Figure 20 - Highlight of the numerical domain on a symmetry cut of the experimental assembly [82]. ....  | 24 |
| Figure 21 – Perspective of the scramjet computational domain .....   | 24 |
| Figure 22 - Combustor Inlet conditions [99].....   | 24 |
| Figure 23 - Comparison of the computed and experimental pressure and net HRR traces, Standard engine. The solid blue lines represent the variability range in the 10 modeled cycles. ....  | 27 |
| Figure 24 - Experimental and numerical flame radii evolution.....  | 27 |
| Figure 25 - Comparison of the computed and experimental pressure and net HRR traces, Pre-chamber engine. The solid light grey lines represent the variability range in the 10 modeled cycles. ....   | 28 |
| Figure 26 - Evolution of the streamline pattern and contours of the Turbulent Kinetic Energy (TKE) on a longitudinal plane, reported for each of the operational phases of the active pre-chamber. ....  | 31 |
| Figure 27 - Pressure and net Heat Release Rate in the pre and main chamber. Dashed, the three flow reversal events. ....   | 32 |
| Figure 28 - Mass burnt fraction .....  | 32 |
| Figure 29 - Total flowrate N <sub>2</sub> excluded, red; O <sub>2</sub> flowrate, magenta; CO <sub>2</sub> flowrate, brown; CH <sub>4</sub> flowrate, yellow; CH <sub>3</sub> flowrate, green; 0.1xOH flowrate, blue. Dashed, the flow reversal events. When positive, the flow is toward the main chamber. .... | 33 |
| Figure 30 - Contribution to Equation (16) evaluated in the pre and main chamber.....   | 33 |
| Figure 31 - -148CAD, Early scavenging phase in the pre-camber; SOI= -150CAD .....  | 34 |
| Figure 32 - Total, CO <sub>2</sub> and CH <sub>4</sub> flow-rate between pre-chamber and main chamber.....   | 35 |

|   |    |
|---|----|
| Figure 33 - Instantaneous residual fraction and equivalence ratio and its standard deviation in the pre-chamber.....  | 35 |
| Figure 34 – Mass based binned distribution of the equivalence ratio in the pre-chamber at spark time.....   | 36 |
| Figure 35 - Equivalence ratio and Turbulent Kinetic Energy [m2/s2] distribution in the pre-chamber at spark time.....   | 36 |
| Figure 36 – Red, iso-surface of equivalence ratio=1; green, iso-surface of residual fraction=16% at spark time .....  | 37 |
| Figure 37 - Monitoring lines definition.....  | 38 |
| Figure 38 - G=0 iso-surfaces, indicating the turbulent flame front propagation, colored with temperature  | 39 |
| Figure 39 - Species mass fractions and HRR in the pre-chamber. (a) radicals and chemical HRR, (b) main product and net HRR. Dashed, the flow reversal events .....  | 40 |
| Figure 40 - Flame propagation in the pre-chamber; left axis, Equivalence Ratio (solid line); right axis, Temperature [K]. Flame visualization: iso-surfaces of G=0.....   | 41 |
| Figure 41 – Velocity magnitude [m/s] (dashed) and $Y_{CO_2}$ distribution along the orifices' axes- black dotted, the orifices; Flame visualization, iso-surface of G=0. Stream-traces colored with $Y_{CO_2}$ and Velocity magnitude . | 42 |
| Figure 42 - Early ejection time; top, flame visualization by a G=0 iso-surface colored with temperature. At the bottom, Temperature [K] (solid) and velocity magnitude [m\s] along the lines passing through the orifices. ....         | 43 |
| Figure 43 – Left axis, TKE (solid) and Damkohler number evolution; right axis, Temperature [K] (solid) and O,H and OH radicals mass fraction evolution.....   | 43 |
| Figure 44- Shear rate magnitude, left; Normal and tangential shear rate evaluated on the lines crossing the orifices. ....  | 44 |
| Figure 45- Takeno Flame Index distribution in the main chamber. The contour refers to a plane at middle height between the piston and the engine head. ....   | 45 |
| Figure 46 - Average temperature in the pre and main chamber .....   | 45 |
| Figure 47 - Species mass fractions and HRR in the main chamber. (a) radicals and chemical HRR, (b) main product and net HRR. Dashed, the flow reversal events. ....   | 46 |
| Figure 48 - Flow-field visualization at -2CAD. Streamtraces colored with the velocity magnitude; Iso-surface of G=0 colored with temperature; left slices colored with Damkohler number; right slices with temperature contour. ....    | 47 |
| Figure 49- $CH_4$ and O,H and OH radicals mass fractions evolution, left along the pre-chamber lines; right, along the orifices lines.....  | 48 |
| Figure 50- Left, Equivalence ratio and $C_2H_4$ mass fraction distribution; Right, O, H and OH and $C_2H_6$ mass fractions distribution along the lines in the pre-chamber. ....  | 49 |
| Figure 51- Left, Temperature [K] and Damkohler number distribution; Right, $CO_2$ and CO mass fraction distribution along the lines in the pre-chamber.....   | 49 |
| Figure 52. Nitrogen oxides mass fractions: (a) in the cylinder and (b) in the pre-chamber. Vertical dashed lines indicate flow reversal events. ....  | 50 |
| Figure 53- $NO_x$ , left axis, and un-burned hydrocarbons (dashed), right axis, mass fractions; Left, along the pre-chamber lines; Right, along the lines crossing the orifices. Black dashed, the orifices.....                        | 51 |
| Figure 54- $NO_x$ , left axis, and un-burned hydrocarbons (dashed), right axis, mass fractions; Left, along the pre-chamber lines; Right, along the lines crossing the orifices. Expulsion stage.....                                   | 51 |
| Figure 55- O,H and OH radicals and $NO_x$ mass fractions on the left axis, CO and HC mass fractions on the right axis along the cylinder lines.....   | 52 |

|   |    |
|---|----|
| Figure 56 - Pathway of NO reduction by reburning with Methane [26].....   | 52 |
| Figure 57- Mach number and density gradient distribution. ....  | 53 |
| Figure 58- Computed engine out emissions; Blue, pre-chamber engine.....   | 54 |
| Figure 59-Experimental and numerical flame visualization at -5 CAD. ....  | 55 |
| Figure 60-Experimental and numerical flame visualization at 0 CAD. ....   | 55 |
| Figure 61 - Experimental and numerical flame visualization at 3 CAD. ....   | 56 |
| Figure 62-Experimental and numerical flame visualization at 5 CAD. ....   | 56 |
| Figure 63- Experimental and numerical flame visualization and radius evaluation. ....   | 57 |
| Figure 64- Left, mass burnt fractions in the main chamber of the pre-chamber engine and of the standard engine; Right, flame radii of the modeled engines. ....   | 57 |
| Figure 65- Left, a-dimensional flame volume in the main chamber of the pre-chamber engine and of the standard engine; Right, mass burnt fractions in the main chamber of the pre-chamber engine and of the standard engine..... | 58 |
| Figure 66 - The kernel particles: Black, 1.5 CAD after SOS; Green, 4.5 CAD after SOS; Blue, 10 CAD after SOS. ....  | 59 |
| Figure 67 - The kernel evolution. (a), 1.5 CAD after SOS; (b) 4.5 CAD after SOS; (c) 10CAD after SOS. The flame is visualized as a G=0 iso-surface colored with temperature .....   | 60 |
| Figure 68 - The computational domain of the metal engine.....   | 60 |
| Figure 69 - Comparison between experimental and numerical pressure and heat release rate of the metal engine .....  | 60 |
| Figure 70 - Pressure contours in the symmetry plane. Top, the first quarter of the combustor; center, the whole combustor; bottom, a particular of the injection section .....  | 63 |
| Figure 71 - Mach number contours in the symmetry plane. Top, the first quarter of the combustor; center, the whole combustor; bottom, a particular of the injection section.....  | 63 |
| Figure 72 - Temperature contours in the symmetry plane. Top, the first quarter of the combustor; center, the whole combustor; bottom, a particular of the injection section .....   | 64 |
| Figure 73 - Hydrogen mass fraction. Top, the first quarter of the combustor; center, the whole combustor; bottom, a particular of the injection section .....   | 64 |
| Figure 74 - Density gradient contours. Top, the first quarter of the combustor; center, the whole combustor; bottom, a particular of the injection section .....  | 65 |
| Figure 75 - Comparison between the experimental and numerical pressure distribution along the symmetry line of the combustor. The experimental data are taken from [82]. ....   | 66 |
| Figure 76 - Comparison between the experimental and numerical heat flux distribution along a line at 6mm from the symmetry line. The experimental data are taken from [82]. ....  | 66 |
| Figure 77 - Comparison between the experimental and numerical heat flux distribution along a line at 9mm from the symmetry line. The experimental data are taken from [82]. ....  | 66 |
| Figure 78 - Preliminary RANS simulation results: (a), pressure distributions; (b) heat-flux distributions. ....   | 67 |
| Figure 79 - Q-criterion iso-surfaces colored with temperature. ....   | 68 |
| Figure 80 - Representation of the main vortical structures in the HyShot II combustor [136].....  | 68 |
| Figure 81 - Flow structures near the injector. Velocity streamlines colored with temperature.....   | 69 |
| Figure 82 - Snapshot of the computational grid in the injection section. ....   | 70 |
| Figure 83 – Vorticity contours and streamlines at different locations in the flow direction. ....   | 71 |
| Figure 84 - Ignition time for cold Hydrogen (300K) injected in hot air [134]. ....  | 72 |
| Figure 85 - OH mass fraction contours. Top, the first quarter of the combustor; center, the whole combustor;  |    |

|  |    |
|--|----|
| bottom, a particular of the injection section .....  | 73 |
| Figure 86 – H <sub>2</sub> O mass fraction contours. Top, the first quarter of the combustor; center, the whole combustor; bottom, a particular of the injection section .....   | 73 |
| Figure 87 – HO <sub>2</sub> mass fraction contours. Top, the first quarter of the combustor; center, the whole combustor; bottom, a particular of the injection section .....  | 74 |
| Figure 88 - Chemical source term. The white zones are characterized by null or negative values. Top, the first quarter of the combustor; center, the whole combustor; bottom, a particular of the injection section. ....  | 75 |
| Figure 89 - Mixture fraction contours and stoichiometric iso-line. Top, the first quarter of the combustor; center, the whole combustor; bottom, a particular of the injection section .....                               | 75 |
| Figure 90 – H <sub>2</sub> Mass source term contours. Top, the first quarter of the combustor; center, the whole combustor; bottom, a particular of the injection section .....  | 76 |
| Figure 91 - HO <sub>2</sub> Mass source term contours. Top, the first quarter of the combustor; center, the whole combustor; bottom, a particular of the injection section .....   | 77 |
| Figure 92 - OH Mass source term contours. Top, the first quarter of the combustor; center, the whole combustor; bottom, a particular of the injection section .....  | 77 |
| Figure 93 - H <sub>2</sub> O Mass source term contours. Top, the first quarter of the combustor; center, the whole combustor; bottom, a particular of the injection section .....  | 78 |
| Figure 94 - The computed Takeno Flame Index. Top, the first quarter of the combustor; center, the whole combustor; bottom, a particular of the injection section. The white regions are characterized by null values ..... | 78 |
| Figure 95 - Scatterplot Z,T. The markers are colored with the magnitude of the strainrate tensor.....  | 79 |
| Figure 96 - The Strain rate tensor norm distribution. Top, the first quarter of the combustor; center, the whole combustor; bottom, a particular of the injection section. ....  | 79 |

## List of Tables

---

|   |    |
|---|----|
| Table 1 - Experimental engine specifications .....  | 13 |
| Table 2 - Experimental engine performance .....   | 14 |
| Table 3 - The average flow conditions examined .....  | 18 |
| Table 4 - Comparison between the experimental and modeled engines performance, Standard engine .....    | 28 |
| Table 5 - Comparison between the experimental and modeled engines performance, Pre-chamber engine ..... | 29 |
| Table 6 - Operational phases and timings of the pre-chamber .....                                       | 30 |
| Table 7- Main pollutant mass fractions at EVO .....   | 52 |
| Table 8- Combustion progress times .....  | 58 |
| Table 9 - Comparison between the experimental and modeled engines performance, metal engine .....       | 61 |

# 1. Introduction

---

Combustion is the oldest technology of mankind and, at present day, about 88% of worldwide energy support is still provided by combustion [1]. This is due to the high specific energy of conventional fuels. Coupled with always less acceptable polluting emissions, the rising trend in energy consumption of the current and past century is pushing on research to develop cleaner combustion systems. Among all the polluting compounds emitted by combustion systems, carbon dioxide and water vapor represent the main ones. Thus, it appears that one way to reduce the carbon footprint of combustion systems is to remove carbon from fuels.

Theoretically, any oxidable compound is a fuel candidate. However, by considering the easily transportable ones and excluding the hazardous ones, only Hydrogen hydrocarbons compounds remain. Under this point of view, the so-called bio-fuels seems to be a good alternative to conventional ones. Being based on agricultural product or, better, on captured CO<sub>2</sub> they can be considered as carbon neutral [2]–[6], virtually neglecting the carbon emitted by their combustion in many scenarios.

Switching to Hydrogen is another way to abandon fossil fuels. It is a fascinating energy carrier [7], especially if produced by renewable sources [8]–[11]. It can be employed both in fuel cells, thus in fully electric devices, and as a true fuel in combustion systems.

Hydrogen fuel cells are a technology ancient know. However, the costs [12], the limited life-span and the need of Hydrogen with high degree of purity [13] are still issues to be solved. On the other hand, for Hydrogen as a fuel in an internal combustion engine a high grade of purity is not required. Nevertheless, other questions like backfire [14], injection strategies [15] or Hydrogen storage [16] are not solved yet. Anyway, metal hydrides Hydrogen storage seems to be the most promising technique to store Hydrogen at low temperatures and pressures [17], [18].

Recently, various efforts are being made also to asset Hydrogen transportability in already available piping [19]–[21], as well as, its employability in already existing plants and equipment [22]–[24]. For low dilution rates, no particular difficulties are encountered both in transportation and employment [21]. Unfortunately, due to its low density, such Hydrogen rates are not enough to remarkably reduce the total carbon content of the resulting fuel [25].

Other pollutants are mainly constituted by Sulphur and Nitrogen oxides. The firsts are usually due to lower purity fuels, such as coal or low grade liquid fuels. The latter, can arise from Nitrogen contained in fuels (Fuel NO<sub>x</sub>) or from the combustion process (thermal and prompt NO<sub>x</sub>) [26].

Research is currently involved in developing systems and solution aimed to reduce NO<sub>x</sub> production instead of post-treatment devices. Examples are given by steam injections turbine cycles [27] or by low temperature combustion [28], [29].

## 1.1 Recent trend in Internal Combustion Engine research: the Turbulent Jet Ignition system

The transportation sector represents the most evident example of transition. Despite the current trend in electrification [30], [31] and hybridization [32], it is a wide-spread opinion that Internal Combustion Engines (ICE) will be still the main power-train for a while [31], [33]–[35]. Therefore, several strategies have been developed to reduce fuel consumption and the environmental impact of modern engine such as those based on combustion monitoring [36] and the use of lean-combustion strategies [37], [38]. The role of lubricating oil in engine out emissions is being explored too [39]–[42].

Diesel engines are retained to have reached their end of life, at least for passenger applications, due to limited improvement margins and high post-treatment costs [43]. Thus, lean operating spark-ignition engine represents the actual trend in engine research [42], [44], [45]. However, higher ignition energies are required in order to successfully ignite a lean charge and various technologies, as the plasma igniters [46]–[48], the laser induced igniters [49]–[51], the corona spark plugs [51], [52], are already available but the overall engine cost would be prohibitive. A further alternative is represented by the Turbulent Jet Ignition (TJI) system, able to achieve the same goal without excessively increasing the implementation costs [53], [54] and with good capability of retro-fitting [55]. A TJI system generates hot and reacting jets in a separated volume, the so-called pre-chamber, by the combustion of a quasi-stoichiometric mixture, ignited by a standard spark-plug. The jets reach the main chamber through narrow orifices penetrating the main charge and igniting it in multiple points. Moreover, the high momentum proper of the jets promote the mixing between the hot reacting products and the fresh lean mixture. Thus, the main combustion is initiated by a combination of chemical and thermal effects and its speed is increased by the high turbulence levels induced by the jets. In this way, a superior tolerance to high diluent fraction in the main chamber can be also obtained [56], [57]. Moreover, a reduction of the cyclic variability proper of lean operating spark-ignition engine [58]–[60] can be achieved [54]. Thanks to the high dilution grade achievable with TJI, considerable improvements in NO<sub>x</sub> emission are possible [61], [62]. For the same reason, however, higher un-burned Hydro Carbons (HC) emissions are often reported [54], [63].

Despite the concept appears simple, the scavenging, filling and mixing phases of a small volume auxiliary chamber are challenging. In an active pre-chamber, scavenging is promoted by the fuel injection. Moreover, the mixture formation is achieved by the dilution of a rich charge, deriving from the injection, by the lean one, rising from the bottom, arriving from the main chamber. This causes a true charge stratification and represents a key aspect to be studied for optimal operation [64]. The ignition of the main charge represents another crucial aspect. It can occur either by “hot” jets or by “hot and reacting” jets, in function of the geometry of the pre-chamber and of the working conditions. Depending on the ignition mechanism, the main charge combustion can be more or less fast [65]–[67]. Therefore, also tracking key species plays an important role in the design and optimization of such systems [68]. Hence, 3D numerical simulations can significantly reduce the costs for design and optimization of TJI systems and studies focused on detailed analyses of the mass and energy exchange are increasingly encouraged. Many works have been conducted in configurations barely comparable to real engines [66], [67], [69], [70], while other works on active pre-chambers are based to 0D or 1D analyses [63], [71] and they rely on some limiting assumptions. Other works are usually focused on fluid dynamic aspects alone [70], [72]–[74] or at most consider only some major species (very often only the fuel) [63], [70], [72], [73], [75].

In the present work, a detailed analysis of an active TJI system, with an in-house developed pre-chamber focusing on several fundamental aspects such as mixing, charge ignition, combustion efficiency and emissions formation, is purposed. The same engine equipped with a standard spark-plug was also modeled and considered for comparison. The numerical model was validated against experimental data collected on an optically accessible engine fueled with Methane and operating in lean conditions ( $\lambda \approx 1.3$ ).

The key aspects, such as the energy provided by the pre-chamber to ignite the main charge, the species distribution, the operational phases of the pre-chamber (scavenging, filling, mixing, combustion...) and the overall emission production pathways are discussed in detail.

The present analysis, based on 3D numerical simulations, was aimed at considering all the fundamental aspects related to charge replacement, energy and mass exchange between the chambers and combustion process of a TJI system in order to provide a general as well as detailed method to describe the behavior of

such a complex system.

## 1.2 Hydrogen combustion: scramjets applications for hypersonic flights

The development of reliable and efficient hypersonic flight vehicles is today pursued for several interesting possibilities of application in the civil fields of space launch systems and passenger transportation. The main technical challenge is designing an air-breathing propulsion system capable of operating from low Mach number to the hypersonic regime ( $M > 5$ ). Achieving this goal with a single propulsion device seems to be not possible due to various dissipation phenomena related to moving parts of the machinery [76]. For  $M > 3$  cruise speed, the combustor can be replaced with a ramjet combustor. This kind of combustor exploits the fluid kinetic energy to raise the temperature in the combustor and initiate the combustion. The high temperature fluid is then expanded in a nozzle to generate the thrust. Similarly, in a scramjet (supersonic combustion ramjet) combustor, the higher kinetic energy of the flow is employed to raise pressure and temperature in the combustor to achieve the combustion. In this kind of combustor, the fluid residence time is very short, in the order of 1ms.

Today, a great effort is being devoted to the development of the scramjet technology; in particular, understanding the aero-thermochemistry in the supersonic combustor represents one of the most challenging problems. In particular, the fuel and air mixing, ignition and combustion represent the most crucial aspects being investigated. The experimental testing of this kind of engine is very difficult and expensive. Recent experimental research programs include the HyShot project by the University of Queensland [77], [78], the US-Australian HIFiRE program [79], and the European LAPCAT projects [80]. Numerical simulations of scramjet engines are also employed to investigate the aero-thermochemistry of the combustion chamber (see, for instance, [81] and [82]), but also the computational approach is very challenging due to the complexity of the physical phenomena involved. Moreover, the computational cost is in general very high due to the wide range of spatial and time scales involved.

In the present work, a portion of the HyShot II combustor has been modeled. After having validated the model accuracy against a set of experimental data, various details about the flow structure and combustion regime were extracted and analyzed and here presented.

## 2. Fundamentals of combustion modeling

---

Considering a chemically reactive flow, the system at each point in space and time can be completely described by specification of pressure, density, temperature, velocity field and concentration of each species. All of these properties can be changing in space and time due to chemical reactions, convection\advection and diffusion phenomena. However, some of these properties are globally conserved. Summing allover the processes that involves mass, momentum and energy changes leads to the definition of the conservation equations, known as *Navier-Stokes* equations. The following chapter will deal with the definition of the basic additional equations involved in combustion modeling, such as the species transport equation, and the chemical reactions equations.

In the present work, the commercial software CONVERGE CFD [83] was employed. CONVERGE is an immersed boundary reactive flow solver, based on the PISO algorithm [84]. It comes provided with various turbulence and combustion models. The ones employed in this work will be introduced in the dedicated sections and sub-sections.

### 2.1 The species transport equation

In a multispecies system, tracking each specie is mandatory, especially in reactive flows. The mass conservation equation, defined as:

$$\frac{\partial \rho}{\partial t} + \frac{\partial \rho \mathbf{u}}{\partial \mathbf{x}} = S \quad (1)$$

Can be rearranged in terms of species mass fractions as:

$$\frac{\partial \rho_m}{\partial t} + \frac{\partial \rho_m \mathbf{u}}{\partial \mathbf{x}} = \frac{\partial}{\partial \mathbf{x}} \left( \rho D_m \frac{\partial Y_m}{\partial \mathbf{x}} \right) S_m \quad (2)$$

Where  $S$  is the species' source term and the mass fraction of specie  $m$  over the total mass,  $Y_m$ , is defined as:

$$Y_m = \frac{M_m}{M_{tot}} = \frac{\rho_m}{\rho_{tot}}$$

The specie diffusion coefficient  $D_m$  can be assumed equal to the air's one if air is the major specie and the flow is turbulent -that is, transport is not diffusion controlled-, as in the cases evaluated in the present work, and defined by the following equation:

$$D_m = D = \frac{\nu}{Sc}$$

Where  $\nu$  is air's viscosity and  $Sc$  is the Schmidt number. In case of turbulent flows, the overall diffusion coefficient is given by:

$$D_m = D + D_t = D + \frac{\nu_t}{Sc_t} \quad (3)$$

The additional terms represent the turbulent viscosity and the turbulent Schmidt number, respectively, given by the turbulence model.

### 2.2 The scalar transport equation

Scalars are often employed to transport auxiliary information, needed by some sub-model or for post-processing purposes. For them, the general transport equation is assumed:

$$\frac{\partial \rho \phi}{\partial t} + \frac{\partial \rho \mathbf{u} \phi}{\partial \mathbf{x}} = \frac{\partial}{\partial \mathbf{x}} \left( \rho D \frac{\partial \phi}{\partial \mathbf{x}} \right) + S \quad (4)$$

Where  $\phi$  is a generic scalar,  $S$  its source term and  $D$  the diffusion coefficient, defined as Equation (3).

## 2.3 Turbulence transport equation

In the present work, the *RNG*  $k - \varepsilon$  RANS model was employed in the engine modeling setup while the Dynamic Smagorinsky LES model was employed in the scramjet model setup.

Their characteristic equations will be reported for completeness but not further discussed.

### 2.3.1 RANS turbulence modeling: the *RNG* $k - \varepsilon$ model

In the Reynolds Averaged Navier Stokes (RANS) turbulence models, the flow variables are decomposed into an ensemble mean and in a fluctuating term as:

$$\mathbf{u} = \bar{\mathbf{u}} + \mathbf{u}'$$

By substituting such decomposition into the Navier-Stokes equation, the compressible RANS equation for mass and momentum are obtained:

$$\begin{aligned} \frac{\partial \bar{\rho}}{\partial t} + \frac{\partial \bar{\rho} \tilde{u}_j}{\partial x_j} &= 0 \\ \frac{\partial \bar{\rho} \tilde{u}_i}{\partial t} + \frac{\partial \bar{\rho} \tilde{u}_i \tilde{u}_j}{\partial x_j} &= -\frac{\partial \bar{P}}{\partial x_i} + \frac{\partial}{\partial x_j} \left[ \mu \left( \frac{\partial \tilde{u}_i}{\partial x_j} + \frac{\partial \tilde{u}_j}{\partial x_i} \right) - \frac{2}{3} \mu \frac{\partial \tilde{u}_k}{\partial x_k} \delta_{ij} \right] + \frac{\partial}{\partial x_i} (-\bar{\rho} \tilde{u}_i' u_j') \end{aligned} \quad (5)$$

The Favre average of velocity is given by:

$$\tilde{u}_i = \frac{\overline{\rho u_i}}{\bar{\rho}} \quad (6)$$

The last term on the right-hand side of Equation (16) is referred as Reynolds stress tensor, denoted with  $\tau_{ij}$ .

The aim of each turbulence model is modelling such tensor.

The ReNormalized Group (RNG)  $k - \varepsilon$  model [85] models the Reynolds stress as:

$$\tau_{ij} = 2\mu_t S_{ij} - \frac{2}{3} \delta_{ij} \left( \rho k + \mu_t \frac{\partial \tilde{u}_l}{\partial x_l} \right) \quad (7)$$

Where the turbulent viscosity is given by:

$$\mu_t = C_\mu \rho \frac{k^2}{\varepsilon}$$

The turbulent kinetic energy is equal to the half of the trace of the stress tensor:

$$k = \frac{1}{2} \tilde{u}_i \tilde{u}_i$$

And the mean strain rate tensor is given by:

$$S_{ij} = \frac{1}{2} \left( \frac{\partial \tilde{u}_i}{\partial x_j} + \frac{\partial \tilde{u}_j}{\partial x_i} \right)$$

The model introduces two additional transport equations, one for the turbulent kinetic energy and one for the dissipation rate, Equations (8) and (16):

$$\frac{\partial \rho k}{\partial t} + \frac{\partial \rho u_i k}{\partial x_i} = \tau_{ij} \frac{\partial u_i}{\partial x_j} + \frac{\partial}{\partial x_j} \left( \frac{\mu + \mu_t}{Pr_k} \frac{\partial k}{\partial x_j} \right) - \rho \varepsilon + \frac{C_s}{1.5} S_s \quad (8)$$

$$\begin{aligned} \frac{\partial \rho \varepsilon}{\partial t} + \frac{\partial \rho u_i \varepsilon}{\partial x_i} &= \frac{\partial}{\partial x_j} \left( \frac{\mu + \mu_t}{Pr_\varepsilon} \frac{\partial \varepsilon}{\partial x_j} \right) + C_{\varepsilon 3} \rho \varepsilon \frac{\partial u_i}{\partial x_i} + \left( C_{\varepsilon 1} \frac{\partial u_i}{\partial x_j} \tau_{ij} - C_{\varepsilon 2} \rho \varepsilon + C_s S_s \right) \frac{\varepsilon}{k} \\ &+ S - \rho R_\varepsilon \end{aligned} \quad (9)$$

In this equations  $S$  and  $S_s$  are source terms, the first user-supplied and the second due to the interaction with sprays. Also,  $C_{\varepsilon i}$ ,  $C_S$  and  $C_\mu$  are user-supplied model constants. Moreover,

$$R_\varepsilon = \frac{C_\mu \eta^3 \left(1 - \frac{\eta}{\eta_0}\right) \varepsilon^2}{(1 + \beta \eta^3) k}$$

With

$$\eta = \frac{k}{\varepsilon} \sqrt{2 S_{ij} S_{ij}}$$

Finally, the turbulence length scale is evaluated as:

$$le = C_\mu^{\frac{3}{4}} \frac{k^{\frac{3}{2}}}{\varepsilon} \quad (10)$$

### 2.3.2 LES turbulence modeling: the Dynamic Smagorinsky Sub Grid Scale model

With the RANS approach, only the mean flow is actually resolved and the turbulence effects are all modeled by means of a dedicated turbulence closure model.

Large Eddy Simulations (LES), on the contrary, are able to solve also a part of the turbulent properties of the flow (namely, the large eddies). Generally, the velocity field can be decomposed in the resolved field and in a modeled field, called Sub-Grid Scale (SGS) field as:

$$\mathbf{u} = \bar{\mathbf{u}} + \mathbf{u}'$$

The resolved velocity field is a spatial average of the actual velocity field, unlike RANS that evaluates the mean velocity field as an ensemble average. Because of this decomposition, the LES filter is characterized by the following properties:

$$\begin{aligned} \bar{\bar{u}}_i &= \bar{u}_i \\ \bar{u}'_i &= 0 \end{aligned}$$

By applying the LES decomposition, the momentum conservation equations can be re-written as:

$$\frac{\partial \bar{\rho} \tilde{u}_i}{\partial t} + \frac{\partial \bar{\rho} \tilde{u}_i \tilde{u}_j}{\partial x_j} = -\frac{\partial \bar{P}}{\partial x_i} + \frac{\partial \bar{\sigma}_{ij}}{\partial x_j} - \frac{\partial \tau_{ij}}{\partial x_j} \quad (11)$$

Here, again, the tilde indicates the Favre average given by Equation (16) and  $\sigma_{ij}$  indicates, for brevity, the resolved flow viscous stress.

Due to the LES decomposition, the Reynolds stress tensor assumes the following form:

$$\tau_{ij} = \bar{\rho} (\tilde{u}_i \tilde{u}_j - \tilde{u}_i \tilde{u}_j)$$

The turbulence length scale can be referred to the cell volume,  $V$ , as:

$$le = \sqrt[3]{V}$$

Different formulations exist to model the Reynolds stress tensor with the LES approach. The Smagorinsky SGS [86] model is a zero-equation model. It does not require additional transport equations and relates the Reynolds stress tensor to the shear stress tensor by means of a user supplied model constant and a filter.

The filter is represented by the average cell length:

$$\Delta = \sqrt[3]{V}$$

The turbulent viscosity is evaluated as:

$$\nu_t = C_s^2 \Delta^2 \sqrt{S_{ij} S_{ij}}$$

And, finally, the sub-grid stress tensor is given by:

$$\tau_{ij} = -2 \nu_t \bar{S}_{ij} \quad (12)$$

The dynamic Smagorinsky model [87], substantially, internally evaluates the value of  $C_s$  by means of the so called Germano identity and by performing a second filtration.

The  $\Delta$  and  $\hat{\Delta}$  filtered Reynolds stress are, respectively, given by:

$$\begin{aligned}\tau_{ij} &= (\overline{u_i u_j} - \overline{u_i} \overline{u_j}) \\ T_{ij} &= (\overline{\widetilde{u_i u_j}} - \widetilde{\overline{u_i} \overline{u_j}})\end{aligned}$$

The first equation represents, effectively, the modeled sub-grid stresses. The second, the filtered (or test) sub-grid stresses.

The Germano identity relates the two levels stress tensors by defining the Leonard stress terms as:

$$L_{ij} = T_{ij} - \tau_{ij}$$

Such expression is representative of the actually resolved turbulent stresses and contains the contributions of all the scales between the filter and the sub-filter dimensions.

The deviatoric part of the Leonard stress term can be evaluated as:

$$L_{ij} - \frac{1}{3} L_{kk} \delta_{ij} = C_{s-dynamic} M_{ij}$$

Where  $C_{s-dynamic}$  is the Dynamic Smagorinsky constant and  $M_{ij}$  is defined as:

$$M_{ij} = 2 \hat{\Delta}^2 |\widehat{S}| \widehat{S}_{ij} - 2 \Delta^2 |\widetilde{S}| \widetilde{S}_{ij}$$

The sub-grid scale stress tensor can be evaluated as in Equation (16) replacing the Smagorinsky constant with the dynamic one which can be calculated, as purposed in [88], by:

$$C_{s-dynamic} = \frac{M_{ij} L_{ij}}{M_{kl} M_{kl}}$$

## 2.4 Combustion modeling

Combustion phenomena can be classified, basically, into premixed and non-premixed combustion.

It is said premixed a combustion in which the fuel and the oxidizer are mixed before of combustion commencing. In such situation, when the combustion starts, a flame front propagates “smoothly” through the fresh mixture. Typically, the mixture behind the flame front rapidly approaches the equilibrium state while the mixture in front of the flame remains in the un-burned state. The flame-front is a transition region whose thickness and speed are related to the actual thermodynamic and turbulent conditions, as well as, to the chemical species involved. A schematic representation of a turbulent premixed flame is given in Figure 1.

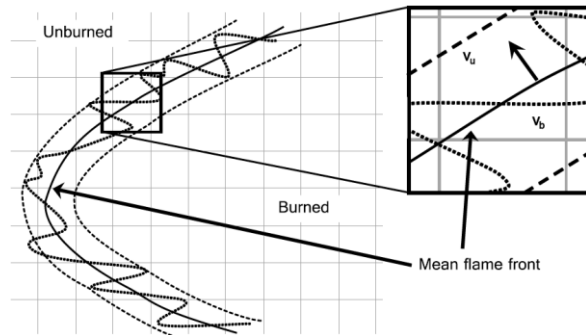


Figure 1 - Scheme of a premixed turbulent flame [89]

In non-premixed combustion phenomena, fuel and oxidizer get mixed during the combustion. The combustion starts when favorable conditions (both chemical and thermodynamic) are achieved, somewhere in the domain, and progresses mainly in a diffusion-controlled regime.

Turbulence plays a crucial role in combustion phenomena, enhancing the mixing and transport phenomena. The turbulent vortices interact with the flame front accelerating both the species and the heat diffusion. This expands the region of influence of the flame front, making it thicker. Generally, the combustion speed increases with the turbulence levels but highly turbulent flows can inhibit ignition.

### 2.4.1 SAGE detailed chemical kinetic solver

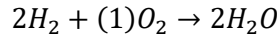
Figure 2 reports, as an example, the so-called reaction pathway (or reaction flow diagram) of Methane oxidation. The set of reactions describing such phenomena is defined as *reaction mechanism*.

A reaction mechanism contains all the information useful to model the reaction rate of each reaction, accordingly with the Arrhenius formulation:

$$k_{f(r)} = A \cdot T^\beta \cdot \exp\left(-\frac{Ea}{RT}\right)$$

The pre-exponential constant,  $A$ , the exponential factor,  $\beta$ , and the activation energy,  $Ea$ , are, therefore, reported in the mechanism.

By introducing a *rate law*, the reaction rate can be linked to the specific reaction in order to describe its evolution in time; taking the Hydrogen oxidation simplified reaction as an example:



The rate law gives, for the *forward* reaction, the production (consumption) rate of  $H_2$ :

$$\frac{d[H_2]}{dt} = -k_f[H_2]^2 \cdot [O_2] = \dot{\omega}_{H_2}$$

If favorable conditions are achieved, the *reverse* reaction can occur, and the rate law gives:

$$\frac{d[H_2]}{dt} = k_r[H_2O]^2 = \dot{\omega}_{H_2}$$

$k_f$  and  $k_r$  are, respectively, the forward and the reverse reaction rates. Their ratio between gives the reaction equilibrium constant. Such constant can be evaluated on the basis of the actual thermodynamic conditions as:

$$k_c = \frac{k_f}{k_r} = \exp\left(-\frac{\Delta_R \bar{G}^0}{RT}\right) \cdot \left(\frac{P_{atm}}{RT}\right)^{\sum_{i=1}^N \nu_i}$$

Where  $N$  is the total number of species involved in the considered reaction,  $\nu_i$  is the  $i$ -th specie stoichiometric coefficient,  $T$  is the actual temperature,  $R$  the universal gas constant and  $\Delta_R \bar{G}^0$  is the Gibbs' free energy variation across the considered reaction. The thermodynamic data, namely  $Cp, H^0$  and  $S^0$ , of the involved species are retrieved from the NASA polynomial expression.

The system of ordinary differential equation is then closed by the overall energy balance equation:

$$\frac{dT}{dt} = \frac{V \frac{dp}{dt} - \sum_{i=1}^N (h_i^0 \dot{\omega}_i)}{\sum_{i=1}^n (Cp_i [X_i])}$$

Where  $i$  denotes the  $i$ -th species and  $h^0$  and  $Cp_i$  represent the species enthalpy and specific heat, respectively, on molar basis.

In CONVERGE, the SAGE detailed chemistry solver [90] is employed to solve for the given reaction mechanism. In such implementation, the chemical solver is called after the CFD step. Once chemical calculation is complete, the new species concentrations are passed to the CFD solver, and the temperatures are adjusted on the basis of the new species distribution.

The detailed mechanism approach is suitable both for premixed and non-premixed combustion study. All the involved transport phenomena are solved by the CFD solver and not modeled by the chemistry solver.

Such coupling makes the turbulence-combustion interaction, implicit. On the other hand, this implies that a sufficient grid resolution needs to be achieved in order to obtain reliable results.

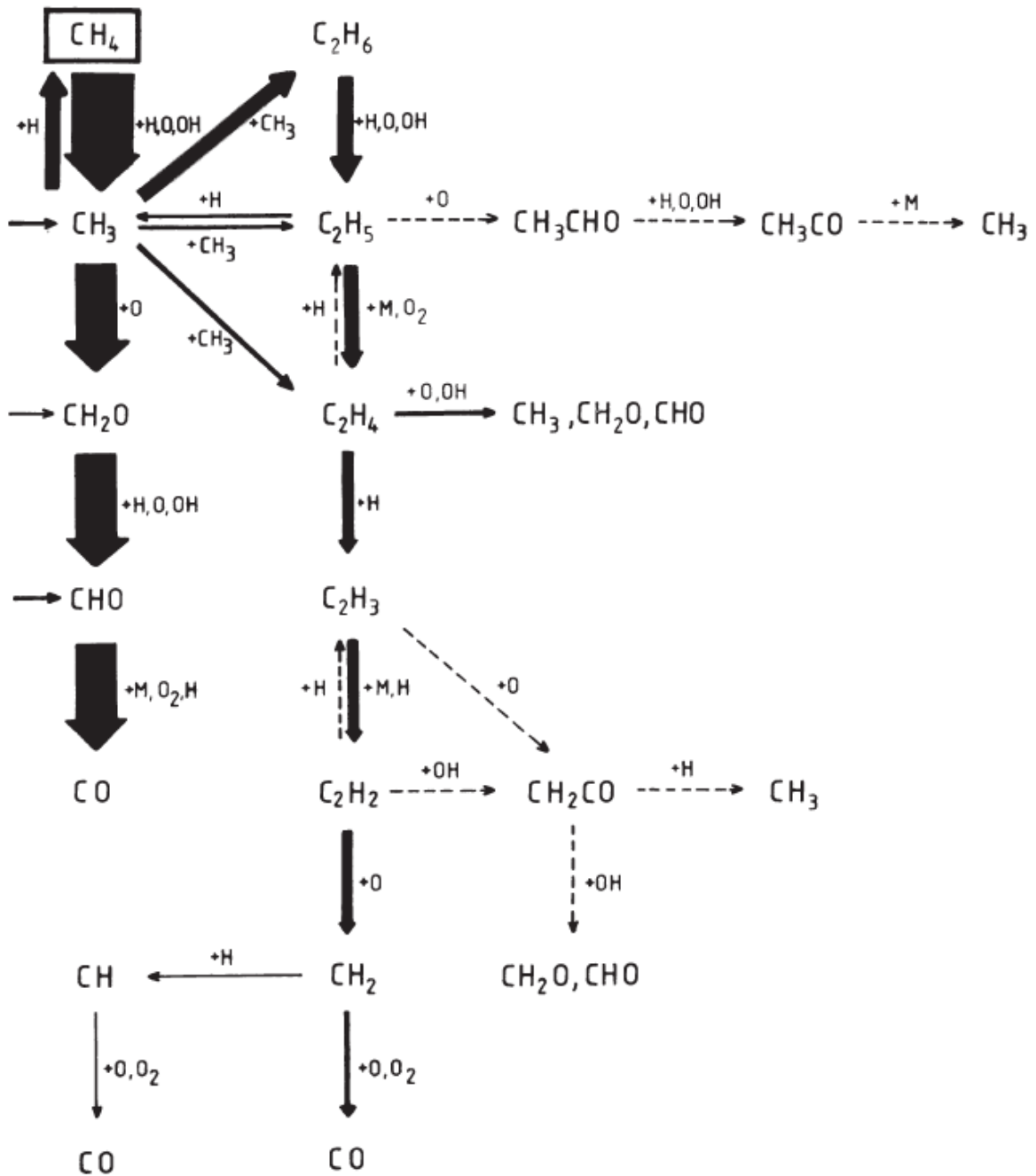


Figure 2 - Flow diagram for stoichiometric Methane oxidation [91]

### 2.4.2 Combustion modeling of premixed flames: the G-equation approach

The G-equation approach is a level-set method employed to track the flame-front and to solve for the chemical reactions, eventually, only in the combusting region of the domain [92].

Depending on the value of the scalar G, the domain can be divided into three zones:

- $G < 0$ , the un-burned region;
- $G = 0$ , the flame-front;
- $G > 0$ , the burned region.

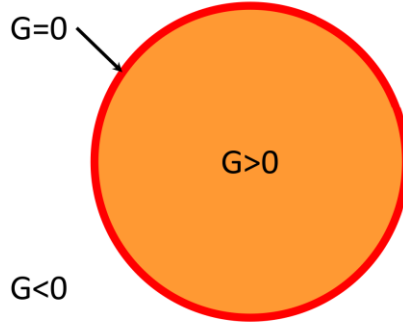


Figure 3 - Conceptual structure of a flame with the G-equation approach

The transport equation of G and its variance are, respectively, given by:

$$\frac{\partial \rho \tilde{G}}{\partial t} + \frac{\partial \rho u_d \tilde{G}}{\partial x_d} = -\rho D'_t \tilde{k} \left| \frac{\partial \tilde{G}}{\partial x_d} \right| + \rho u_s s_t \left| \frac{\partial \tilde{G}}{\partial x_d} \right| \quad (13)$$

$$\frac{\partial \rho \tilde{G}''^2}{\partial t} + \frac{\partial \rho u_d \tilde{G}''^2}{\partial x_d} = \frac{\partial}{\partial x_d} \left( \rho D_t \left| \frac{\partial \tilde{G}''^2}{\partial x_d} \right| \right) + 2\rho D_t \frac{\partial \tilde{G}}{\partial x_d} \frac{\partial \tilde{G}}{\partial x_d} - c_s \rho \tilde{G}''^2 \frac{\varepsilon}{k} \quad (14)$$

Numerically, G represents the distance from the flame-front while its variance represents the turbulent flame brush thickness.

In Equation (13), the first term on the RHS represents the flame curvature contribution while the second is related to the turbulent mass burn rate and depends on the actual turbulent flame speed.

The corrected diffusion term and the flame curvature are given, respectively, by:

$$D'_t = \sqrt{C_s \frac{k}{2} \frac{C_\mu}{Sc} \tilde{G}''^2}$$

$$\tilde{k} = -\frac{\partial}{\partial x_d} \left( \frac{\partial \tilde{G}}{\partial x_d} / \left| \frac{\partial \tilde{G}}{\partial x_d} \right| \right)$$

Equation (16) and the corrected diffusion term represents the link between the flame-front propagation and the actual turbulence conditions.

The turbulent flame-speed can be evaluated accordingly with:

$$s_t = s_l + u' \left\{ \frac{-a_4 b_3^2}{2b_1} Da + \left[ \left( \frac{a_4 b_3^2}{2b_1} Da \right)^2 + a_4 b_3^2 Da \right]^{\frac{1}{2}} \right\} \quad (15)$$

Where  $u'$  is the velocity fluctuation and  $Da$  is the Damkohler number, defined as:

$$Da = \frac{s_l l_t}{u' \delta_l} \quad (16)$$

Where  $s_l$  is the local laminar flame speed,  $\delta_l$  is the local laminar flame thickness,  $l_t$  is the local turbulent length scale and  $u'$  is the local velocity fluctuation, both evaluated by the turbulence model.

The laminar flame-speed can be evaluated with the so-called power-law expression:

$$s_l = s_{l,ref} \left( \frac{T_u}{T_{ref}} \right)^\alpha \left( \frac{P_u}{P_{ref}} \right)^\beta (1 - 2,1Y_{dil}) \quad (17)$$

With the reference laminar flame-speed given by:

$$s_{l,ref} = \omega \phi^n \exp[-\xi(\phi - 1,075)^2] \quad (18)$$

In Equation (16),  $\omega$  represents the laminar flame-speed of the given fuel at ambient (*reference*) and stoichiometric conditions.  $n$  and  $\xi$  are fitting constants proper of the fuel.

In Equation (17), the  $u$  pedix indicates the un-burned region. Moreover,  $\alpha$  and  $\beta$  represents other fitting values or functions. Different expressions and values of  $\alpha$  and  $\beta$  are purposed in literature. In the present work, the ones purposed by Amirante et al. [93] are employed:

$$\begin{aligned} \alpha &= \alpha_2 \phi^2 - \alpha_1 \phi + \alpha_0 \\ \beta &= -\beta_2 \phi^2 + \beta_1 \phi - \beta_0 \end{aligned}$$

The values of  $\alpha_i$  and  $\beta_i$  are fuel dependent.

Such expressions were implemented in CONVERGE by means of a User Defined Function (UDF) both for Methane and for Gasoline laminar flame-speed calculation.

Regarding the constants in Equation (15), it can be said that:

- $b_1$ , is a proportionality constant between the fully developed turbulent flame-speed and the velocity fluctuation, namely  $s_t = b_1 u'$ ;
- $b_3$ , relates the turbulent and the laminar diffusivity at the turbulent and laminar flame-speed,  $\frac{s_t}{s_l} = b_3 \sqrt{\frac{D_t}{D}}$ ;
- $a_4$ , represents the connecion between the turbulent diffusivity and the turbulence integral length scale and velocity fluctuation,  $D_t = a_4 u' l$ .

### 3. The experimental data

---

This thesis work relies on two sets of experimental data, one referred to the internal combustion engine and the other to the scramjet combustor. They will be presented separately in the following sub-sections.

#### 3.1 Experimental Engine data

An in-house developed active pre-chamber prototype was tested on an optically accessible engine. A representation of the TJI apparatus is given in Figure 4.

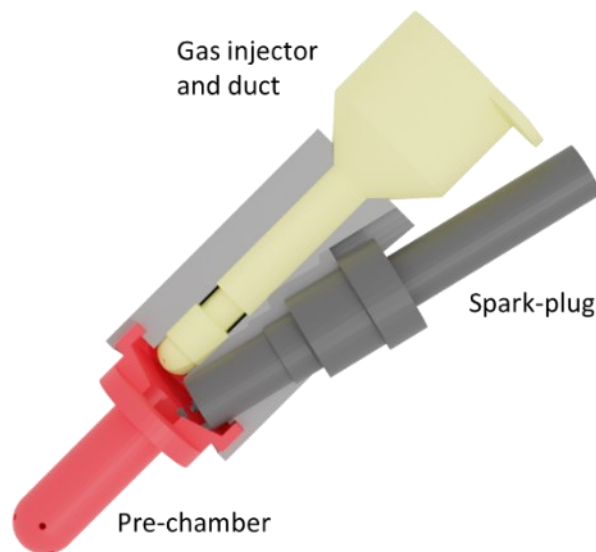


Figure 4 - The pre-chamber assembly

The internal volume of the pre-chamber was about 6% of the engine clearance volume and the connection with the main chamber was represented by 4 small angled circular orifices.

The tests were carried out, by our partners of the Istituto Motori CNR di Napoli, on a four-stroke Port Fuel Injection (PFI) optically accessible spark-ignition engine connected to an electrical dynamometer. It was equipped with a pent-roof four-valves and centrally located spark plug head. A sapphire window flat piston and a quartz cylinder were employed. Both fired and unfired cycles were considered, at an engine speed of 2000 rpm.

Two engine configurations have been tested: a typical SI engine with a spark plug located at the center of the head, which will be referred to as the *standard engine* and a modified configuration, which has the pre-chamber mounted in the place of the spark plug and will be referred to as the *pre-chamber engine*. A decrease of the compression ratio has been observed due to the presence of the pre-chamber volume but not corrected. Indeed, the aim of the campaign was to assess the retro-fitting capability of the TJI system. The main engine specifications are summarized in Table 1.

The pressure distributions versus the crank angle and several digital images of the flame have been recorded during the experimental campaign.

In the considered tests, the engine was fueled with Methane supplied to the injectors by an 8-bar pressurized tank. The pre-chamber injector, a modified Synerject Strata GDI injector, was connected with the pre-chamber by a properly dimensioned duct.

In both configurations, the end of fuel injection and the start of spark were fixed in order to operate at the

maximum brake torque, with  $\lambda=1.3\pm 1\%$ . Such dilution was chosen because representative of the lean operating limit of the standard engine. Although leaner conditions can be established with a TJI system, an analysis performed in the selected conditions makes possible a direct comparison between the capability of igniting the main charge of the TJI system with that of the traditional spark plug. In this way, the benefits in terms of efficiency and emissions brought to an existing engine retrofitted with a TJI system can be quantitatively defined.

In the modified engine, the start of fuel injection in the pre-chamber was fixed at 150 CAD Before the Top Dead Center (BTDC), in order to optimize the exhaust emissions. A linear lambda sensor was used to measure the air-fuel equivalence ratio and a quartz pressure transducer to acquire the in-cylinder pressure. Sensors were synchronized with an optical shaft encoder and a crank angle degree marker.

The intake air temperature was at 298 K while the refrigerating fluid temperature was kept at 333 K in order to protect the self-lubricating teflon-bronze piston rings in the optical section.

Two-dimensional digital flame images were acquired with a 12500 fps 16-bit gray scale camera with a 1024x1024 resolution. The camera CMOS sensor was lighted by the combustion through a 45° oriented UV-visible mirror. A representation of the experimental setup is purposed in Figure 5.

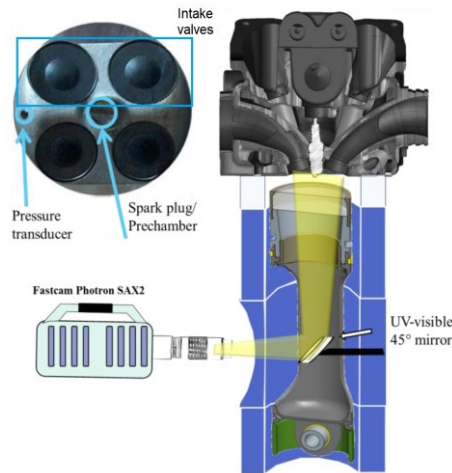


Figure 5 - Representation of the optical setup

| Displacement [cm <sup>3</sup> ] | 250                  |                   | Standard     | Pre-chamber |
|---------------------------------|----------------------|-------------------|--------------|-------------|
| Bore [mm]                       | 72                   | PFI EOI [CAD]     | <u>0°</u>    | <u>0°</u>   |
| Stroke [mm]                     | 60                   | PFI DOI [CAD]     | <u>100°</u>  | <u>90°</u>  |
| Connecting rod [mm]             | 130                  | Pre-chamber [CAD] | <u>SOI</u>   | <u>DOI</u>  |
| Compression ratio               | 9:1                  |                   | <u>-150°</u> | <u>7.8°</u> |
| Maximum power                   | <u>7.9@5000 rpm</u>  | SOS [CAD]         | <u>-24°</u>  | <u>-22°</u> |
| Maximum torque [N]              | <u>14.7@5000 rpm</u> |                   |              |             |

Table 1 - Experimental engine specifications

The acquired pressure and computed Heat Release Rate (HRR) traces for both the configurations are summarized in Figure 6. The pressure traces were obtained as an average over 500 consecutive cycles.

The net (or apparent) Heat Release Rate was computed accordingly with Equation (16) [94]:

$$\frac{dQ_n}{d\theta} = \frac{1}{k-1} V \frac{dP}{d\theta} + \frac{k}{k-1} P \frac{dV}{d\theta} \quad (19)$$

Where,  $P$  is the averaged pressure and  $V$  is the actual displaced volume which accounts for the clearance volume and for the pre-chamber volume.

Considering the kind of the employed engine, no measurements of emissions were performed.

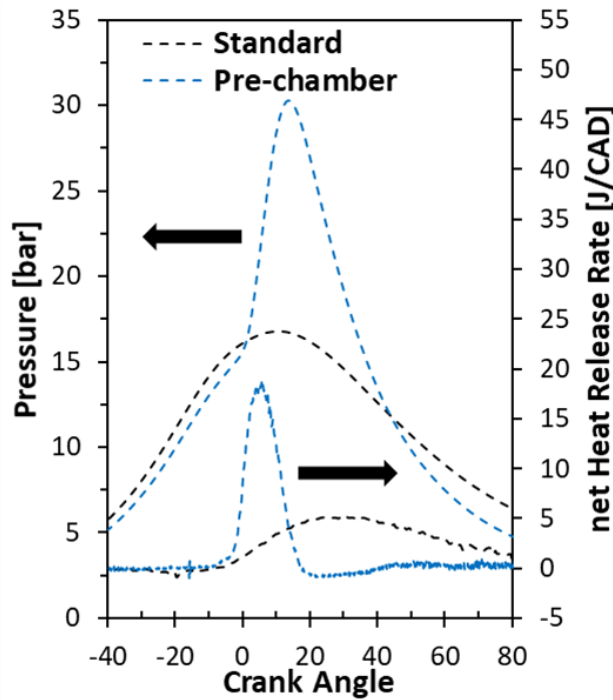


Figure 6 - Experimental pressure and HRR traces

The pressure trace of the pre-chamber engine is lower, until the ignition, than the one of the standard engine, due to the before mentioned loss of compression ratio. A sudden peak in pressure and nHRR is noticed just before the TDC and represents the ejection of the reacting material and the following main charge ignition, as can be visualized in Figure 7. It appears that a lot of energy is available for the main charge ignition. Moreover, the ignition is achieved in multiple point and the jets from the pre-chamber promotes mixing between the fresh lean mixture and the reacting material being released from the pre-chamber, as can be noticed by the flame images, reported in Figure 7.

Soon after the nHRR peak, it is possible to identify a significant mass leakage from the cylinder for the pre-chamber engine: namely, the negative values of the net HRR between 20 and 40 CAD ATDC are due to an outgoing flow related to the piston rings typology required in optical engines, which do not ensure a proper sealing action, compared to those of a metal engine, as discussed in detail in [95]. Indeed, the computed Integrated apparent Heat Released (IaHR) of the pre-chamber engine is smaller than the standard one, as summarized in Table 2.

|                    | IMEP [bar] | IMEP <sub>cov</sub> | Work[J] | IaHR[J] |
|--------------------|------------|---------------------|---------|---------|
| <b>Pre-chamber</b> | 3.46       | 2.9                 | 86      | 210     |
| <b>Standard</b>    | 3.32       | 7.4                 | 83      | 278     |

Table 2 - Experimental engine performance

Nevertheless, the overall engines works are comparable, as well as, the IMEP. The higher IMEP<sub>cov</sub> of the standard engine suggests that the selected dilution is close to the lean limit.

Figure 7 reports some flame images, showing the characteristic conical structure of a high-pressure reacting jet ejected from an orifice. As will be highlighted in section 5.2-*The pre-chamber engine*, the so-called

mushroom shaped flames, are detached from the pre-chamber orifices and their energy and chemical composition is such to make the main ignition happening in multiple points.

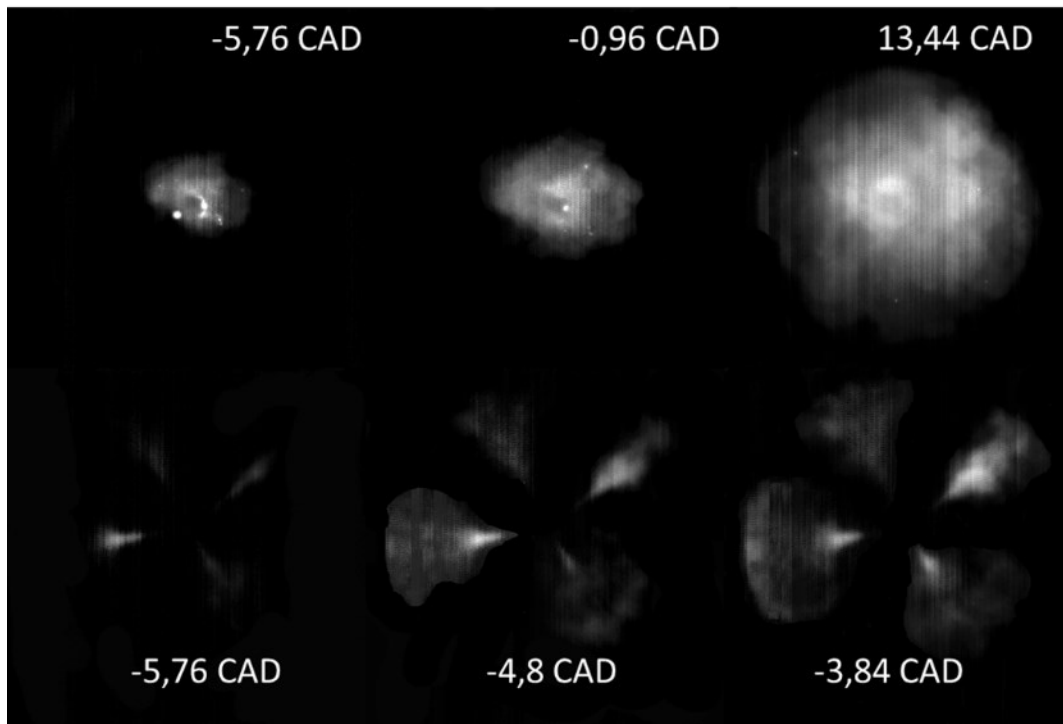


Figure 7 - Experimental flame visualizations. Top, the standard engine; Bottom the pre-chamber engine.

As will be pointed out by the numerical simulations, the ignition mechanism involves both thermal and chemical matters and is related with the high combustion speed typically observed in TJI equipped engines. The standard engine is, on the other hand, characterized by a typical spherical developing flame. By comparing the flame surface extension, it clearly appears that the flame speed is much lower.

The flame mean radius was also measured, at Istituto Motori, by averaging the distance between the spark and the boundary of the flame, as schematized in Figure 8. Such measurement, evaluated over the time, is proportional to the flame speed and, consequently, to the burn rate.

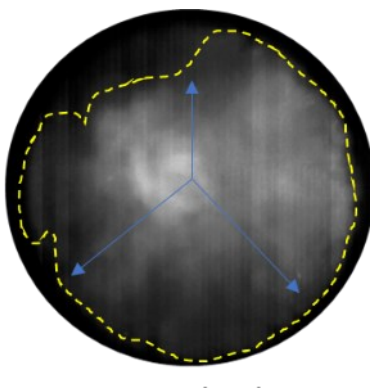


Figure 8 - Flame radius evaluation

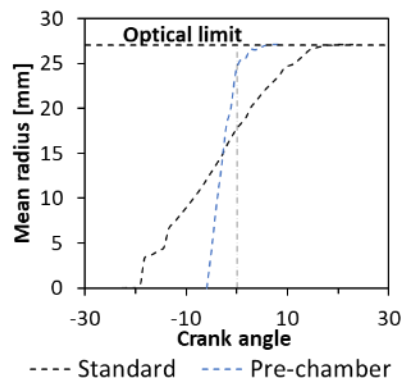


Figure 9 - Flame radius evolutions

By comparing the measurements, reported in Figure 9, it appears that the combustion for the pre-chamber engine is almost twice faster than for the standard one.

### 3.2 Experimental scramjet data

The Hyshot II combustor is composed by a rectangular shaped duct, terminating with an expansion nozzle, and is fed by four port-hole injectors ( $D=2$  mm) placed, on the lower side of the combustor, 58 mm downstream of the combustor leading edge – cf. Figure 12 and Figure 20. The injection pressure is such to achieve critical conditions at the injector exit.

A few experimental campaigns regarded the HyShot II combustor. Only one regarded a real flight experiment and was performed in 2002 by the Queensland University in the Woomera flight area in Australia. A back-to-back configuration of two combustor was installed on a two-stage sounding rocket. It followed a parabolic trajectory, with an apogee at 314 km. in the descending phase, at around 35 km from the ground, the Hydrogen injector of one combustor were fed with the fuel, making the experiment commencing. The other combustor was un-fed, in order to acquire information about the air only stream. The flight speed was such that  $M=7.5$ . The experiment ended at an altitude of 23 km, with a fling speed with  $M=7.4$  [96].

During the flight, various data about the external and internal flow conditions were acquired. In the following ground experiments, the information about the free stream gathered with the flight experiment, were employed to setup the wind tunnels in order to achieve realistic flow conditions.

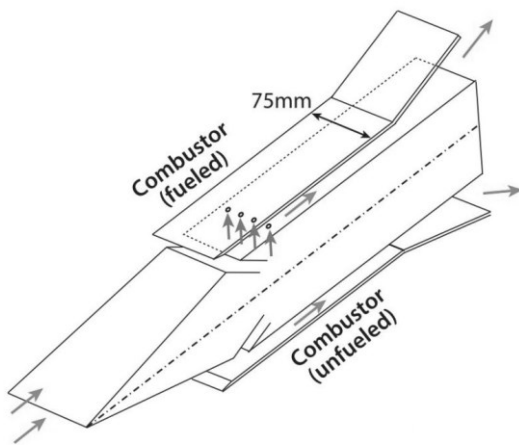


Figure 10 - The back-to-back combustor configuration

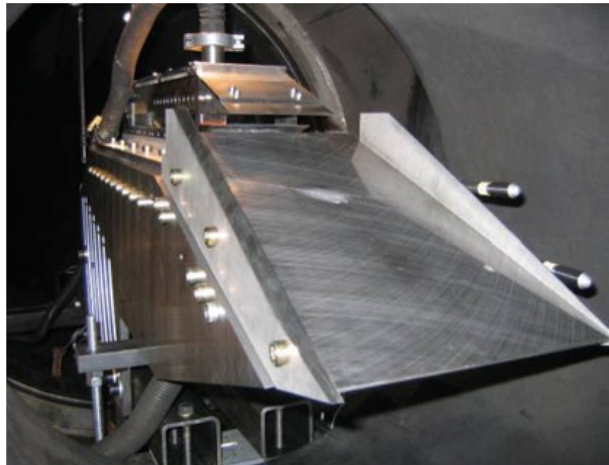


Figure 11 - The model installed in the HEG wind tunnel [97]

The ground test data employed in this work were acquired in the High Enthalpy shock tunnel of Gottingen (HEG) and are representative of a Mach 7.4 flight at an altitude of 28 km. The full model, of which a quoted section is given in Figure 12, was tested.

The HyShot II combustion chamber is parallel, and the cross-sectional dimensions are  $9.8 \times 75$  mm. The length of the constant area combustor is 300 mm. Fuel is injected into the combustion chamber by four cylindrical injectors, with radius of 1 mm, positioned along one line in cross flow direction in the body side combustor wall, 57.5 mm downstream of its leading edge.

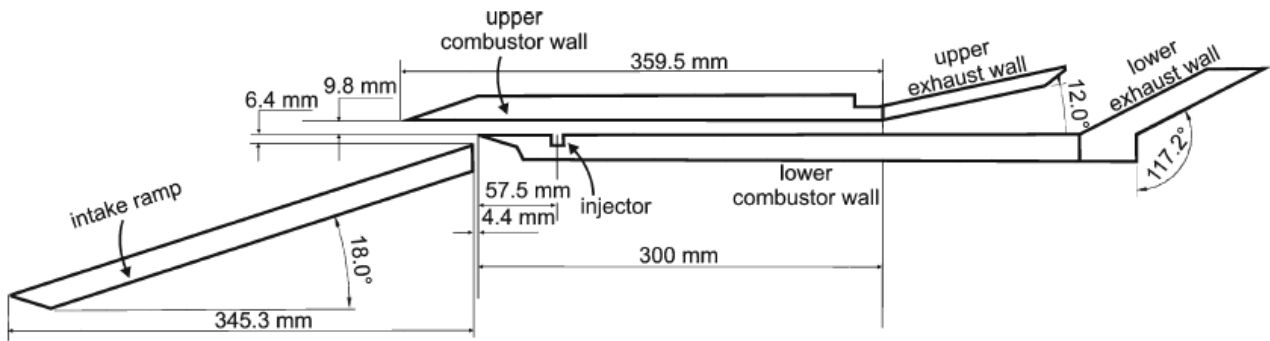


Figure 12 - Symmetry plane cut of the HyShot II assembly

On the intake ramp, 5 pressure gauges and 4 thermocouples were installed along the symmetry line. The cowl side combustion chamber plate was instrumented with 23 pressure gauges and 11 thermocouples. The pressure transducers were positioned along the symmetry line and the thermocouples along a line 9 mm off the symmetry line. In the body side combustion chamber plate 31 pressure transducers and 15 thermocouples were integrated. The pressure gauges were positioned along the symmetry line and the thermocouples downstream of a Hydrogen injector along a line 9 mm off the symmetry line. The cowl (upper) side and body (lower) side thrust surfaces were instrumented with 5 and 6 pressure transducers, respectively [98].

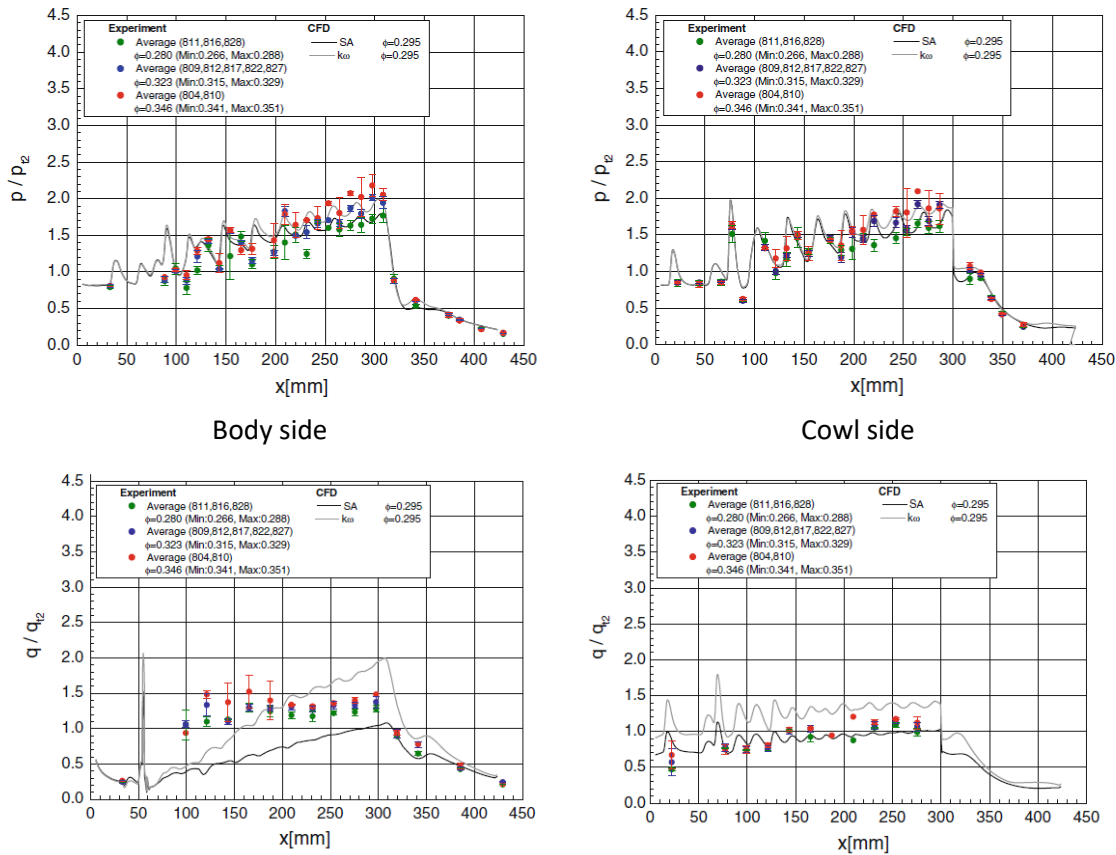


Figure 13 – Normalized experimental pressure and heat-flux for the 28 km test.  $Pt_2=142$  kPa,  $qt_2=4.38$  Mw/m<sup>2</sup> [97].

In blue, the data employed in this work.

Figure 13 summarizes one of the HEG test campaigns. It is interesting noting the equivalence ratios at which the combustor was tested: they are all located in the lean zone. This is related to the unstart or blow-off phenomena which may occur in a scramjet engine. Basically, referring on the theory of the Rayleigh flow, it can be concluded that high heat release can lead to strong flow deceleration, potentially bringing it in the subsonic regime, causing the combustion extinction. Such aspect is crucial in designing and operating a scramjet combustor.

Figure 13 reports, in blue, the data employed in the current study and in Table 3 the free stream conditions. Considering the pressure traces, the shock train is clearly visible: the shock waves reflecting on the combustor walls generate peak values of the pressure. Moreover, a quasi-linear pressure rise can be noticed. A sudden pressure decrease, as expected, is found in the expanding nozzle. Moving the attention on the heat flux, homogeneous values are found on both sides after the fuel injection.

Figure 22 reports the temperature, pressure and velocity distributions at the combustor inlet. Such conditions were evaluated numerically during the HEG experimental campaign [99]. In such way, the combustor can be numerically analyzed by avoiding the computation on the whole vehicle.

| $P_0$ [kPa] | $T_0$ [K] | $V_0$ [m/s] | $m_{H_2}$ [g/s] | $\phi$ |
|-------------|-----------|-------------|-----------------|--------|
| 127         | 1350      | 1720        | 3.7             | 0.32   |

*Table 3 - The average flow conditions examined*

### 3.3 Conclusions of chapter 3

In the concluding chapter, the experimental methods for gathering the data, and the data themselves, employed in the following numerical simulations have been presented.

The experimental pressure, the apparent heat release rate traces and the flame images were acquired on an optically accessible engine fueled with Methane. The engine was tested with and without the TJI system, object of the study. The equivalence ratio and the operating conditions were the same for both the configuration, in order to make direct comparisons of the overall engine performances and the combustion speed possible. The pressure traces, gathered also in motored conditions, will be employed, with the other data (e.g. the equivalence ratio, the engine temperature, the spark advance, the inflow air temperature...) to implement, tune and validate the numerical model.

Considering the nature of the engine, which is not equipped with properly sealant piston rings, mass losses in the high pressure operating phases were not avoidable. Indeed, the pre-chamber configuration showed a significant pressure decrease rate during the early expansion stroke, accompanied by negative values of the aHRR, indicating that leakages are occurring.

Considering this, the computed integrated heat release results smaller for the pre-chamber engine. Nevertheless, the mean indicated pressure values are comparable for both engines and the  $IMEP_{cov}$  results smaller for the pre-chamber configuration.

The flame structure and evolution were evaluated by means of the flame images. The pre-chamber engine shows, at the early stages of the main chamber ignition, particular flame shapes, the so-called mushroom shaped flames. This structure is due to the high momentum proper of the ejected material and is such to involve a considerable portion of the main chamber charge in the ignition phenomena. This, in combination with the high energy and chemical composition of the jets, characterizes the high speed combustion typical of this ignition system, also evaluable by means of the flame images and radii.

The scramjet data were, instead, acquired in a shock tunnel. The free flow conditions were chosen to match the flow Mach number and total enthalpy recorded during one of the few real flights of the combustor. Thanks to the high number of pressure gauges and thermocouples employed in the shock tunnel experiments, the pressure, velocity and temperature distribution at the inflow boundary of the combustor were computed. This data will be employed in the numerical model. The pressure and heat flux recorded during the experiments along the combustor will be compared with the ones obtained numerically and used to tune the numerical model. More specifically, the dataset referred to the flight altitude of 28km was selected. From the experimental pressure traces, a linear increasing tendency can be noted. Moreover, the shock waves reflections were recorded by the pressure gauges. The boundary heat-flux distribution is, instead, more uniform.

## 4. Modeling approach

---

This chapter will describe the model setups in CONVERGE. Before going further, a brief discussion on the meshing strategy of CONVERGE will be performed.

CONVERGE is an immersed boundary CFD solver. This means that the grid is (re)generated, at each iteration, on runtime. To make this automatic grid generation possible, CONVERGE uses a modified cut-cell Cartesian grid generation method. The geometry surface is immersed within a Cartesian block and the meshing algorithm trims the cells at the intersecting surface, after which the intersection information (surface areas, normal vectors, etc.) is reduced before being stored for each cell. With this approach, moving geometries are continuously re-meshed.

Additional density boxes can be added to embed specific portion of the domain. Moreover, the Adaptive Mesh Refinement (AMR) algorithm can dynamically embed local portion of the domain in order to enhance the resolution when it is insufficient without heavily affect the computational costs.

Figure 14 and Figure 15 reports two examples showing the static and dynamic embeddings: in Figure 14, the injection section of the scramjet is embedded, as well as the body and cowl side boundaries; Figure 15 shows the spherical embedding at the pre-chamber lower part and the AMR which surrounds the flames in the main chamber.

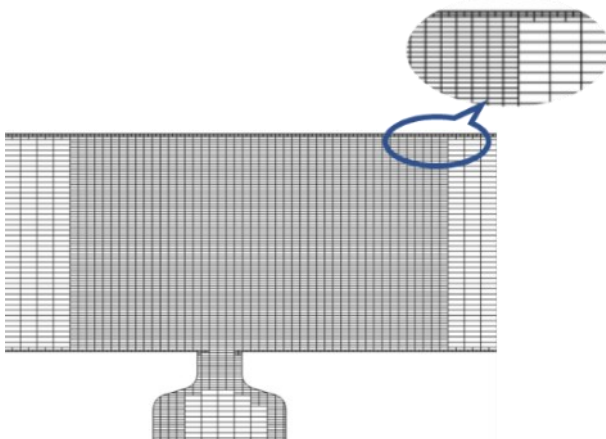


Figure 14 - Example of fixed embedding in a region of the domain and on a boundary



Figure 15 - Example of spherical fixed embedding ad AMR

The mixture is assumed to be a Newtonian viscous fluid with Fourier heat conduction and Fickian species diffusion. The viscosity is computed using Sutherland's law and the thermal conductivity and species diffusivities are evaluated using the viscosity and constant Prandtl and Schmidt numbers, respectively. Each species is considered as a thermally perfect gas, with tabulated formation enthalpies and specific heats. Finally, in the present work, the computations were performed in parallel on a distributed memory machine with Intel Xeon E5 2660v3@2.6GHz processors using the message passing interface.

### 4.1 Engine model setup

Both the pre-chamber and the standard engine configurations were modeled; The computational domains are reported in Figure 16.

The flow was described by solving the Reynolds Averaged Navier-Stokes (RANS) equations, closed by the RNG  $k-\epsilon$  turbulence model, with a centered second-order accurate numerical scheme. The time advance was achieved by an implicit Euler discretization.

Both fixed and dynamic grid embedding were employed. Being the smallest turbulence scale to be solved of the order of 0.1 mm [100], the smallest cell size was set to 0.125 mm in the main and pre-chamber while it was set to 0.5 mm in the intake region. A visualization of the grid during the intake stroke is purposed in Figure 17. In order to limit the computational cost, the maximum number of cells was set to  $4 \times 10^6$  and the base grid dimension was fixed to 4 mm.

A spherical density box was set in the lower part of the pre-chamber, in order to capture the turbulent flow travelling through the orifices. The grid spacing was chosen to achieve at least 4 cells in the diametral direction of each orifice without AMR and 8 when the AMR criteria were met. In the same way, a higher resolution is achieved, at spark time, around the spark-plug. A snapshot of the grid at spark-time is given in Figure 18.

The AMR was triggered when the temperature difference between two adjacent cells was greater than 2.5K or the velocity difference was greater than 1 m/s.

A variable time-step, based on the Courant-Friedrich-Lewy (CFL) number, was used. The maximum CFL ranged between 1 and 5, depending on the region of the domain and on the actual crank angle, with a resulting timestep  $10^{-3} \div 1$  CAD.

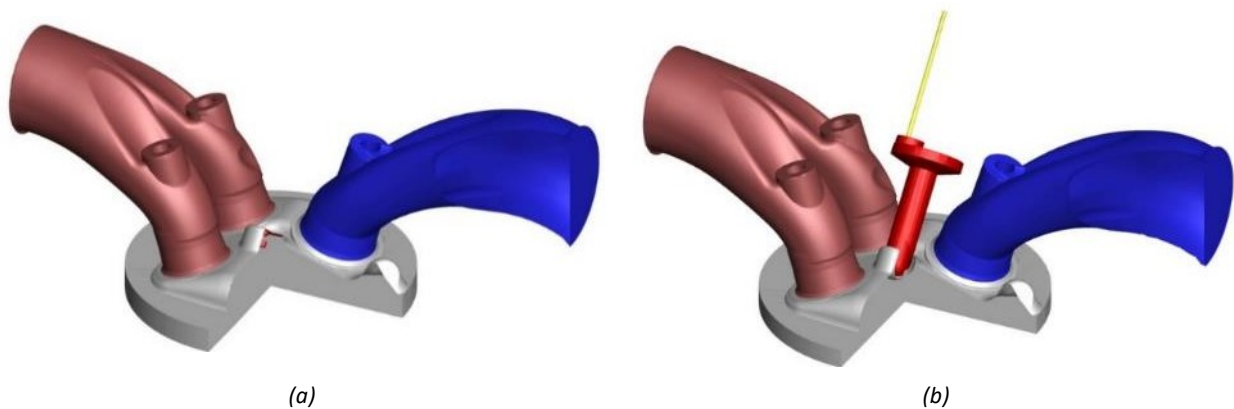


Figure 16- Computational domain for the standard engine (a) and the pre-chamber engine (b).

Combustion was solved with the G-equation method, in order to track the flame-front with the flame-speed model described in section 2.4.2. The oxidation of Methane was described by the Gri-Mech 3.0 reaction mechanism [101], composed of 53 species and 325 reactions. Such mechanism was chosen because although its small sizes it produces reliable results according to the various validations available in literature for several species profiles [102]–[104]. The SAGE solver is called in each region of the flame (burned, unburned and on flame) in order to capture the ignition mechanism of the pre-chamber engine. The overall combustion phase lies in the thin reactions zone of the Borghi diagram. In fact, the pre-chamber is characterized by low turbulence levels, if compared with the main chamber [105].

Ignition was modeled with a 20 mJ [48] spherical shaped energy source placed between the spark-plug electrodes. The source was triggered at spark time and maintained for about 1 ms that, at 2000 rpm, are about 10 CAD.

The flow was initialized as stationary with a post combustion species distribution in the whole domain except for the intake region.

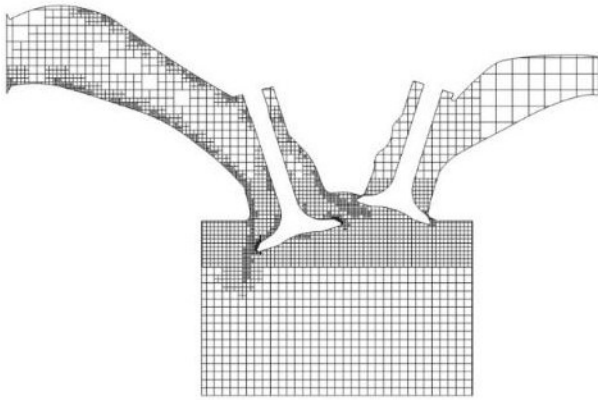


Figure 17- Computational grid during the intake stroke. The AMR effect is noticeable in the intake duct and around the valve angle.

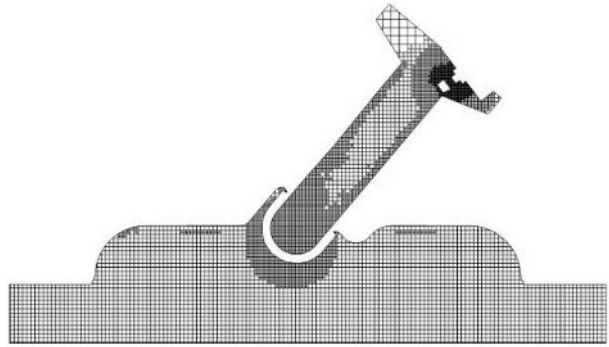


Figure 18- The spherical density boxes around the pre-chamber orifices and spark plug at spark time.

At the inlet boundary, the total pressure and temperature, as well as, the species distribution was imposed as inflow condition, being the injected mass of fuel known from the experiments. For the pre-chamber engine, the fuel concentration at the inlet boundary kept into account the amount of fuel injected in the pre-chamber to achieve the same air-to-fuel equivalence ratio at the exhaust for both engines, as in the experiments. Although the injection duration in the pre-chamber was known, the fuel mass was estimated as the one needed to achieve  $\lambda \approx 1.3$  at the exhaust in the computation. Such assumption was necessary in order to keep into account for the injector dead band. Therefore, Methane injection in the pre-chamber was modeled considering an injection pressure of 8 bar and starting at -150 CAD ATDC, as in the experiments, with a calculated duration of 1.6 CAD. The injector duct, shown in yellow in Figure 16 (b), was also included in the computational domain.

The outflow boundary condition of the exhaust duct was set to ambient pressure. Backflow was allowed and the mixture composition of the backflowing flux was set equal to a burned mixture at a reasonable temperature. The boundary temperatures were chosen accordingly with the experience of the working group.

The motored cycles were employed to tune the compression ratio of the modeled engine. The achieved compression ratio and the crevice model constant were then adjusted by comparing the compression stroke of the modeled fired engine with the fired experimental pressure traces.

11 consecutive fired cycles were modeled for both engines. The results were evaluated discarding the first cycle. Moreover, a crevice model was employed to keep into account for the mass losses from the main chamber. Such model is introduced in the following sub-section.

It is worth to mention that all the parameters and model constants are the same for both engine setups.

#### 4.1.1 The crevice model

A crevice model, an auxiliary model, is able to simulate the flow occurring between the cylinder, the piston and the piston rings. It can be employed to track and consider the blow-by losses of a piston-cylinder assembly, in particular in the present case in which an optical engine, which is not equipped with properly sealant piston rings, is analyzed.

CONVERGE contains the model proposed by Namazian and Heywood [106]. In this model, 5 regions are defined. Region 1 represent the cylinder while region 5 is the crankcase. Regions 2 and 4 represent the ring sits and region 3 is the piston-cylinder gap zone, as schematized in Figure 19.

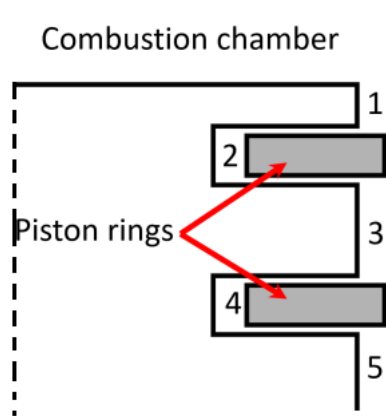


Figure 19 - Schematization of the crevice model regions

The mass flowrate occurring between each region can be evaluated accordingly with the following equation:

$$\dot{m}_{ij} = \frac{Ah^2}{24W_r} \frac{1}{\mu RT} (P_i^2 - P_j^2)$$

Where  $A$  is the area normal to the flow, approximated as  $\pi \cdot bore \cdot h$ ,  $h$  is the channel width,  $W_r$  is the channel length and  $T$  is the crevice-zone temperature.

Depending on the regions of interest, the channel can be either the ring sit or the piston-cylinder gap.

Region 1 is at the cylinder pressure while region 5 is assumed to be at the atmospheric pressure. The crevice-zone temperature is assumed equal to the end of compression temperature.

The flowrate between the ring gaps is instead evaluated as

$$\dot{m}_{ij} = C_d \rho c \eta A_{ij}$$

Where  $C_d$  is the coefficient of discharge of the orifice,  $A_{ij}$  is the ring end gap area,  $c$  is the speed of sound and  $\eta$  is the compressibility factor evaluated considering the mixture as air.

Considering the nature of the actual rings, the rings motion was not allowed.

The rings dimensions were taken from a catalog, being the actual unknown. By virtue of this, to reduce the uncertainty, the only tuned parameter was the coefficient of discharge of the orifice.

## 4.2 Scramjet model setup

A snapshot of the quoted computational domain is given in Figure 21. Referring to Figure 20, air, at  $M \approx 2.4$ , enters the domain through the rectangular area on the left side of the assembly after passing through the intake ramp (not modeled). Gaseous Hydrogen is injected by four port-hole injectors placed on the lower side of the combustor.

Thanks to its symmetry, only one-eighth of the combustor, comprising a half of one injector, was modeled.

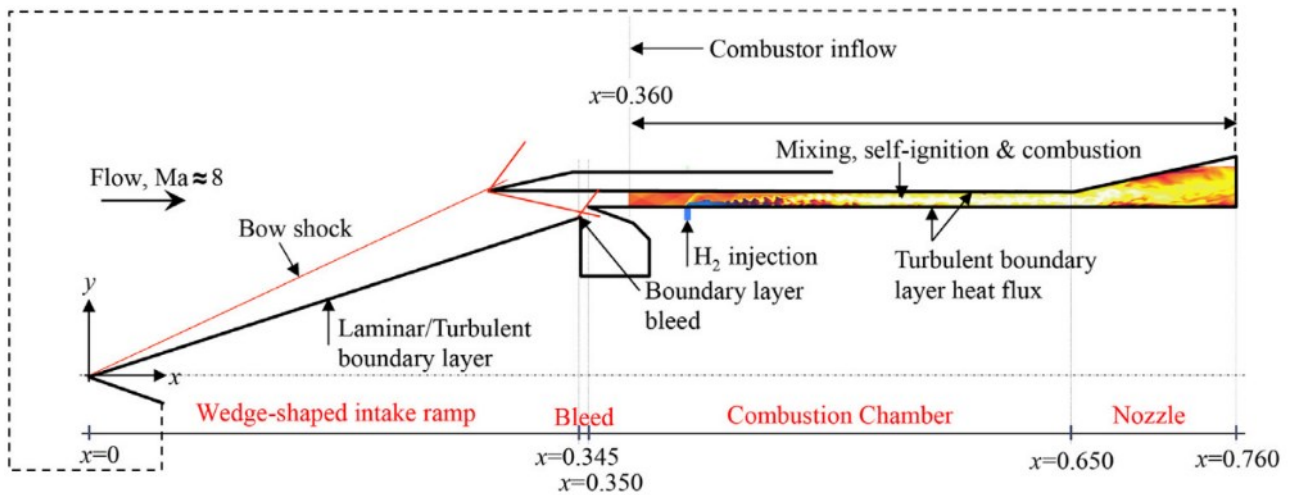


Figure 20 - Highlight of the numerical domain on a symmetry cut of the experimental assembly [82].

The flow was modeled with the LES approach, using the dynamic Smagorinsky SGS model – cf. Section 2.3.2.

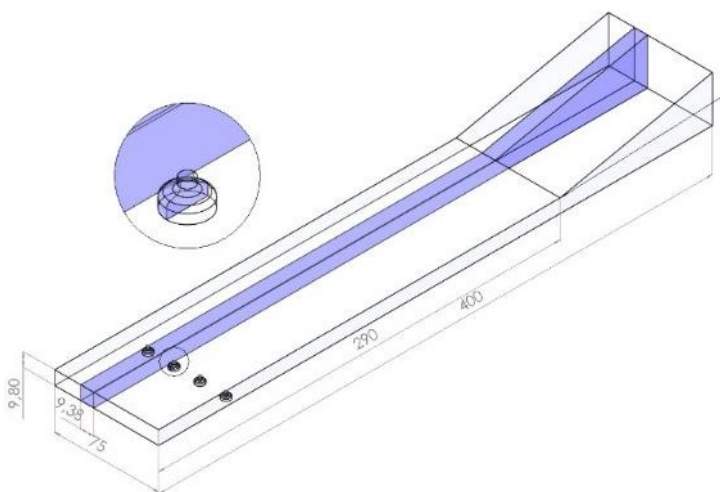


Figure 21 – Perspective of the scramjet computational domain

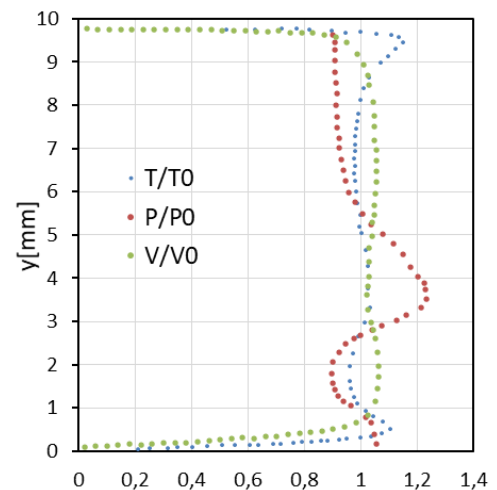


Figure 22 - Combustor Inlet conditions [99]

The symmetry boundary condition was applied in the spanwise direction of the combustor, while iso-thermal no-slip boundary condition was applied on the upper and lower side of the combustion chamber. The wall temperature was fixed to 300 K [82]. To model the flow-wall interaction, the Werner and Wengle wall function [107] was employed.

At the inflow boundary, the pressure, temperature and velocity distribution reported in Figure 22 were applied in the normal direction and air was the entering fluid. The outflow conditions were extrapolated from

the domain.

Hydrogen injection was modeled with a total pressure and temperature boundary condition. The value of the total pressure was analytically calculated and then adjusted in order to match the experimental Hydrogen flowrate and its combustion was modeled with the 10 species 21-step reaction mechanism of O' Conaire et al. [108] solved by the SAGE chemical solver.

The base computational grid dimensions were chosen following the aspect ratio of the combustor, employing  $\frac{dx}{dz} = 2$  and  $\frac{dy}{dz} = \frac{5}{3}$ , as can be observed in Figure 14. A density box was placed in the injection zone, to better capture the complex flow pattern. Moreover, the AMR algorithm, triggered by a temperature difference of 0.5 K, was enabled on the whole domain. The smallest cell dimension was in the order of 0.05mm and the maximum number of cells was fixed to  $80 \times 10^6$ .

A centered second-order accurate spatial discretization was employed with the Crank-Nicolson method for the time advancement. Also in this setup, a variable time-step based on the CFL number was employed and the computation was initialized with the flow conditions given in Table 3.

### 4.3 Conclusions of chapter 4

In chapter 4, the modeling approach, by means of the commercial software CONVERGE CFD, of the two applications was described. CONVERGE is an immersed boundary CFD solver which integrates different turbulence and combustion models. In the present work, two different turbulence and combustion models were employed in the analyzed applications.

In the engines models, the flow was modeled with a RANS approach and the combustion with the G-equation model. The laminar flame speed of Methane was described with a correlation purposed by the workgroup and implemented in the code by means of a user defined function while the species conversion was described with the Gri-Mech 3.0 reaction mechanism. Total pressure and temperature and the mixture composition were set at the inflow boundary. The exhaust outflow boundary pressure was set to the atmospheric value and temperature and species distribution of a complete combustion were included in case of backflow. The walls temperatures were set, basically, referring to the experience of the workgroup. Finally, the Methane injection (for the modified engine) was modeled by imposing the total pressure at the injector duct boundary and the timing was determined by matching the engine overall equivalence ratio, being the injected mass value not reliable.

The computational grid was developed by exploiting the adaptive mesh refinement algorithm of the software. Moreover, additional density boxes were included in the crucial zones of the domain, as around the spark or at the pre-chamber orifices.

The scramjet combustor was, instead, modeled with LES approach. The combustion, which proceeds prevalently in a non-premixed regime, was modeled by solving the reaction mechanism, based on 10 species and 21 reactions, in each cell of the domain. The static pressure and temperature and the velocity distributions were set as inflow condition at the combustor entrance. The outflow conditions were extrapolated from the domain while the Hydrogen injection was modeled by imposing the total pressure and temperature at the injector inflow boundary.

The walls temperatures were set accordingly with the literature articles chosen as reference. Also in this case, the adaptive mesh refinement was employed to refine the mesh locally, where the velocity and temperature gradients were stronger.

For both the models, an adaptive time step, based on the CFL criteria, was used. Moreover, in both computation the spatial discretization was performed through a second order centered scheme. The time advance was modeled with a first order implicit Euler scheme, for the engines, and with a second order Crank-Nicolson scheme for the scramjet.

## 5. Engine simulations results

This chapter opens with a preliminary validation and discussion on the modeled standard engine will be performed; then, a detailed analysis of the pre-chamber engine will be presented.

### 5.1 The standard engine

After having tuned the compression ratio of the optically accessible engine with the motored cycles, a finer tuning was performed against the fired experimental cycles. The crevice model parameter, i.e. the orifice discharge coefficient, was also adjusted.

Figure 23 reports the comparison of the experimental and numerical pressure and net Heat Release Rate for the standard engine. The light blue lines represent the variability range in the 10 consecutive modeled cycles. As can be observed, the compression stroke is well captured.

Moreover, the slopes of the nHRR traces are similar, thus also the early stages of the flame development acceptably agree, as well as, the propagation speed- $c_f$ . Figure 24. The combustion phase, anyway, appears to be globally a bit in early.

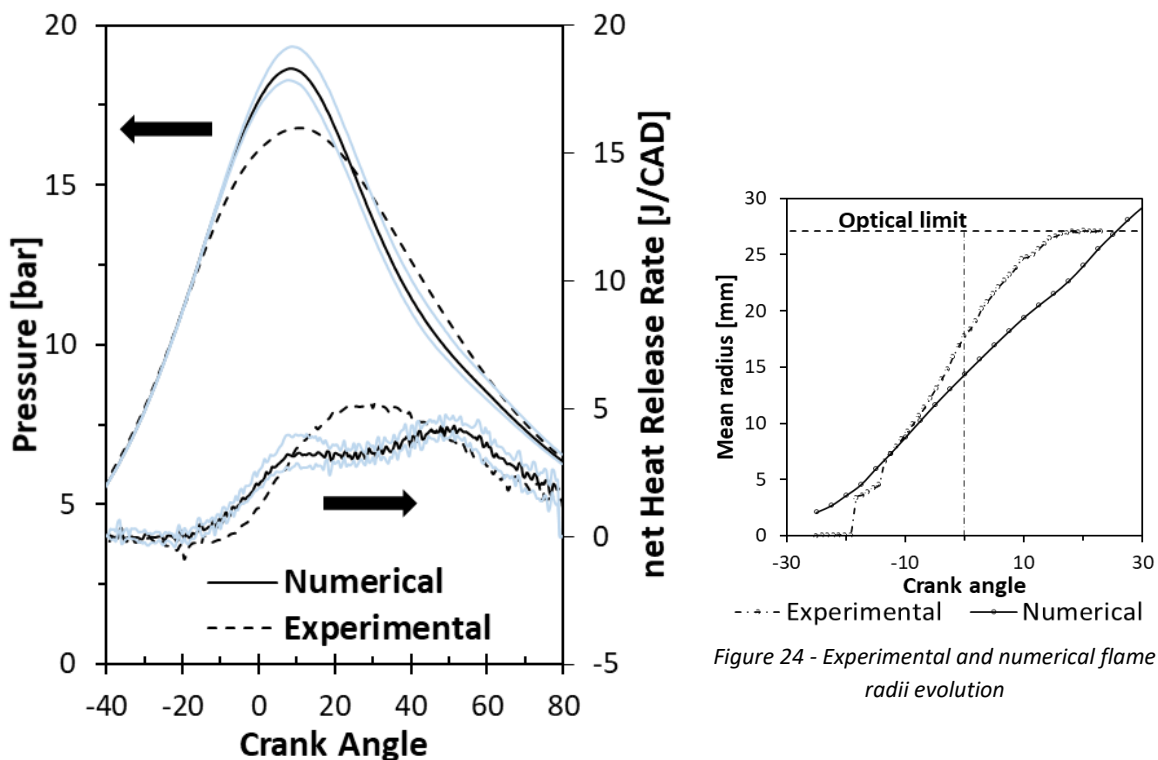


Figure 23 - Comparison of the computed and experimental pressure and net HRR traces, Standard engine. The solid blue lines represent the variability range in the 10 modeled cycles.

Figure 24 - Experimental and numerical flame radii evolution

A better agreement between the pressure traces would have been possible with a finer tuning of the crevice model but this was not the aim of the present work. Moreover, a loss of generality could occur, considering that the employed crevice model was not intended for being applied on an optically accessible engine.

|                     | IMEP [bar] | IMEP <sub>cov</sub> | Work[J] | IaHR[J] |
|---------------------|------------|---------------------|---------|---------|
| <b>Experimental</b> | 3.32       | 7.4                 | 83      | 278     |
| <b>Modeled</b>      | 3.24       | 3.3                 | 81      | 272     |

Table 4 - Comparison between the experimental and modeled engines performance, Standard engine

Table 4 compares the summarized performance of the experimental and modeled engine. The values are comparable.

Finally, emissions productions were computed. They are reported in section 5.3 - Engine out emissions, in comparison with those calculated for the pre-chamber engine.

## 5.2 The pre-chamber engine

After “having installed” the pre-chamber, a new tuning iteration of the compression ratio was performed. All the other coefficients were not modified, in order to maintain a general validity of the numerical setup.

The comparison between the experimental and numerical pressure and nHRR traces, evaluated in the cylinder, for the pre-chamber engine is purposed in Figure 25. Also in this case, the compression stroke is well captured.

The flame development process in the pre-chamber and the subsequent main charge ignition appears to be a bit in early with respect to the experiments. Nevertheless, the numerical and the experimental pressure traces are in good agreement until the pressure peak.

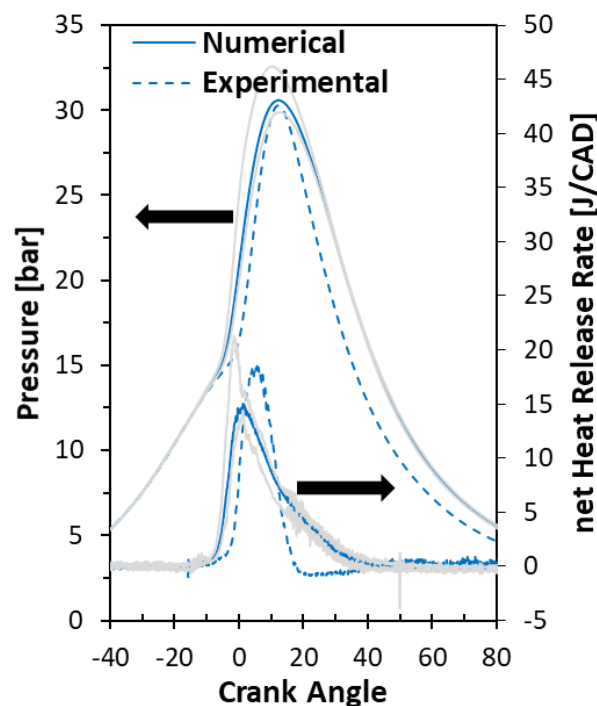


Figure 25 - Comparison of the computed and experimental pressure and net HRR traces, Pre-chamber engine. The solid light grey lines represent the variability range in the 10 modeled cycles.

Soon after the pressure peak, both pressure and the computed net Heat Release Rate sudden decrease, due to the mass leakage mentioned in section 3.1. The gentler slope of the numerical nHRR and the higher pressure trace in the expansion stroke are related to an under-estimation of the mass losses. It needs to be underlined that the crevice model here employed was not developed for application like the one here treated and that the aim of the following analysis is to provide a general analysis approach of the combustion process related to TJI systems.

|                     | IMEP [bar] | IMEP <sub>COV</sub> | Work[J] | IaHR[J] |
|---------------------|------------|---------------------|---------|---------|
| <b>Experimental</b> | 3.46       | 2.9                 | 86      | 210     |
| <b>Modeled</b>      | 4.64       | 0.41                | 116     | 279     |

Table 5 - Comparison between the experimental and modeled engines performance, Pre-chamber engine

A comparison between the performance indicator of the modeled and experimental pre-chamber engine is purposed in Table 5. As could be expected, the indicators of the modeled engine are better than the experimental ones. The Integrated apparent Heat Released is, instead, similar to the standard engine one, as the experiments were designed for.

For a comparison purpose, also the IMEP<sub>COV</sub> values are reported. Beside the fact that the RANS approach is not properly suitable to estimate or predict many of the fluctuations associated with COV, the values computed reflect the behavior of the real engine. As can be noticed, the pre-chamber is able to reduce the cycle-to-cycle variability.

### 5.2.1 Preliminary analysis

All the characteristics operating phases of an active TJI system are summarized in Figure 26. The stream-line pattern evolution, colored with the velocity, is reported with the TKE colored contour while the timings of each phase are summarized in Table 6.

The SOI in the pre-chamber, at -150 CAD, corresponds to the beginning of the *filling* phase of the pre-chamber. After the injection start, Methane takes about 0.5 CAD to travel the injection duct and reach the pre-chamber. Such injection causes the ejection of a portion of the residual gasses remained in the pre-chamber, as shown by the stream-traces in Figure 26 (a). Therefore, the filling phase and the *scavenging* one are closely related. During the scavenging, also some fuel leaves the pre-chamber. It is worth noting that, despite the high turbulence promoted by the injection, its duration is too short to globally increase the turbulence levels in the whole pre-chamber.

The successive *mixing* phase begins when the pressure in the main chamber becomes higher than the one in the pre-chamber, around -134 CAD. In this stage, the lean mixture of the cylinder is pushed inside of the pre-chamber causing, by one hand, the dilution of the rich fresh charge and, by the other, a slight increase of the turbulence levels. A vortex favoring the mixing between the rich and the lean charge can be identified in Figure 26(b). Such structures, which plays a crucial role in promoting mixing, are induced by the orifice orientation. Indeed, the absence of symmetry in the orifice orientation promotes the formation flow patterns with different velocity (cf. also Figure 41), leading to the formation of the before mentioned vortices. However, as the mixing goes on, the turbulence levels keep remaining globally low, especially at spark time in the neighborhood of the spark-plug, as shown in Figure 35.

Soon after the spark, at -22 CAD, the *propagation* stage begins. A flame-front rapidly develops and propagates through the pre-chamber, pushing in the main chamber the content of the pre-chamber. The before introduced vortices get compressed by the descending flow, as showed in Figure 26(c) The propagation phase concludes when the flame reaches the orifices. The *ejection* stage, instead, begins when the flame is still propagating and ends a couple of CADs after the end of the propagation stage, when the pressure in the main chamber gets higher than that in the pre-chamber. During the ejection, high energy jets are generated from the pre-chamber. The high turbulence levels proper of such jets promotes the mixing between the hot and reacting material composing the jets and the fresh lean mixture, causing the ignition and favoring a fast combustion. The extension of the area of influence of the jets can be estimated by the stream-traces showed in Figure 26(d): the circulation bubble extends reaching the clearance volume.

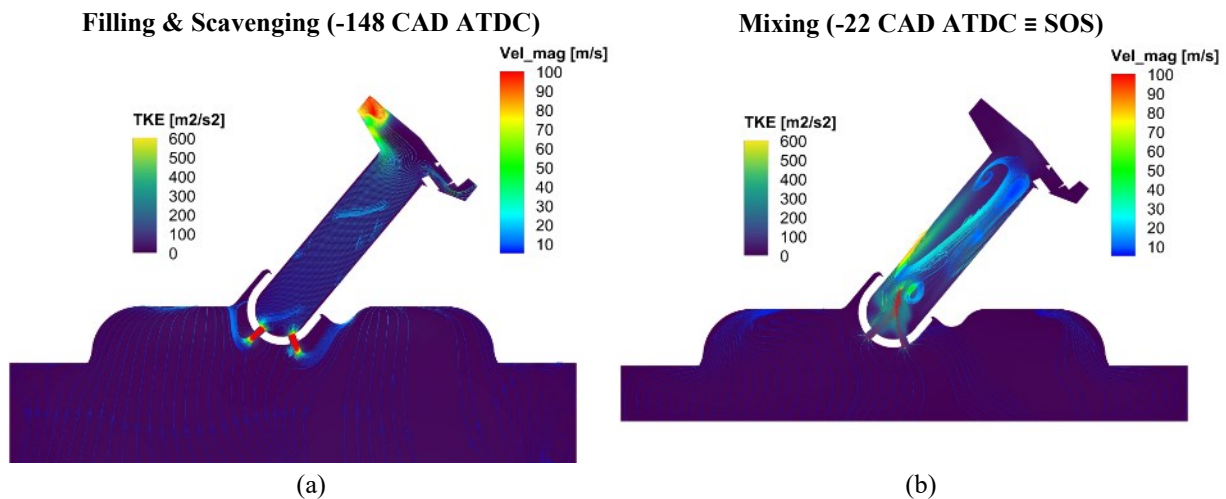
At the end of the ejection phase, the main combustion is already in progress. The pressure in the main chamber rapidly overcomes the one in the pre-chamber, causing a flow inversion which pushes material – mainly fresh charge- from the main to the pre-chamber. Such event triggers the so-called *reburning* phase. Reburning runs like a flameless combustion, promoted by the sufficiently high turbulence levels in the pre-chamber. Also in this phase, the orifice orientation promotes, with a minor intensity with respect to the mixing stage, the internal mixing of the pre-chamber mixture, as shown in Figure 26 (e). The minor pressure rise makes some product being ejected when the main combustion is approaching the end; the remaining will be ejected during the expansion stroke. No particular flow patterns are identified in this stage. Indeed, the stream-traces, reported in Figure 26(f), are quite straight.

Summarizing, 6 distinct phases can be highlighted, timed by 5 flow reversing events.

| Phase                  | Start      | End      |
|------------------------|------------|----------|
| Filling & Scavenging   | -150 (SOI) | -134     |
| Mixing                 | -134       | -22      |
| Flame Propagation      | -22        | -7       |
| Ejection               | -14.4      | -4       |
| Reburning              | -4         | 16       |
| Expulsion & Extraction | 16         | 97 (EVO) |

Table 6 - Operational phases and timings of the pre-chamber

By evaluating the pressure evolution separately in the pre and in the main chamber, Figure 27, three intersection points are found. Such points indicate 3 of the 5 before mentioned flow reversing events.



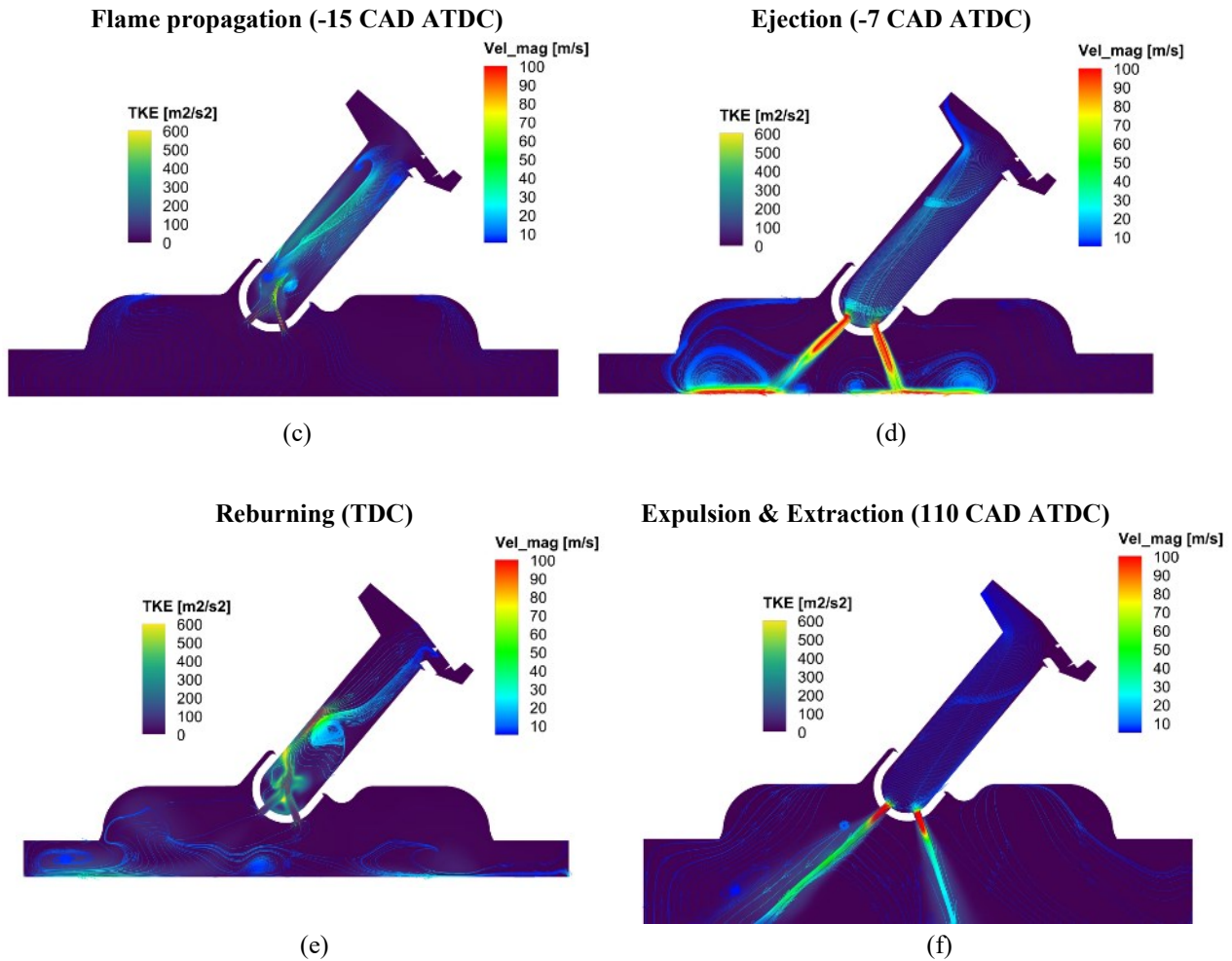


Figure 26 - Evolution of the streamline pattern and contours of the Turbulent Kinetic Energy (TKE) on a longitudinal plane, reported for each of the operational phases of the active pre-chamber.

The net Heat Release Rate is computed accordingly with Equation (16).

About 8 CAD after the spark (-22 CAD) the pressure in the pre-chamber overcomes the pressure of the main chamber, which was increasing mainly due to the compression, and the ejection begins. The pressure peak in the pre-chamber is achieved around 15 CAD after the start of spark and the second flow reverse event, the reburning one, is located about 4 CAD BTDC. Between these two flows reversing events, the ignition of the main charge occurs, as can be noticed by observing the nHRR of the main chamber in Figure 27.

The pressure of the main chamber increases and quickly reaches its peak value, around 12 CAD ATDC. The pressure increase in the pre-chamber follows that recorded in the main chamber, basically for two reasons: firstly, the presence of the orifices, and secondly the main combustion in the pre-chamber is already completed, as indicated by the mass-burnt fraction evolution reported in Figure 28. Thus, the slope change of the pre-chamber pressure trace, located in Figure 27 near the second flow reversal event, is due to unburned charge being pushed in the pre-chamber from the main chamber, as stated also by the mass-burnt fraction evolution, cf. Figure 28. Indeed a slope change can be noticed at the before mentioned time.

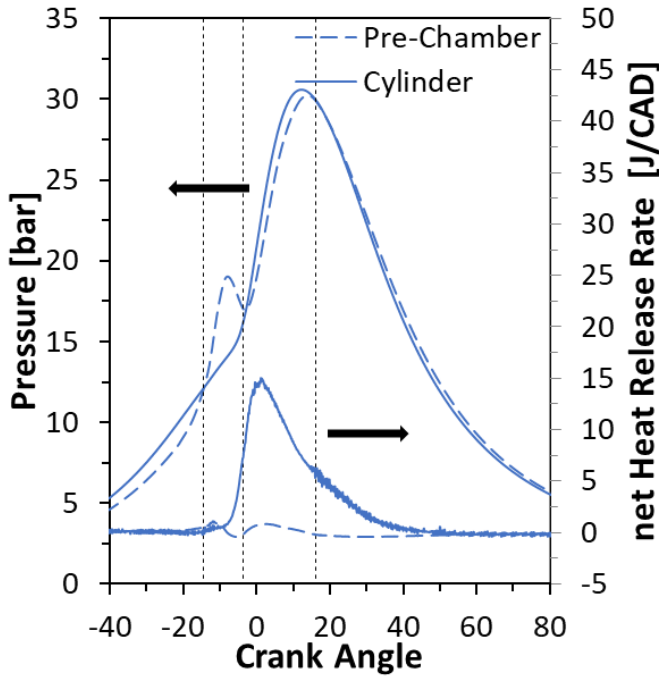


Figure 27 - Pressure and net Heat Release Rate in the pre and main chamber. Dashed, the three flow reversal events.

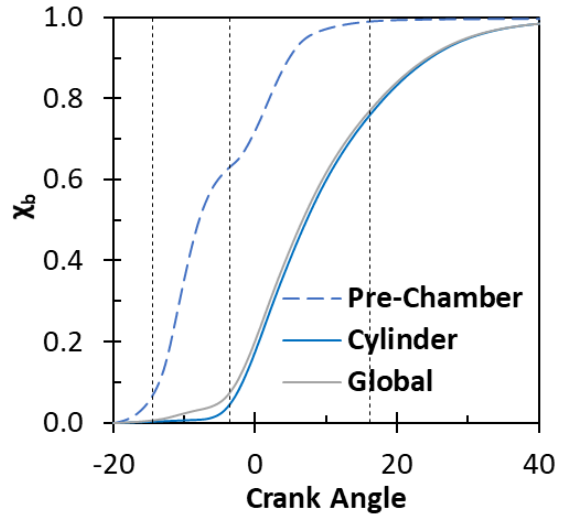


Figure 28 - Mass burnt fraction

The negative values of the nHRR traces purposed in Figure 27 can be inferred to the assumption behind Equation (16). Indeed, such equation is valid for a closed system (like a conventional engine can be assumed) and doesn't complain mass transfers.

The red trace in Figure 29 reports the overall flow rate between the pre-chamber and the cylinder. Considering that, at spark time, the pre-chamber contains about the 5% of the total mass and the peak value of the flow rate, the pre-chamber effect on the main chamber thermal balance can not be neglected.

It is possible to replace Equation (16) with a more general one, as the following:

$$\frac{dQ_{chem}}{d\theta} + \dot{m}_o h_o - \frac{dQ_{walls}}{d\theta} = \frac{1}{k-1} V \frac{dp}{d\theta} + \frac{k}{k-1} p \frac{dV}{d\theta} \quad (20)$$

Where  $Q_{chem}$  represents the energy released by the chemical reactions,  $Q_{walls}$  the heat losses through the combustion chamber walls and  $\dot{m}_o h_o$  is the total energy flux exchanged by the orifices. The sum of these three terms gives the so-called *net* Heat Release Rate [109]. By neglecting the energy exchange through the chambers, Equation (18) is retrieved.

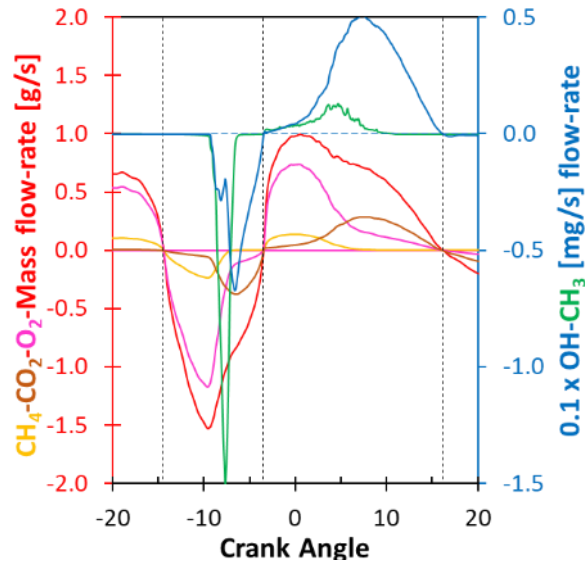


Figure 29 - Total flowrate N2 excluded, red; O2 flowrate, magenta; CO2 flowrate, brown; CH4 flowrate, yellow; CH3 flowrate, green; 0.1xOH flowrate, blue. Dashed, the flow reversal events. When positive, the flow is toward the main chamber.

The single contribution of the first two terms of the LHS of Equation (16) and the net HRR are reported in Figure 30 for the two chambers.

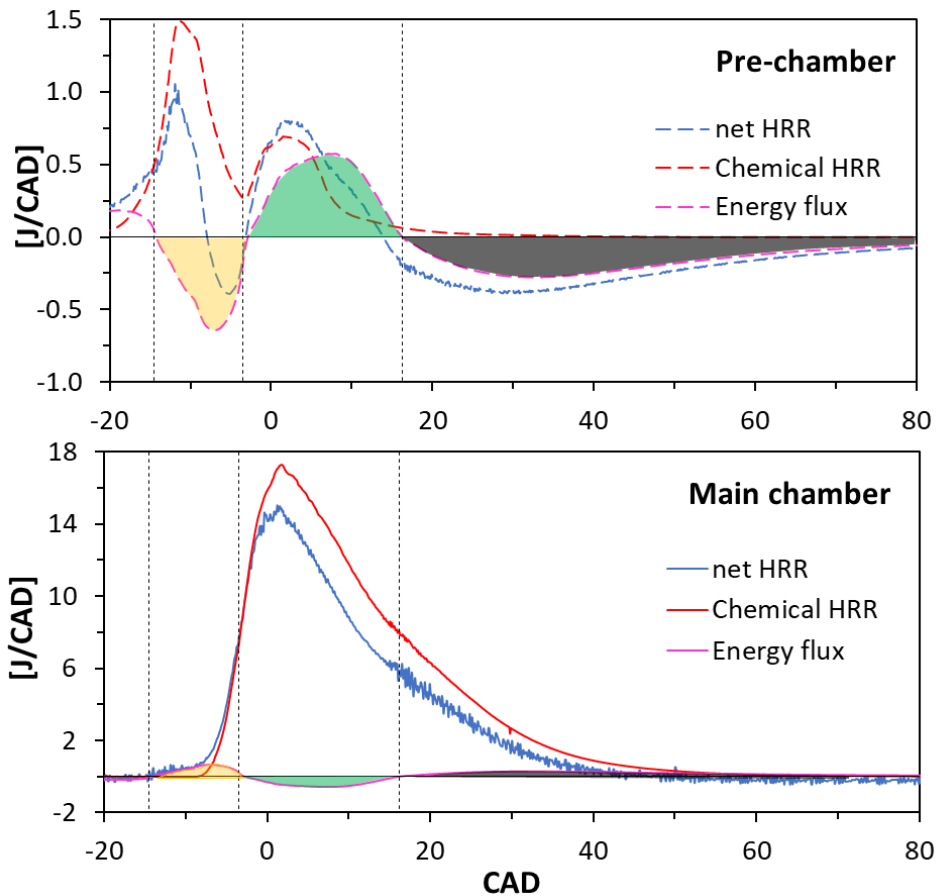


Figure 30 - Contribution to Equation (16) evaluated in the pre and main chamber

Considering the pre-chamber, the pressure peak is achieved in correspondence of the chemical HRR peak – cf. Figure 27 and Figure 30- while the negative values of the net HRR are obtained when the leaving energy is higher and the chemical HRR is lower. It can be noticed also a positive energy flux, after the second flow

reversing event, due to some high temperature material flowing toward the pre-chamber. Moreover, a second peak in the chemical HRR is noticed and represents the reburning phase. Finally, in the early expansion stroke, the exothermal chemical reactions in the pre-chamber are terminating and the pressure in the main chamber is getting lower. In this phase the pre-chamber releases the remaining part of energy. Moving the attention on the main chamber, one can observe that the initial portion of the net HRR is represented just by the energy flux leaving the pre-chamber. Indeed, the chemical HRR in the main chamber is negligible until about -8CAD ATDC, evidencing that the energy furnished, by the pre-chamber, to ignite the main charge is not negligible in an overall energy balance (typically, the kernel development process is not visible on a net HRR trace in a conventional SI engine). A rough estimation of the ignition delay - considering it as the delay between the positive heat flux and the positive chemical HRR in the main chamber – results in about 6 CAD, namely, about 5 ms. Such a value is in the low range of experimentally measured values, in similar initial conditions, discussed in [110].

Moreover, the energy available for the main charge ignition (yellow area of Figure 30) can be estimated to be around 4.4 J, about two orders of magnitude higher than a conventional spark-plug [48]. The energy entering the pre-chamber close to the re-burning stage (green area of Figure 30) and the energy released during the expansion stroke (dark area of Figure 30) are estimated to be -7.2 J and 11.4 J, respectively. It is worth noting that the sum of these 3 terms is positive.

The single phases will be now discussed.

### 5.2.2 The filling and scavenging phases

In a typical engine architecture, the scavenging phase is located between the exhaust and the intake stroke. However, when an additional fixed volume, as the pre-chamber, is connected to the cylinder, such volume will not participate to the main chamber scavenging. Therefore, for an active pre-chamber the scavenging phase begins with the start of fuel injection. As Figure 31 and Figure 32 show, the fuel injection promotes the ejection of the residual gasses from the pre-chamber. Indeed, less of the 15% of the CO<sub>2</sub> (assumed to be representative of the residual gasses fraction) present in the pre-chamber at the Exhaust Valve Opening (EVO) time leaves it during the main chamber scavenging process.

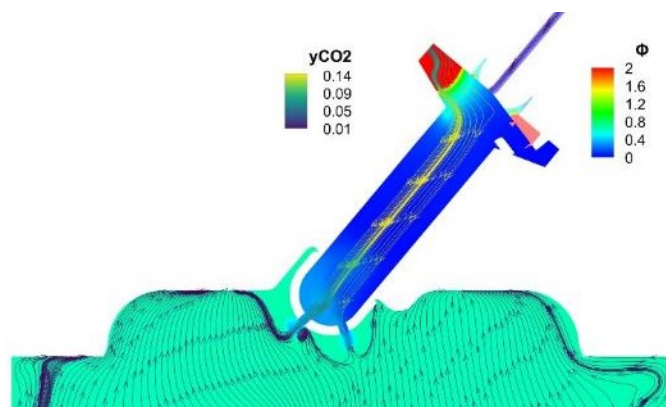


Figure 31 - -148CAD, Early scavenging phase in the pre-chamber; SOI= -150CAD

The residual fraction, standing to Heywood [94], can be defined as the ratio between the molar concentration of CO<sub>2</sub> at the Intake Valve Closing (IVC) time and the same evaluated at the EVO time, that is, the residual gas, represented by CO<sub>2</sub>, at the spark time (neglecting the blow-by losses) over the residual produced at the previous cycle. Keeping in mind the consideration about the scavenging of the pre-chamber, the residual fraction should be intended as the ratio of the residual at the spark time over the residual at the beginning

of the scavenging phase, that is, at the start of the injection:

$$x_r = \frac{(\overline{x_{CO_2}})_{spark}}{(\overline{x_{CO_2}})_{SOI}} = \frac{(Y_{CO_2})_{spark}}{(Y_{CO_2})_{SOI}} \approx 16\%$$

Such high values are typical of larger pre-chambers. It seems, anyway, to have no implications on the overall engine out emissions [63], [72], [111]. On the contrary, such behavior helps to contain unburned hydrocarbons in the pre-chamber rather than ejecting them [112], [113].

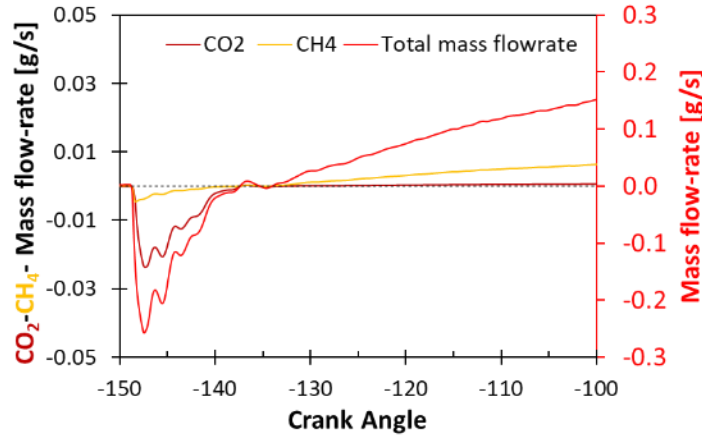


Figure 32 - Total, CO<sub>2</sub> and CH<sub>4</sub> flow-rate between pre-chamber and main chamber

Figure 33 reports the actual residual fraction against time. As can be noticed, it diminishes as the compression goes on, both thanks to the dilution with fresh charge and to some residual being pushed into the injector duct.

Finally, during the scavenging phase also some fuel, around the 2% of the injected, leaves the pre-chamber.

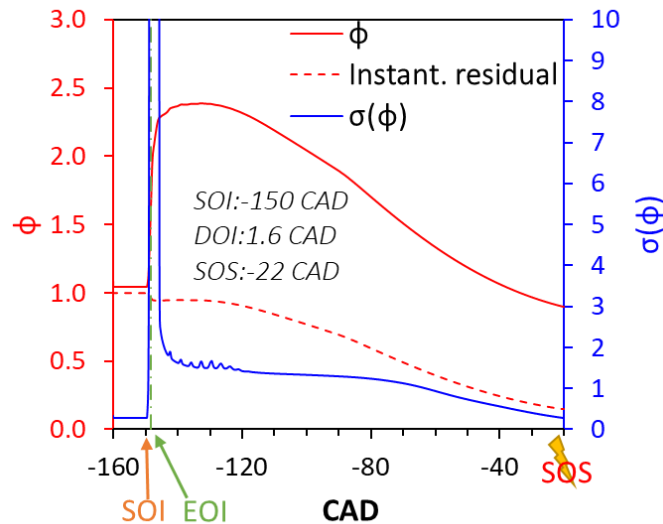


Figure 33 - Instantaneous residual fraction and equivalence ratio and its standard deviation in the pre-chamber

### 5.2.3 The mixing phase

Mixing is a fundamental step in any premixed combustion phenomena. Its duration depends on the local chemical (pre-ignition) and flow characteristics (species transport). When dealing with a volume characterized by low circulation capabilities and low turbulence levels, as the pre-chamber, it becomes

crucial and ensuring a good mixing is challenging.

As discussed in the previous sub-section, the scavenging phase starts with the pre-chamber injector opening. Moreover, during the main chamber scavenging, the mixture remained trapped in the injector duct expands. In this way, burned, unburned mixture and fresh fuel, reach the pre-chamber in this order.

Figure 33 reports the actual equivalence ratio and its standard deviation in the pre-chamber.

When the pressure in the main chamber becomes higher than that in the pre-chamber – a few CAD after injection, cf. Figure 32- the mixing phase begins.

During the compression stroke, the main chamber lean charge is pushed into the pre-chamber, diluting the mixture there contained and promoting the charge stratification.

In Figure 34 is purposed the binned distribution, evaluated on mass base, of the equivalence ratio in the pre-chamber at spark time. Comparing such distribution with the contour showed in Figure 35, it can be noticed that the leaner charge is located in the lower part of the pre-chamber while the richer is in the upper one. Around the spark, favorable conditions of equivalence ratio are found.

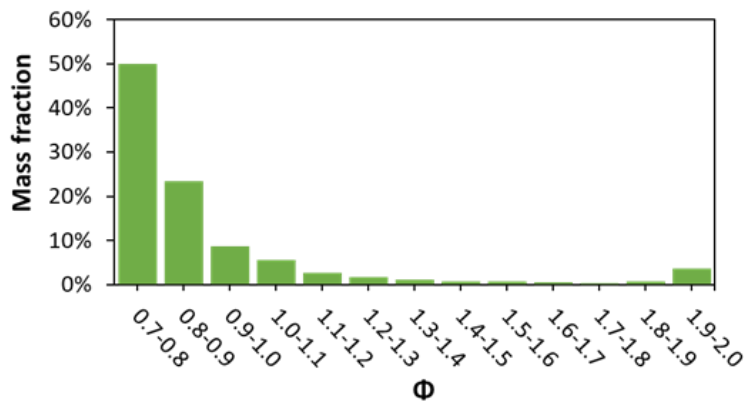


Figure 34 – Mass based binned distribution of the equivalence ratio in the pre-chamber at spark time

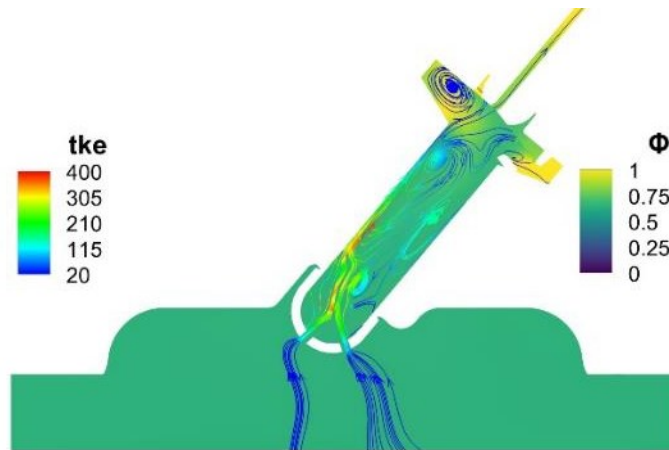


Figure 35 - Equivalence ratio and Turbulent Kinetic Energy [m2/s2] distribution in the pre-chamber at spark time

Moreover, part of the rich charge has been pushed in the injector duct during the compression and will be released part in the actual cycle and part in the next one. Figure 36 summarizes the mixture condition at spark time, reporting the iso-surfaces of  $\Phi=1$  and  $x_{\gamma}=16\%$  at spark time. The stoichiometric regions, colored in red, occupies the spark side of the annular top region and the central zone of the cylindrical duct. Between the  $\Phi=1$  iso-surface and the top boundary and lower cylindrical zone of the duct there is the  $x_{\gamma}=16\%$  zone. It is worth to mention that the residuals occupy both the upper and the lower part of the pre-chamber.

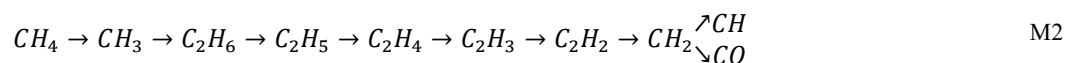
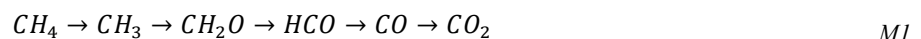


Figure 36 – Red, iso-surface of equivalence ratio=1; green, iso-surface of residual fraction=16% at spark time

## 5.2.4 Combustion phase

Such macro-stage comprises all the phases from spark time to the expulsion. Therefore, a unique discussion will be performed. The combustion in the pre-chamber, the main charge ignition, as well as, the fuel conversion mechanism will be analyzed by means of energy balances, volume averaged species evolution and on-line averaged distributions. Three group of lines are, indeed, employed to track, both in space and in time, different variables. The first group of lines is located inside of the pre-chamber and is parallel to the pre-chamber axis. Such lines have all the same length. The second group is located in the lower part of the pre-chamber and each line is orthogonal to the corresponding orifice. The starting point of this lines is in the center of the hemispherical lower portion, on the same plane of the ending point of the previous 4 lines. Each line ends when a solid boundary (the engine head, the piston or a valve) is encountered. The last group of lines is located in the cylinder. The lines are connected to the previous and terminates on the piston. The lines of the last two groups have, therefore, different lengths, as shown in Figure 37.

The oxidation path followed by Methane can be divided into two macro reaction pathways [91]:



The first one, *M1*, represents the path of a lean to stoichiometric oxidation. The second, *M2*, is representative of a rich oxidation. In this rich case, the large availability of  $CH_3$  radicals makes possible its recombination to  $C_2H_6$ , opening the way to the  $C_2$  oxidation mechanism, as outlined through the mechanism *M2*. By following such paths and by means of the species distribution, one is able to track the combustion process and gather information about the ignition and species conversion mechanisms.

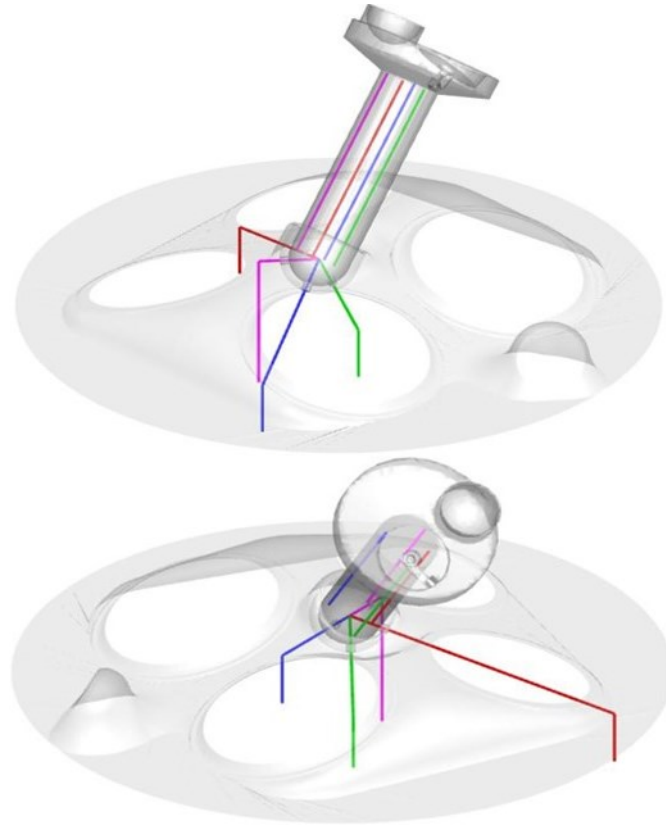


Figure 37 - Monitoring lines definition

In the pre-chamber mixing ends when combustion is initiated, at -22 CAD ATDC, and a flame starts to propagate within it (cf. Figure 38(a)). The burned gases rapidly expand, so that the unburned mixture ahead of the flame front is compressed and forced to be ejected from the pre-chamber- cf. Figure 29. Although the piston has not completed yet the compression stroke, at -14.4 CAD ATDC a flow exiting from the pre-chamber is established. In Figure 29, the mass flow rates through the pre-chamber orifices of some representative species are also reported, showing that unreacted Methane, as well as active radicals (i.e.,  $OH$ ,  $CH_3$ ) and intermediate species (like  $CH_2O$ ) leave the pre-chamber in this phase. The interval between the first two flow reversal events is also known as *residence time* and its duration is crucial in determining the generation of active radicals in a sufficient amount for the ignition of the main charge. During this interval, in which the combustion is limited to the pre-chamber, heat is released and the pressure rises in this confined ambient, as shown in Figure 27 and Figure 30.

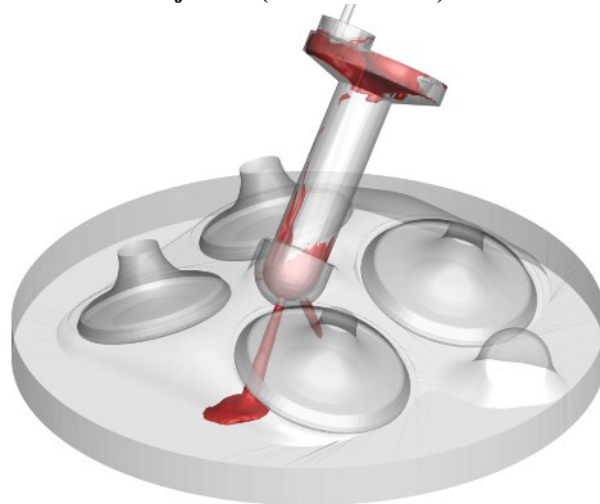
Figure 39 shows the volume averaged evolution of the main species and radicals in the pre-chamber. As can be observed, soon after the spark, Methane is rapidly oxidized to form  $CO$  and  $CO_2$ . Accordingly, the Oxygen fraction decreases rapidly. Moreover, a large quantity of radicals -  $H$ ,  $O$ ,  $OH$ ,  $CH_3$  - is produced. As stated before, the large availability of  $CH_3$  is such to make it to recombine in  $C_2H_6$ , as can be noticed by the yellow trace in Figure 39 (a). Indeed, all the intermediate species cited in M2 mechanism are found in the pre-chamber. Despite the availability of active radicals of the  $H_2 - O_2$  system, the  $CO$  oxidation is not reached in this stage, probably due to the high temperature and high equivalence ratio. Actually, the peak concentration of  $CO$  is achieved near the TDC.

**Flame propagation (-15 CAD ATDC)**



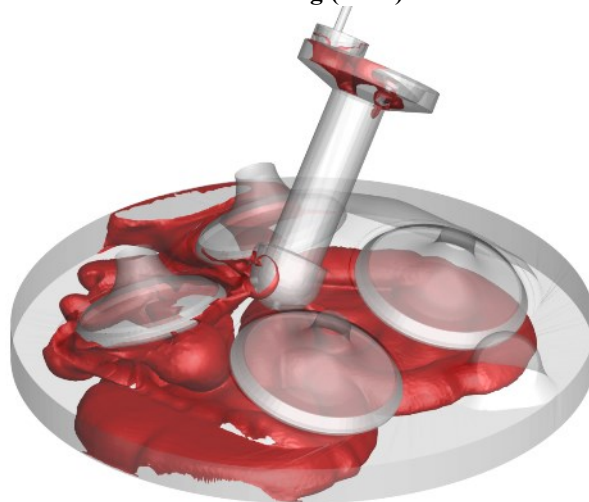
(a)

**Ejection (-7 CAD ATDC)**



(b)

**Reburning (TDC)**



(c)

*Figure 38 -  $G=0$  iso-surfaces, indicating the turbulent flame front propagation, colored with temperature*

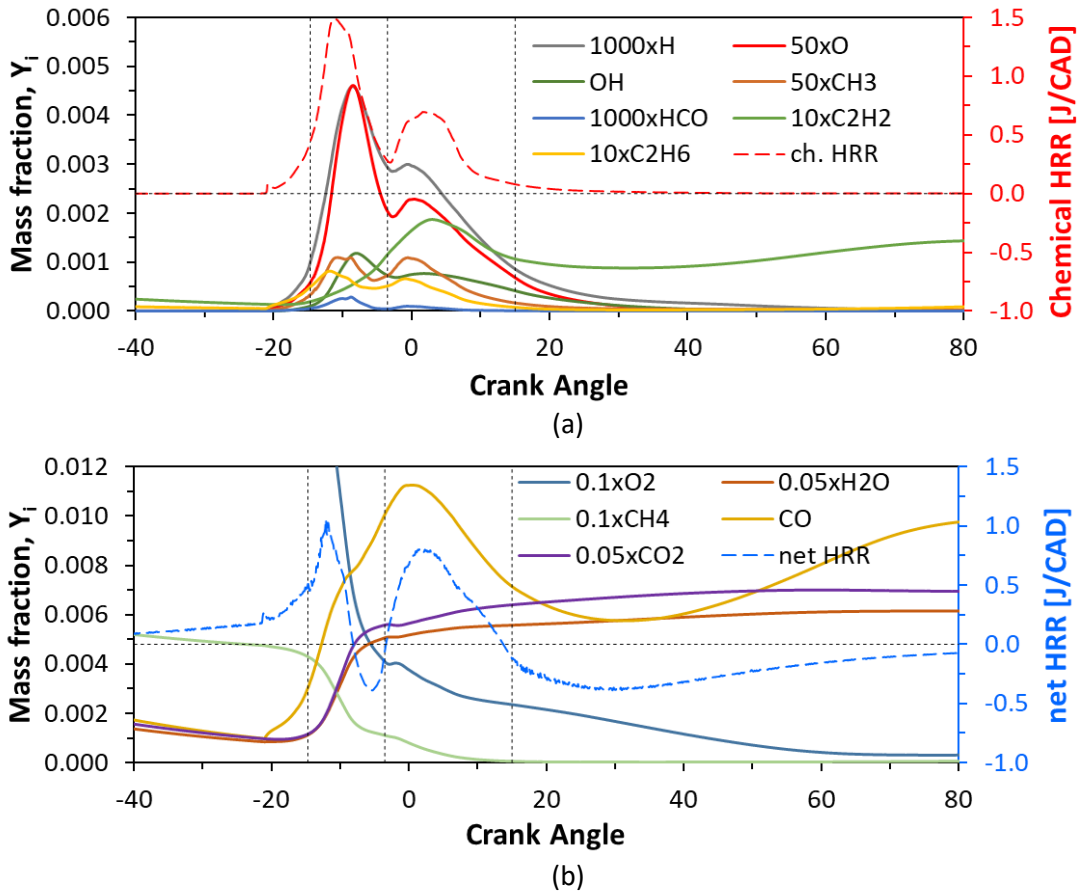


Figure 39 - Species mass fractions and HRR in the pre-chamber. (a) radicals and chemical HRR, (b) main product and net HRR. Dashed, the flow reversal events

The peak concentration of active radicals ( $O, H, OH, CH_3$ ) is, instead, reached at around -7 CAD, at the end of the propagation phase – i.e., when the flame has reached its maximum extension and the pressure is maximum. A sudden reduction of the radical concentration is observed soon after, when the flame impacts against the orifices. It is worth noting that after the peak,  $CH_3$  concentration remains approximately constant for a brief period, indicating that  $CH_3$  is being produced and consumed (and ejected) at the same velocity. Despite the high speed kinetic reported in Figure 39, the flame-front developing in the pre-chamber seems to not propagate uniformly. As reported in Figure 40, the propagation speed is higher in zones characterized by an equivalence ratio closer to the stoichiometric value: the magenta line, the farthest from the spark-plug, is the first at being reached by the flame. In the meantime, a richer mixture is descending from the annular zone. Near the end of the propagation stage, at around -10 CAD, there is a small portion of the cylindrical region that has not burned yet. Such a region is characterized by higher values of the equivalence ratio. The volume enclosing this region will burn later, in the reburning stage.

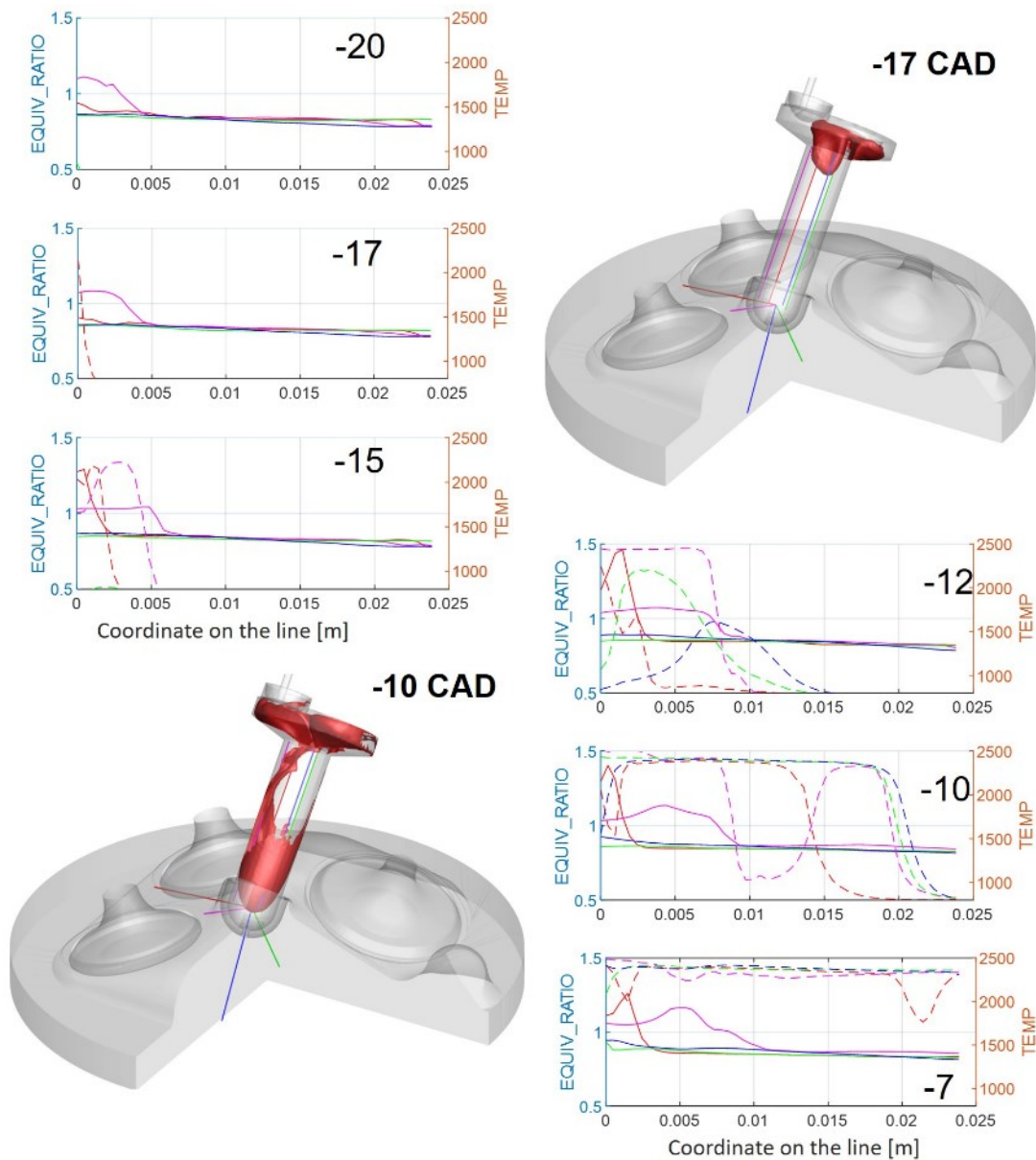


Figure 40 - Flame propagation in the pre-chamber; left axis, Equivalence Ratio (solid line); right axis, Temperature [K]. Flame visualization: iso-surfaces of  $G=0$

During the ejection phase, the reacting material generated in the pre-chamber is continuously transferred into the cylinder (cf.  $OH$  and  $CH_3$  traces in Figure 29), so that the main combustion event begins, as can be inferred from the net HRR and chemical increase recorded in the cylinder, shown in Figure 27 (solid blue line) and in Figure 30. The material being ejected from the pre-chamber, fresh mixture,  $CO_2$  and radicals, in this order -cf. Figure 29, reaches the main chamber at high temperature and with a high speed. The high velocity of the jets promotes the mixing between the hot and reacting material released by the pre-chamber and the fresh lean charge laying in the main chamber. A visualization of such effect is purposed in Figure 41.

Always considering Figure 41, the  $CO_2$  distribution between the orifices is not uniform. Such behavior can be inferred to the before mentioned non-uniformity in the flame propagation process, as well as, to a not homogeneous scavenging and successive mixing.

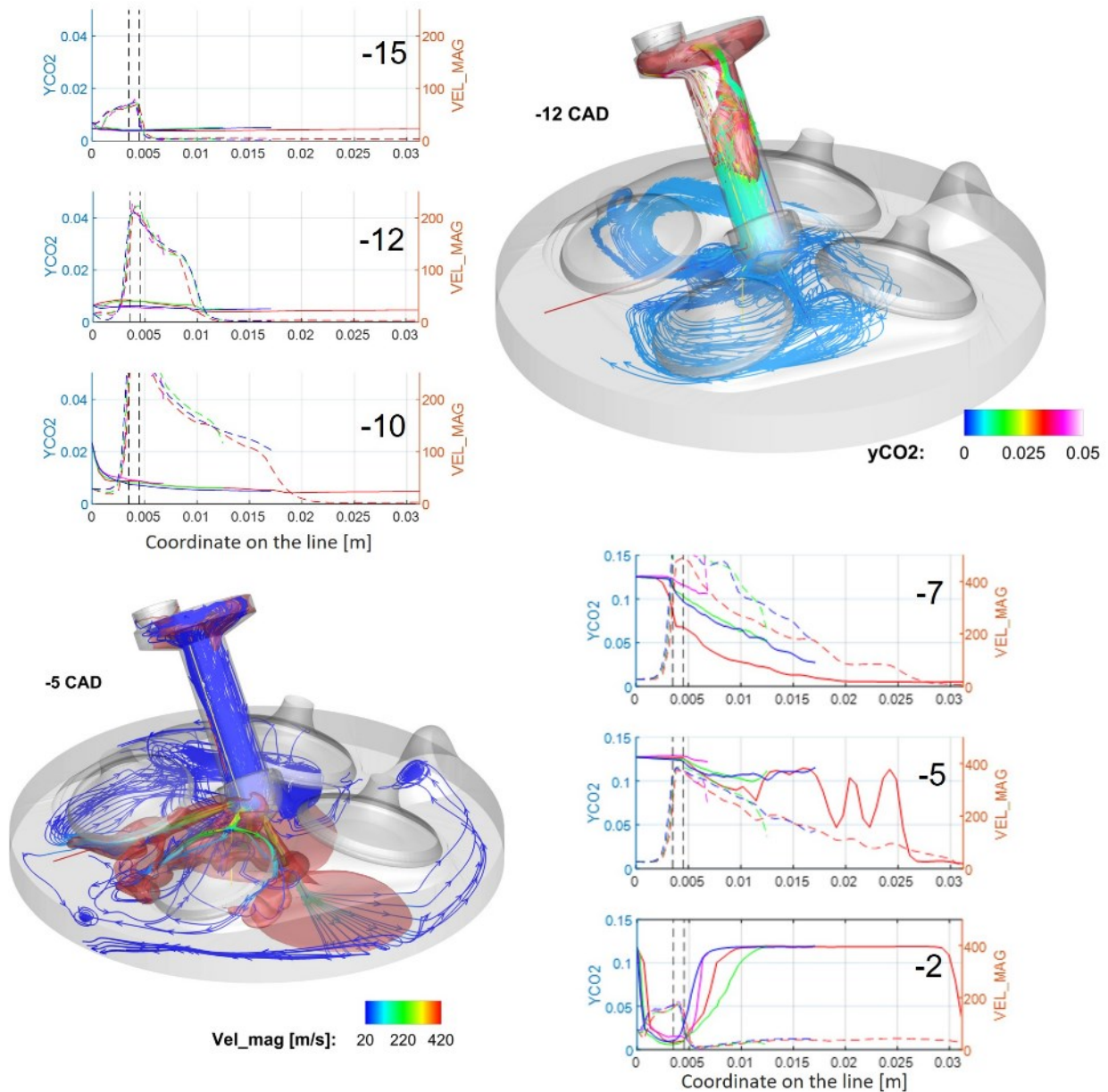


Figure 41 – Velocity magnitude [m/s] (dashed) and  $Y_{CO_2}$  distribution along the orifices' axes- black dotted, the orifices; Flame visualization, iso-surface of  $G=0$ . Stream-traces colored with  $Y_{CO_2}$  and Velocity magnitude

The jet penetration can be evaluated from Figure 41, on the red line (the longest) between -7 and -5 CAD, among the pressure peak in the pre-chamber. A penetration of about 20mm is found. For comparison purpose, the cylinder radius is 36mm.

A visualization of the flame at the early ejection time is purposed in Figure 42. Considering the temperature distribution reported in the same figure, the red line appears to be colder than the others. This, again, can be inferred to the non-uniformity of the flame-front reported in Figure 40.

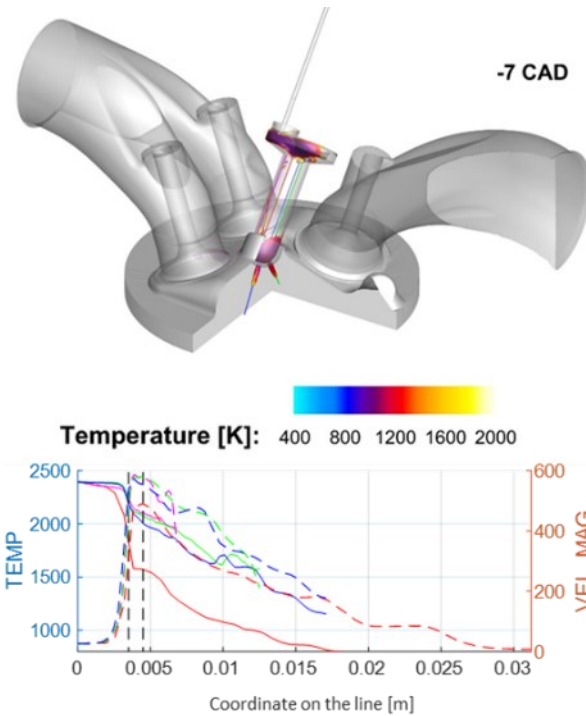


Figure 42 - Early ejection time; top, flame visualization by a  $G=0$  iso-surface colored with temperature. At the bottom, Temperature [K] (solid) and velocity magnitude [m/s] along the lines passing through the orifices.

In order to provide a deeper investigation about what happens when the flame reaches the orifices, the Damkohler number (defined as in Equation (16)) evolution among the orifices was evaluated. According to its definition, low values are typical of highly turbulent flows, where eddy turnover times are particularly low. Typical values in engine applications are in the order of dozens to hundreds [114], [115].

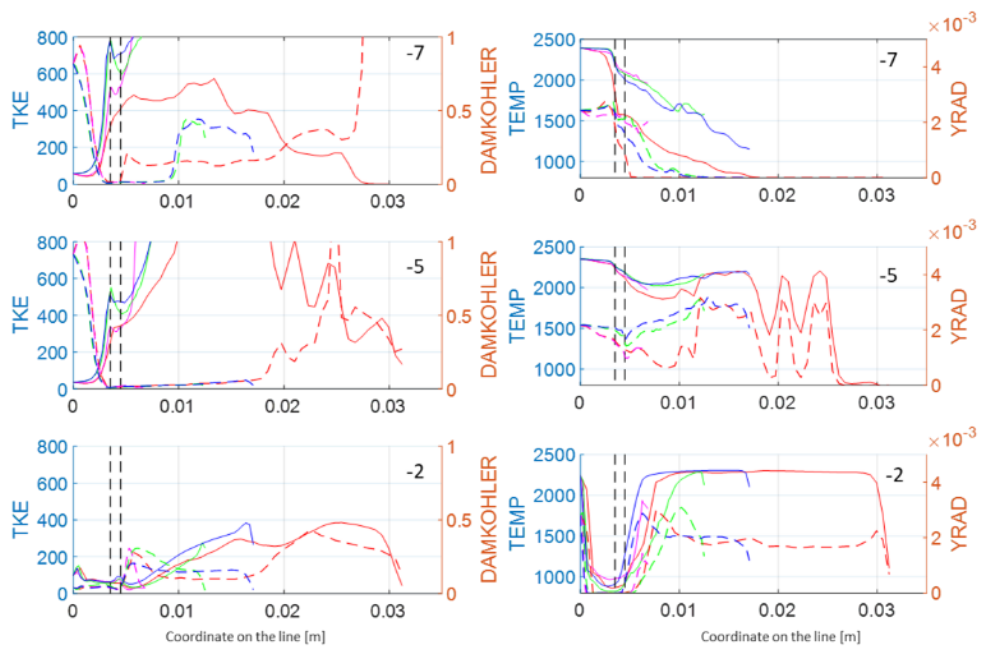


Figure 43 – Left axis, TKE (solid) and Damkohler number evolution; right axis, Temperature [K] (solid) and O,H and OH radicals mass fraction evolution.

The values reported in Figure 43 suggest that the reacting flow passing through the orifices can be considered as “frozen”, being the Damkohler number falling in the broken reaction region [92]. Values greater than 0.3 and lower than 0.6 can lead to ignition but a propagating flame is achieved only when the Damkohler number is greater than 0.6 [116]. Therefore, no ignition would occur around the pre-chamber until the turbulent mixing will slow down [65]. Indeed, the most of  $O$ ,  $H$  and  $OH$  radicals appear to be transported rather than produced and this also explains the plateaus of Figure 39.

The flame structure is also affected by the flow-field shear rate. Depending on its orientation regard the flame, the shear can either compress the flame-front (normal shear) or stretch it (tangential shear) [117]. By manipulating the eigen-decomposition of the strain rate tensor, it is possible to locally quantify the normal and tangential shear and the total dilatation [118]. Despite a large variability of data was observed in literature, the shear flame extinction limits depend on fuel, equivalence ratio, pressure, temperature and Reynolds number [119], [120].

In Figure 44 are reported the normal and tangential components of the shear rate and its magnitude from the flame development phase in the pre-chamber until the main combustion ignition. The normal and tangential components are barely distinguishable, indicating that the flow-field shear has no preferential directions. When the flame reaches the orifices, both components are positive, indicating that the flame is stretched in each direction. The strain-rate magnitude at the main charge ignition time is order of scales higher than those reported in literature for sustainable premixed flames [121]–[123]. The same applies for the components. Although a stable flame can-not be established, ignition can still occur [123]. After about -6 CAD the thermodynamic conditions are such to ensure a flame front propagation, as highlighted by the slope of the chemical HRR in Figure 30 or Figure 47 and by the flame volume calculations, discussed later, and summarized in Figure 65.

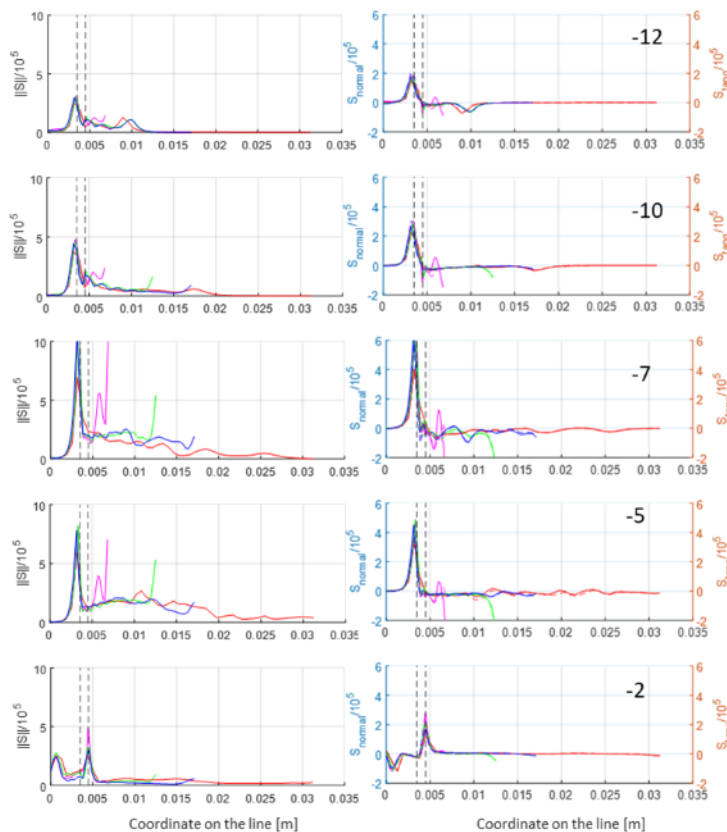


Figure 44- Shear rate magnitude, left; Normal and tangential shear rate evaluated on the lines crossing the orifices.

Another interesting perspective about the main charge ignition time is given by the analysis of the Takeno

Flame Index (TFI). It is defined as the normalized inner product of the fuel and oxidizer gradients [124]. The TFI ranges between -1 (prevalent diffusive) and +1 (prevalent pre-mixed) and characterizes the combustion mode [125].

As reported in Figure 45, at the main ignition time, there are two annular diffusive zones. They represent the effect of the hot jets impinging the piston. The next snapshots refer to the ongoing of a prevalent pre-mixed combustion where the sparse diffusive zones are located in the burned region (post-flame reactions).

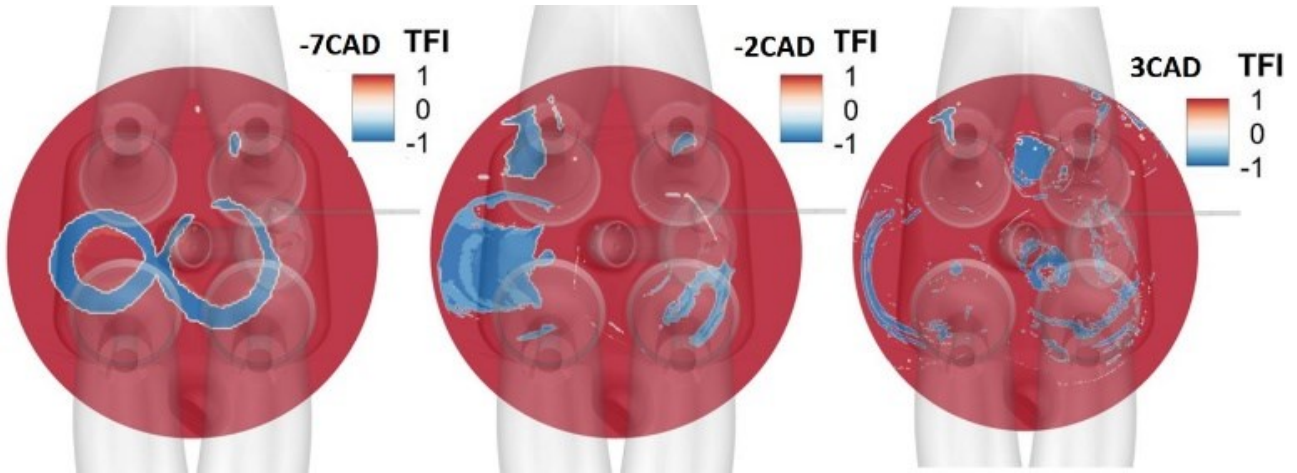


Figure 45- Takeno Flame Index distribution in the main chamber. The contour refers to a plane at middle height between the piston and the engine head.

Therefore, the combustion in the main chamber is initiated by a hot flow of reacting material. The intermediate species reported in Figure 44 before the ignition derives from the pre-chamber. When the ignition occurs, the fuel is rapidly oxidized, as confirmed by the chemical HRR trace in Figure 47. Methane is rapidly converted to  $CO$  and  $CO$  to  $CO_2$ , thanks to the presence of sufficient  $OH$  concentration and to more favorable thermal conditions. The combustion follows the M1 reaction path: Hydrogen is abstracted from Methane until the generation of  $CO$ , whose concentration appears to remain constant until the consumption of Methane. The average temperature evolution in both chambers is reported in Figure 46 and, as can be observed, the main chamber has a gentler temperature rise in the combustion phase.

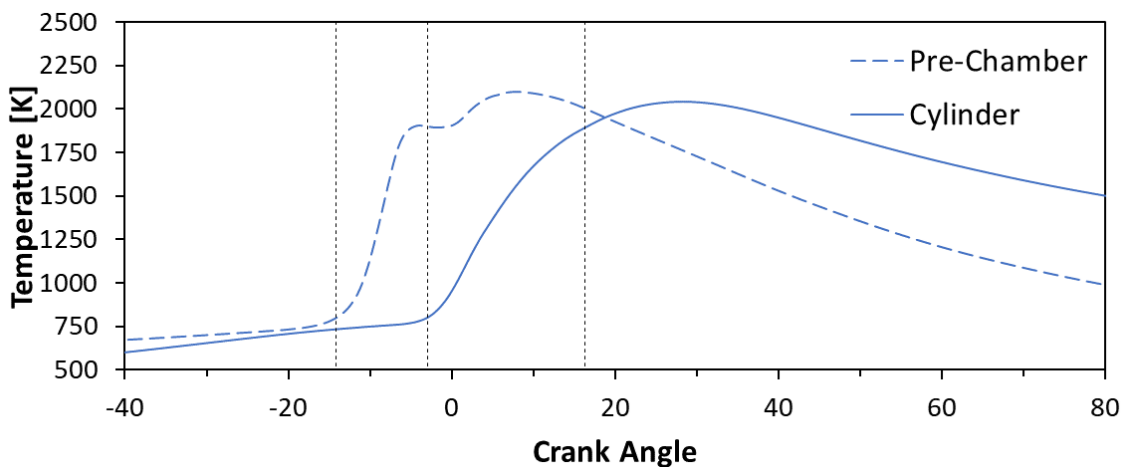


Figure 46 - Average temperature in the pre and main chamber

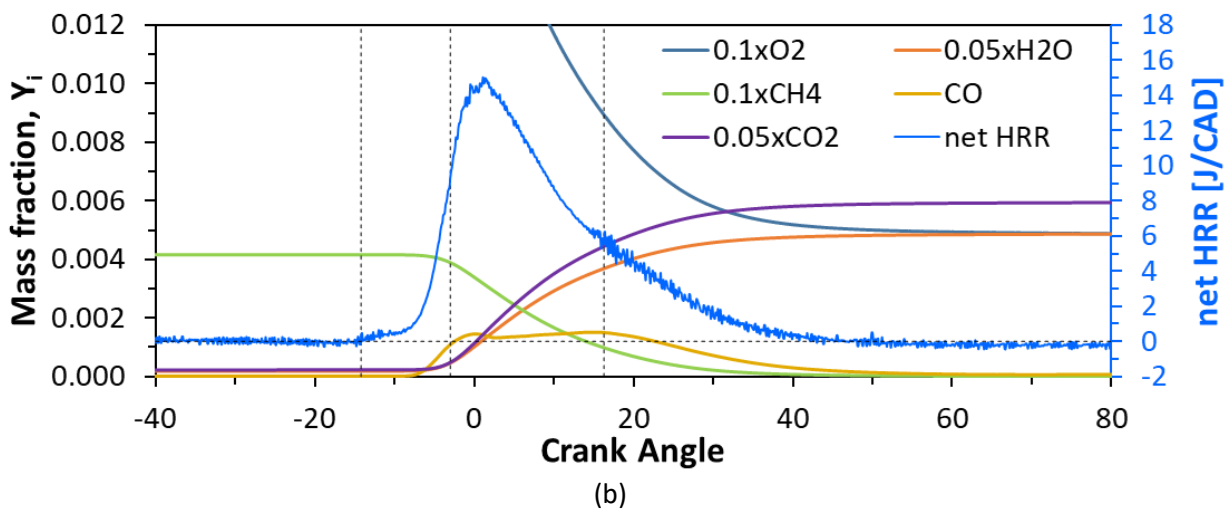
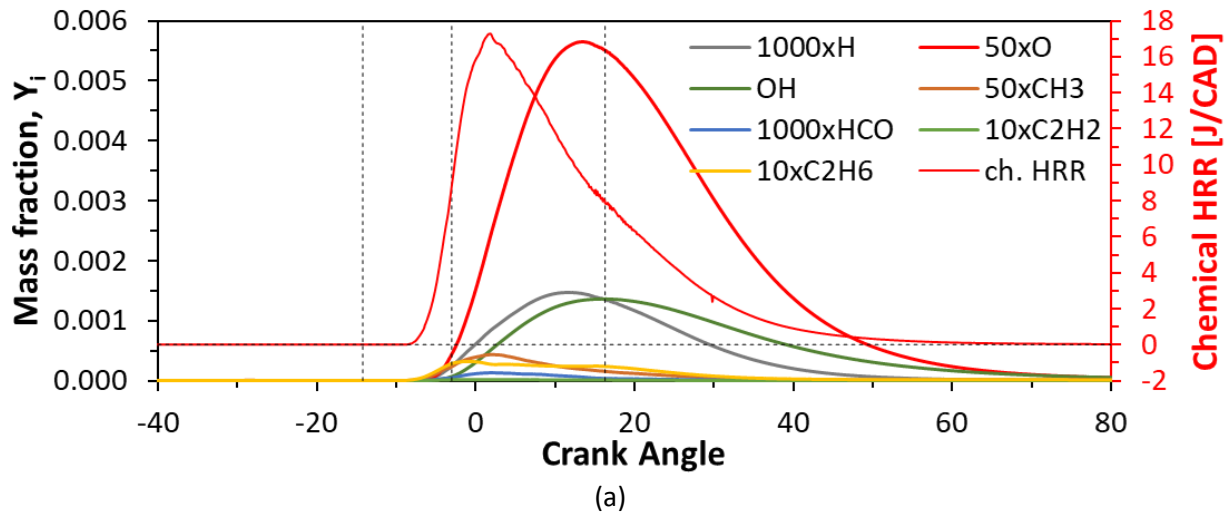


Figure 47 - Species mass fractions and HRR in the main chamber. (a) radicals and chemical HRR, (b) main product and net HRR. Dashed, the flow reversal events.

Figure 48 shows the situation at -2CAD. The stream-traces, colored according to the velocity magnitude, describe the mixing enhanced by the turbulent jets. The jets on the green, blue and red lines impinge against a boundary and generate ascending motions of the charge. Such motions are directed toward the center of the combustion chamber by the engine head. Globally, 3 vortices pushing the charge toward the center can be identified. Inside of the mushroom-shaped flames, the Damkohler number is globally lower than 0.5 and becomes higher approaching the flame front. Finally, in the annular portion of the pre-chamber, where the Damkohler number is greater than 1, there is still a small flame burning. It is worth noting that the zones, at -2 CAD, characterized by negative values of the TFI (cf. Figure 45) are also characterized by low Damkohler numbers.

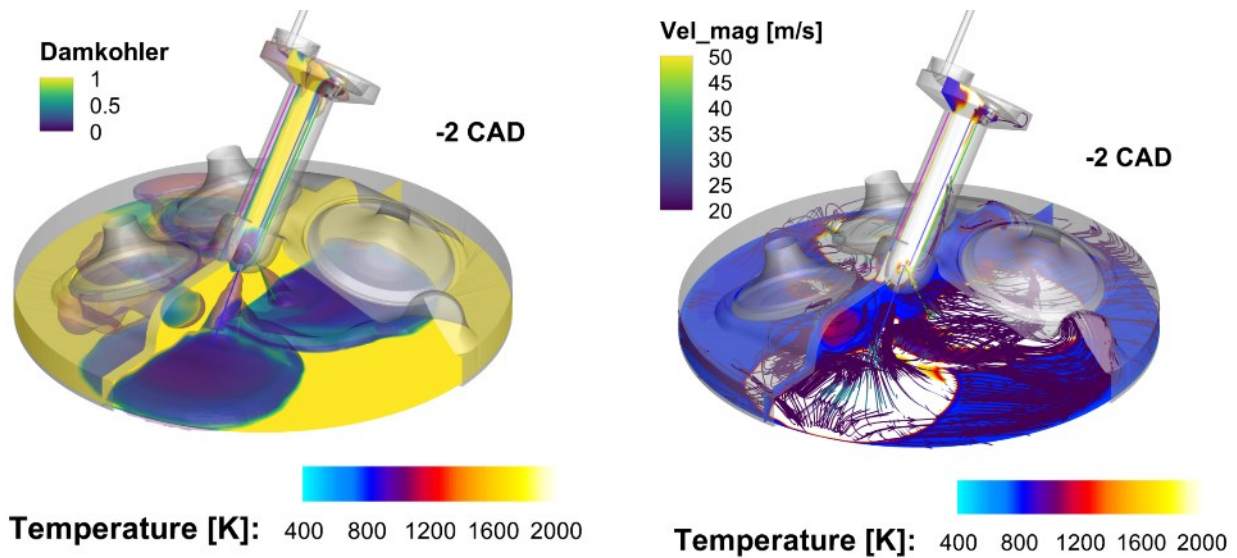


Figure 48 - Flow-field visualization at -2CAD. Streamtraces colored with the velocity magnitude; Iso-surface of  $G=0$  colored with temperature; left slices colored with Damkohler number; right slices with temperature contour.

When the pressure in the cylinder exceeds the value in the pre-chamber, a second flow inversion is induced at about -4 CAD ATDC and a flux carrying unreacted mixture and a lower share of hot reacting material, is established from the cylinder to the pre-chamber, as shown in Figure 29. The presence of unreacted Methane in this flow suggests that the ignition of the in-cylinder mixture does not occur in the proximity of the orifices but rather it takes place at a distance dependent upon the reacting jet momentum, and not uniformly among the orifices. The energy carried by this flow is represented by the green area in Figure 30 and amounts to - 7.2 J. A second combustion event in absence of proper flame propagation, that is the reburning phase (cf. Figure 38 (c)), is initiated in the pre-chamber because of this backflow, as can be inferred from the presence of a second peak in the net HRR trace in the pre-chamber (dashed blue line in Figure 27) and from the chemical HRR in Figure 30 or in Figure 39. As can be inferred by the species evolution reported in Figure 39, a new oxidation process is evolving. In the early stage of such process, radicals seem to be injected rather than produced. Figure 49 shows the evolution of the Methane mass fraction along the lines through the orifices and inside of the pre-chamber. As it appears, until the TDC Methane is flowing almost uniformly through the various orifices. At the same time, until -2 CAD ATDC – cf. the equivalence ratio in Figure 40 and Figure 50- the descending material in the pre-chamber stops. Also, the velocity distribution, not showed, is homogeneous until about 3 CAD ATDC. Then, the velocity along the red and green lines reduces to about a half. This promotes the generation of a convective motion inside of the pre-chamber which moves the reactive and lean charge to the top. Considering the equivalence ratio reported in Figure 50, one can observe the mixture becoming richer along the red and, more gently on the green line, between 3 and 8 CAD ATDC.

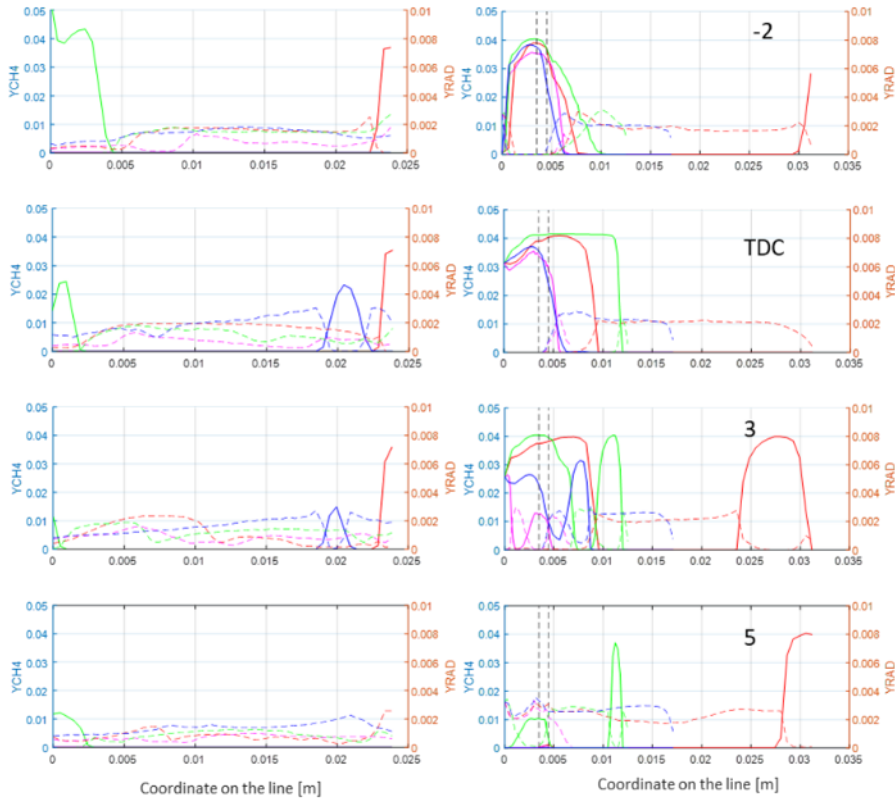


Figure 49-  $CH_4$  and  $O, H$  and  $OH$  radicals mass fractions evolution, left along the pre-chamber lines; right, along the orifices lines.

As anticipated, the main chamber also sources active radical in the pre-chamber. Referring to Figure 49 and Figure 29, both  $CH_3$  and  $O, H$  and  $OH$  radicals travel through the orifices. At the same time, Figure 50 shows that until -2 CAD ATDC the  $C_2$  compounds are descending the pre-chamber. In the meantime, other  $C_2$  compounds, generated during the ejection and remained un-oxidized, are arriving from the orifices.

As this secondary combustion goes on,  $C_2H_6$  is rapidly converted into  $C_2H_2$ , which shows its peak shortly after the second peak of the  $C_2H_6$  concentration- cf. Figure 39. The following decrease of the  $C_2H_2$  mass fractions is ascribable to its conversion to  $CH_2$  and, eventually, to  $CO$ . The  $CO$  concentration presents its highest value in correspondence to the second net HRR peak (Figure 39 (a)). The produced  $CO$  is relatively quickly oxidized to  $CO_2$  thanks to the availability of  $OH$  during the reburning phase. However, these active radicals are quickly depleted, so that their concentration soon falls to levels that result too low for completing the conversion of  $CO$  to  $CO_2$ , cf. Figure 51, as well as for promoting the oxidation of the other intermediate species, such as  $C_2H_2$ , as reported in Figure 50.

It is worth noting that the reburning stage takes place in absence of a propagating flame, as stated by the low Damkohler numbers reported in Figure 51.

Heat production is accompanied by a pressure rise. Consequently, a new expansion of the combusting gases within the pre-chamber takes place in this phase, and a third flow inversion is induced during the expansion stroke at about 16 CAD ATDC (cf. Figure 29). Mainly, fully oxidized products leave the pre-chamber and reach the cylinder in the final stages, during the expulsion & extraction phase. The energy released by the pre-chamber in this stage is represented by the gray area in Figure 30 and was quantified to be 11.4 J. As stated at the end of the Preliminary analysis section, Preliminary analysis, the overall energy balance is positive. By summing up the three contributions, a total energy release of 7.4 J is obtained.

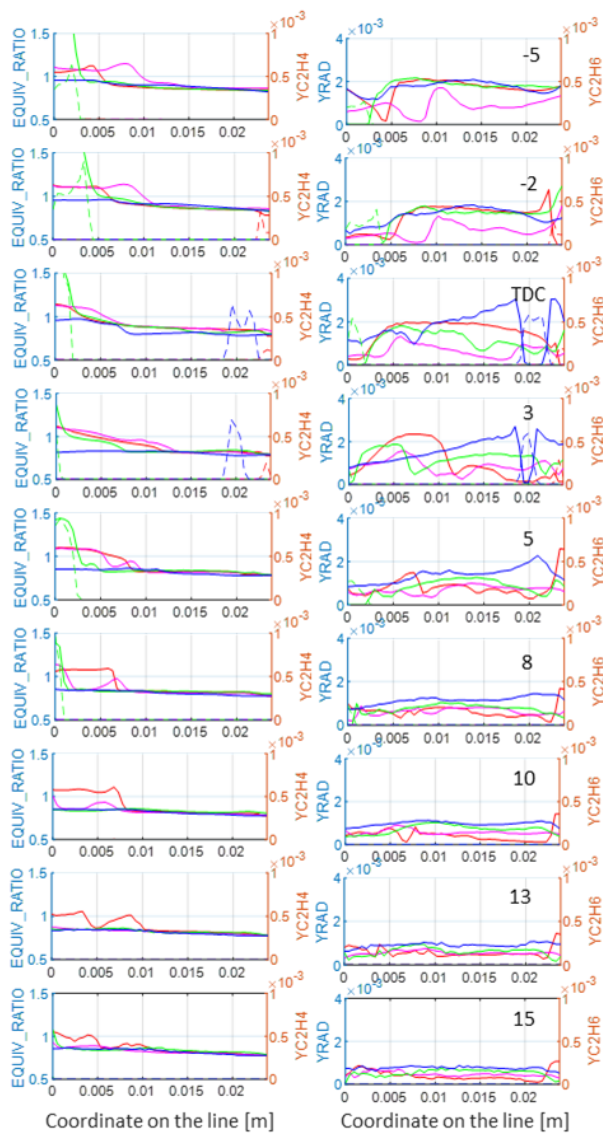


Figure 50- Left, Equivalence ratio and  $C_2H_4$  mass fraction distribution; Right,  $O$ ,  $H$  and  $OH$  and  $C_2H_6$  mass fractions distribution along the lines in the pre-chamber.

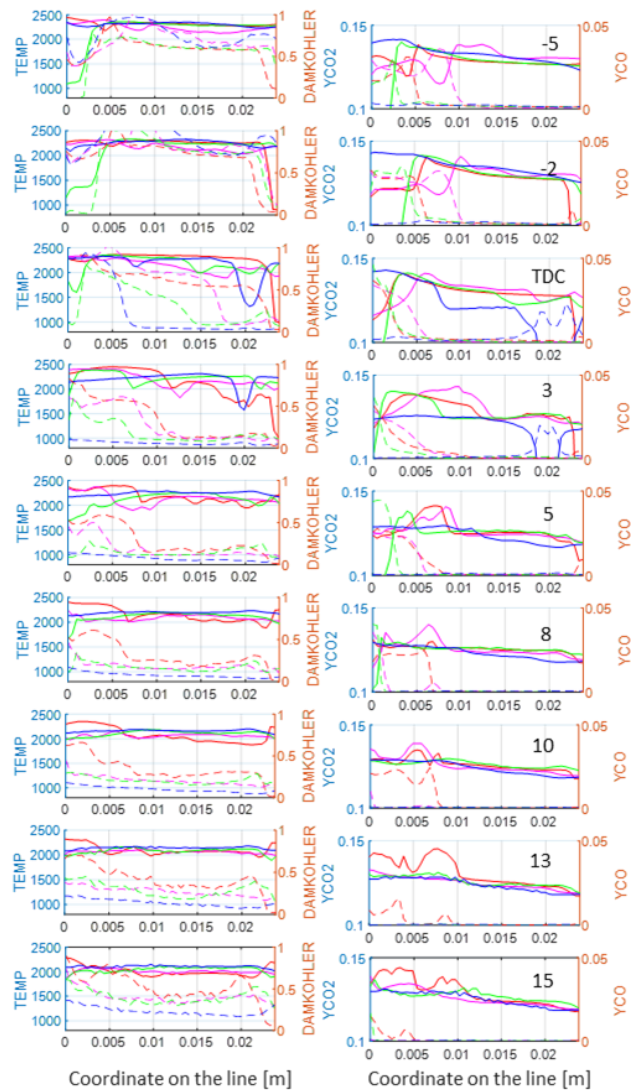


Figure 51- Left, Temperature [K] and Damkohler number distribution; Right,  $CO_2$  and  $CO$  mass fraction distribution along the lines in the pre-chamber.

### 5.2.5 The expulsion phase and pollutant production

During the expansion stroke, when the pressure in the main chamber becomes lower than the pressure in the pre-chamber, the expulsion phase occurs. In this stage the mean temperature, reported in Figure 46, in the pre-chamber decreases earlier than the main chamber.

In Figure 53 the un-burned HydroCarbons (HC) mass fractions along the lines in the pre-chamber and along the lines crossing the orifices is monitored.

By one hand, the reburning promotes the oxidation of the un-burned hydrocarbons being in the pre-chamber; by the other, new un-burned material (comprising fresh lean mixture) is pushed into the pre-chamber until about 8 CAD ATDC.

During the expulsion, the reacting radicals in the pre-chamber are consumed to oxidize the remaining HC to  $CO$  and  $CO$  to  $CO_2$ . However, as introduced in The filling and scavenging phases section, some residuals and

fresh charge remained trapped in the injector duct. They will be in part released in the expulsion stage. This can be noticed in Figure 54: there are HC descending the cylindrical part. Such material leaves, partially, the pre-chamber in the late expansion stroke, at about 70 CAD ATDC, as reported always in Figure 54. Nevertheless, their contribution to the global un-burned HC balance is negligible. Indeed, as reported in Figure 55, un-burned HC mass fraction in the main chamber keeps globally lower in respect to the pre-chamber one.

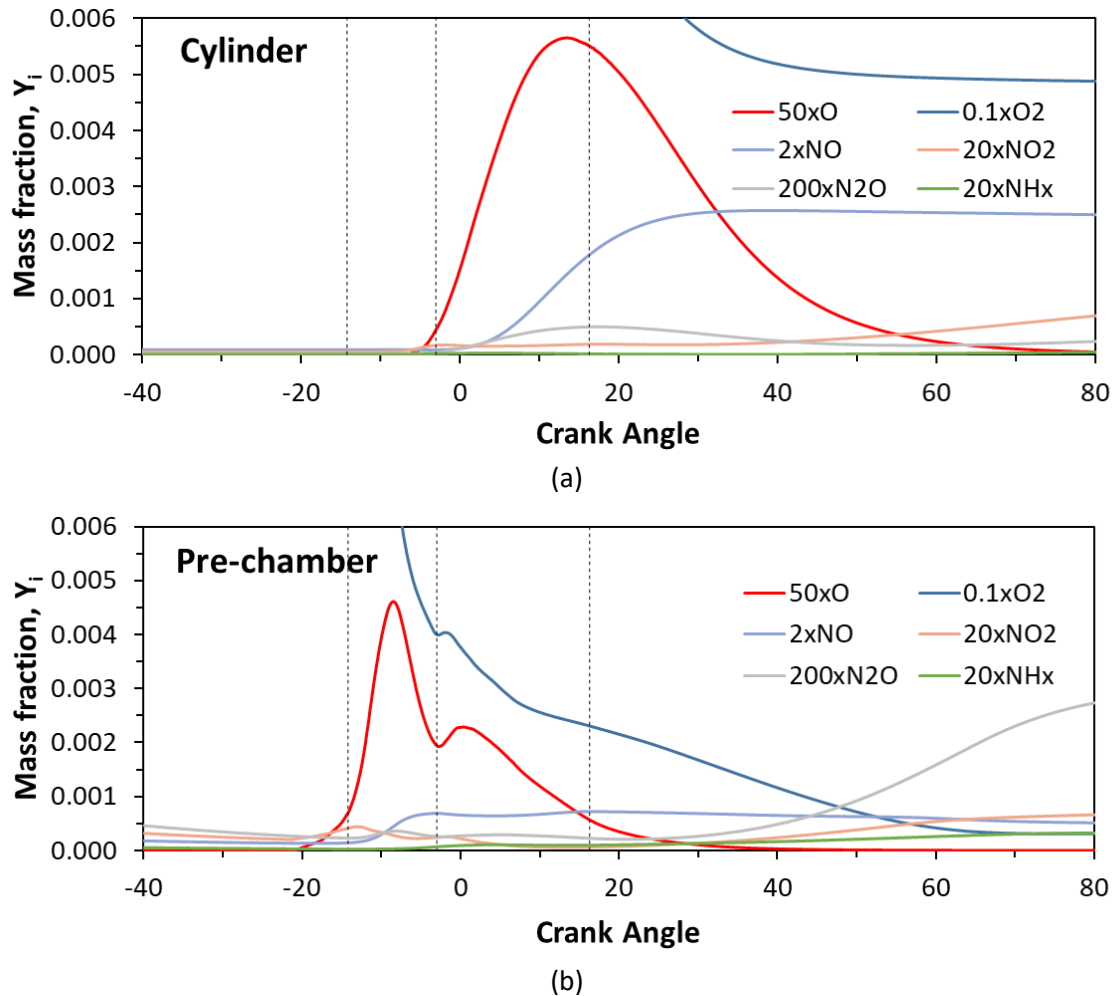


Figure 52. Nitrogen oxides mass fractions: (a) in the cylinder and (b) in the pre-chamber. Vertical dashed lines indicate flow reversal events.

Despite the average temperature of the pre-chamber overcomes the 2000K value for a brief period of time, the actual values in the cylindrical zone keep higher for a longer time (cf. Figure 51). In addition, the huge presence of  $OH$  radicals may enhance the  $NO$  production rate [26]. Therefore, it is of interest to analyze in detail the formation of nitrogen oxides because the lean conditions under which combustion evolves in the cylinder could promote their formation in relevant amounts. Figure 52 shows that both in the cylinder (a) and in the pre-chamber (b) the  $NO$  concentration increases until it reaches an equilibrium value, depending on the  $O$  radicals' availability and the thermal formation pathway. An increase in  $NO_2$  levels in the final stages is promoted by the availability of  $O$  radicals in sufficient concentrations. The presence of  $N_2O$  suggests that the ammonia pathway is active, as highlighted by the presence of  $NH_x$  compounds in non-negligible amounts, especially in the pre-chamber during the expansion stroke, as shown in Figure 52 (b), where richer

conditions reign. This factor, combined with favorable temperatures [126], promotes the recombination of some  $NO$  to  $N_2$ : methyl radicals (often produced in fuel rich conditions [91]) combines with  $NO$  triggering the ammonia pathway leading to  $NO$  reduction to  $N_2$  [127], [128]. The reaction pathway is summarized in Figure 56. A moderate  $NO$  reduction can be, indeed, noticed in Figure 53 and Figure 54. However, such phenomenon is limited to the pre-chamber only, making negligible its effect on the overall engine out emissions, in fact the ammonia levels in the main chamber are quite lower in respect with the ones detected in the pre-chamber, as reported in Figure 53 (a).

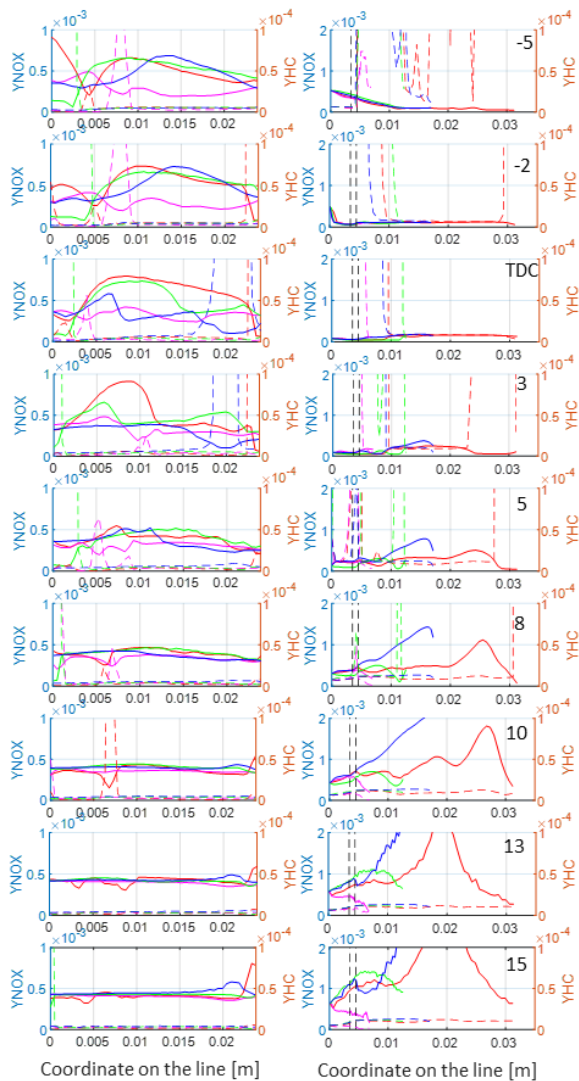


Figure 53-  $NO_x$ , left axis, and un-burned hydrocarbons (dashed), right axis, mass fractions; Left, along the pre-chamber lines; Right, along the lines crossing the orifices. Black dashed, the orifices

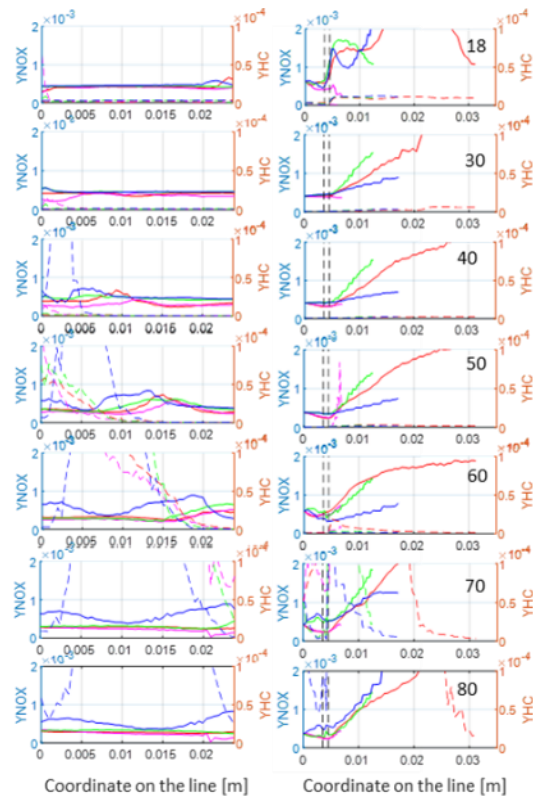


Figure 54-  $NO_x$ , left axis, and un-burned hydrocarbons (dashed), right axis, mass fractions; Left, along the pre-chamber lines; Right, along the lines crossing the orifices. Expulsion stage

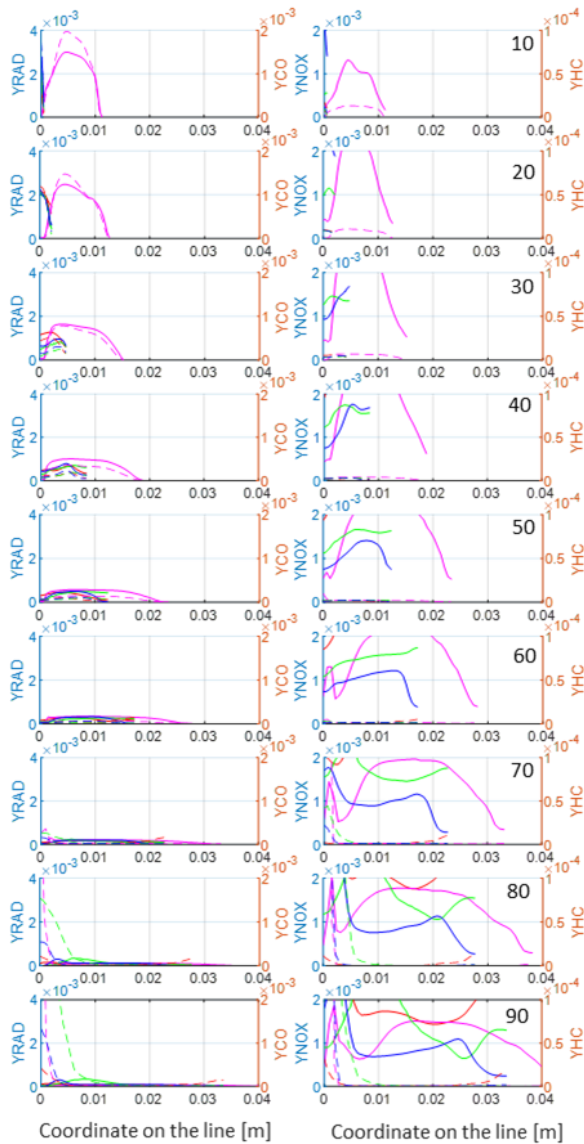


Figure 55- O,H and OH radicals and NOx mass fractions on the left axis, CO and HC mass fractions on the right axis along the cylinder lines

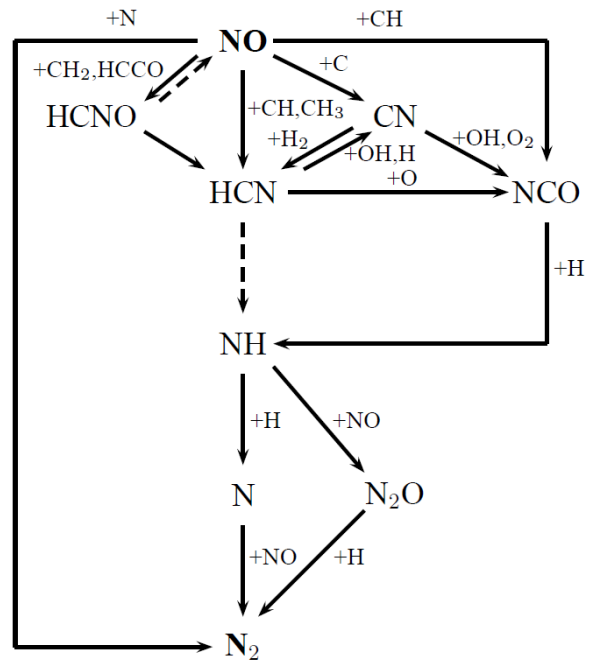


Figure 56 - Pathway of NO reduction by reburning with Methane [26]

It is worth noting that there is an appreciable quantity of O, H and OH radicals also in the main chamber in the late expansion stroke. This, together with the still high temperature, promotes the oxidation of C to CO and CO to CO<sub>2</sub>. However, such conditions have, as before mentioned, a negative impact on NO<sub>x</sub> production. The main pollutant mass fractions at the EVO are summarized in Table 7.

|                     | CO <sub>2</sub>        | CO                     | HC                     | NO <sub>x</sub>        |
|---------------------|------------------------|------------------------|------------------------|------------------------|
| <b>Pre-chamber</b>  | 1.2 × 10 <sup>-1</sup> | 9.9 × 10 <sup>-3</sup> | 1.3 × 10 <sup>-3</sup> | 2.9 × 10 <sup>-4</sup> |
| <b>Main chamber</b> | 1.4 × 10 <sup>-1</sup> | 9.4 × 10 <sup>-5</sup> | 6.2 × 10 <sup>-5</sup> | 1.3 × 10 <sup>-3</sup> |

Table 7- Main pollutant mass fractions at EVO.

### 5.2.6 Compressibility effects

In Figure 41, it can be observed that the velocity peak values evaluated in the ejection stage are in the order

of 600 m/s. Such high velocities may involve compressibility effects and, potentially, lead to choking conditions.

Figure 57 reports the Mach number and the density gradient at -7 CAD ATDC (maximum velocity) and at -2 CAD (soon after the beginning of the reburning). As can be observed, the maximum Mach number near the orifices is lower than one. Thus, choking is avoided for the considered geometry and operating conditions. However, compressibility effects due to the flow-field are noticeable both in the reacting jets at -7 CAD and in the entering jets at -2 CAD.

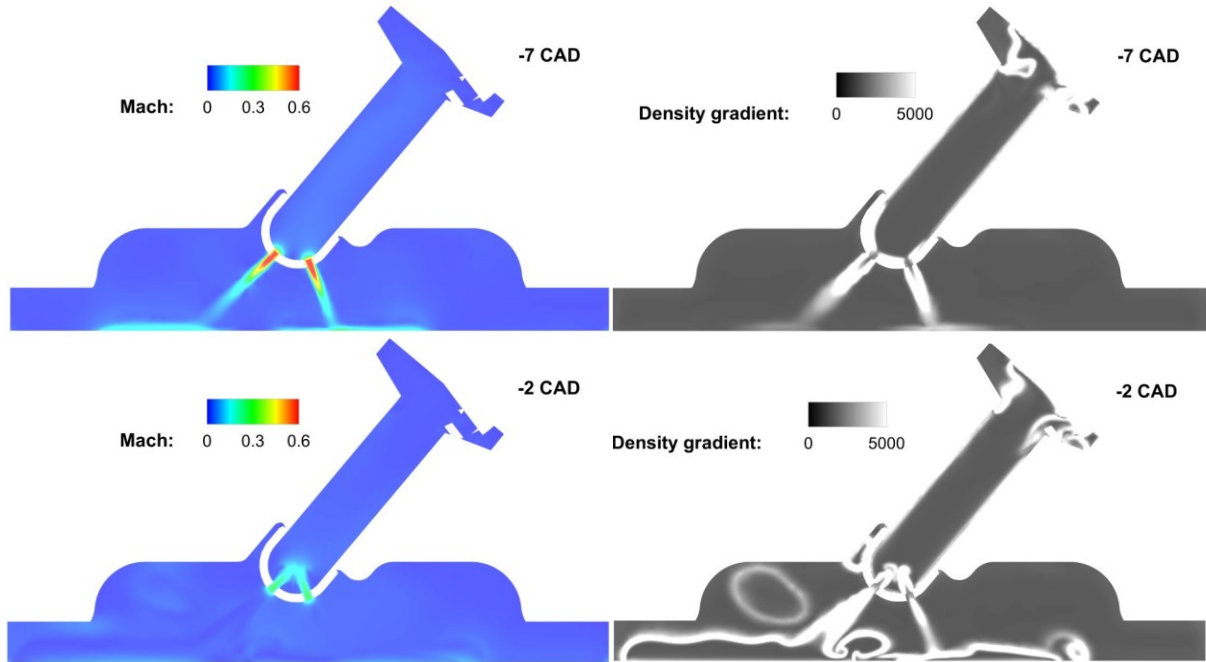


Figure 57- Mach number and density gradient distribution.

### 5.3 Engine out emissions

After having discussed the distribution and the production mechanism of the main engine pollutant emission, a comparison of the modeled pre-chamber engine with the modeled standard engine is performed.

Emissions were evaluated by considering the mass of the species of interest, as  $\text{CO}_2$  for example, which left the domain during the scavenging process, that is, from EVO to EVC, either by the exhaust or the intake duct. In this way, the species that reached the intake duct in the previous cycle will be computed in the actual cycle emission evaluation. The remaining (from EVC to IVC) in the intake duct will be inspired by the engine. A comparison among the computed values, scaled with the engine work, is purposed in Figure 58 and, as can be noticed, the pre-chamber engine behaves globally better.

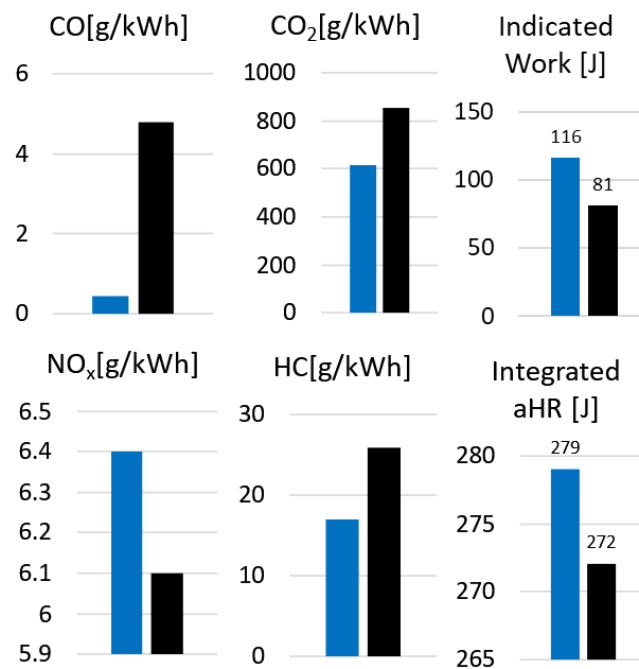


Figure 58- Computed engine out emissions; Blue, pre-chamber engine.

The raw values of  $CO_2$ , not reported, were comparable. Also, both the indicated work and the integrated apparent heat release are higher. This highlights a more efficient fuel conversion mechanism for the pre-chamber engine, recalling that the fuel-to-air equivalence ratio was 1.3 for both engines.

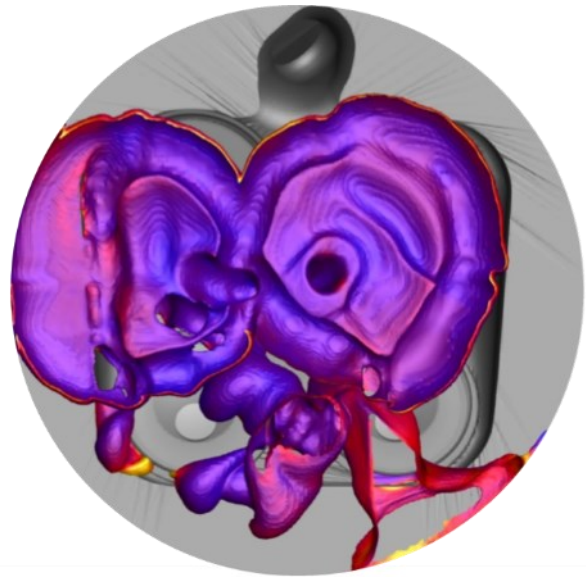
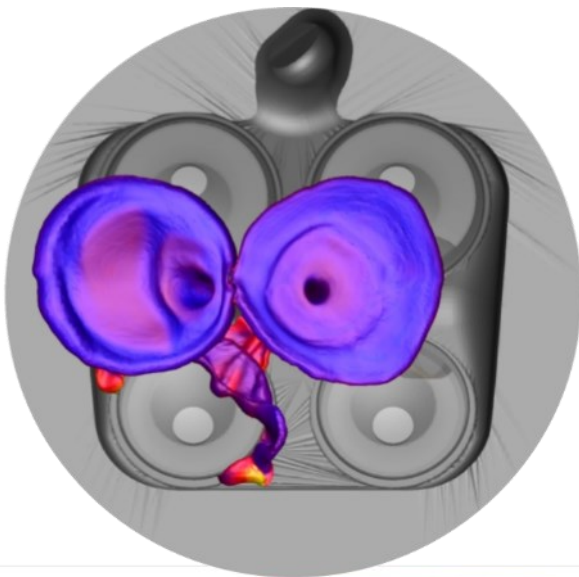
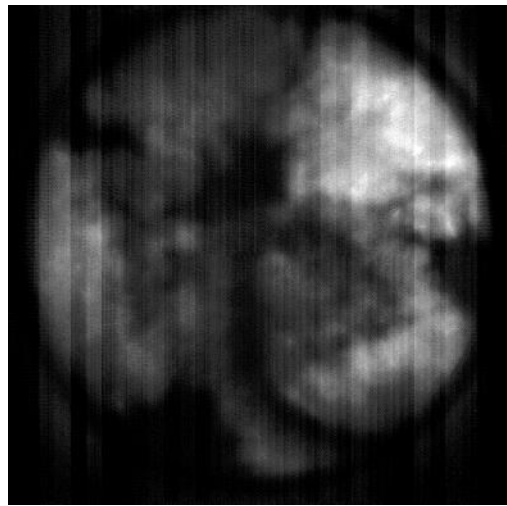
The low dilution is also the main reason for the higher  $NO_x$ . The mean temperature was still too high to inhibit the thermal  $NO_x$  path;  $\lambda > 1.4-1.6$  are necessary to obtain appreciable  $NO_x$  reductions [54], [62].

The lean condition contributes to the reduction of both the CO and the HC values. Moreover, the pre-chamber design, characterized by a big volume and narrow orifices, helps to control the release of un-burned material from the pre-chamber itself [63], [64]. Indeed, about the 15% of the material of the pre-chamber leaves it during the main chamber scavenging. Moreover, as already mentioned, the contribution of the pre-chamber mass to the global balance has a minimum impact.

## 5.4 Flame shape and radius evaluation

Figure 59 to Figure 62 show a comparison between numerical and experimental images of the flame evolution in the main chamber at -5, 0, 3 and 5 CAD, respectively. The experimental data are obtained by an optical system, whereas the numerical results show the iso-surface of  $G=0$  (that is, the actual position of the flame front) colored with the temperature. There is a qualitative agreement in the position of the flame front with respect to the wall of the main chamber for each couple of corresponding frames. The flame visualization at -5 and 0 CAD (Figure 59 and Figure 60) shows that one of the jets impinges against the seat of one of the exhaust valves. Such phenomena, quite undesired, may be related to the design and the orientation of the orifices or to a misorientation of the whole pre-chamber. Of course, it should be avoided to preserve the overall engine reliability. Moreover, the image captured at 3 and 5 CAD shows that the bottom-left portion of the main chamber does not contain a wide flame. Also in the experimental images that portion of the domain appears darker than the rest of the main chamber, indicating a poor flame persistence. By the other hand, the numerical results at 0 and 5 CAD show that the jet issuing from the pre-chamber is characterized by strong chemical activity. Three regions can be identified in the mushroom-type structure generated by the mixture injection. In the first region, close to the orifice exit, a highly turbulent

flow is found where the temperature is very high (about 2200 K, cf. Figure 43) and the reaction is in its first stage, being characterized by a high concentration of  $H_2 - O_2$  radicals (cf. Figure 49). In the second region, an extended region of combustion is observed with lower values of temperature (about 2000 K) where the reaction is shifted towards the products. Finally, a third thin region is observed with a very strong temperature gradient (cf. Figure 60), which has the characteristics of a flamelet wrapping the turbulent combusting region.

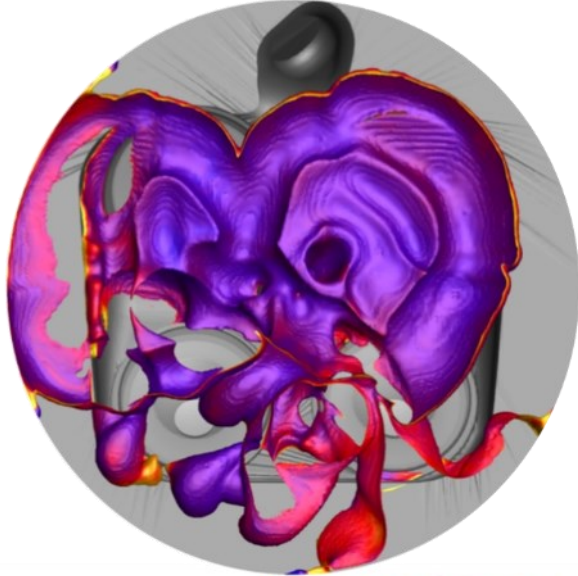
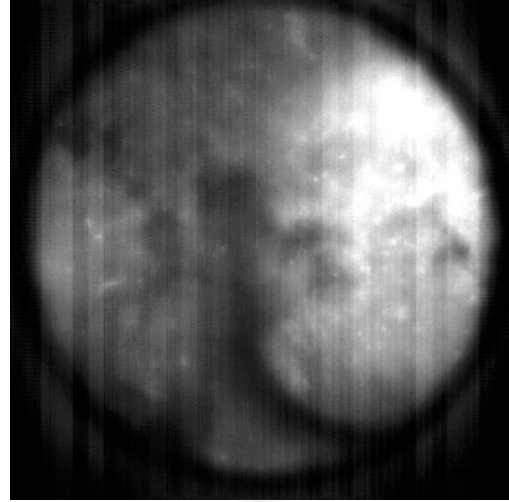
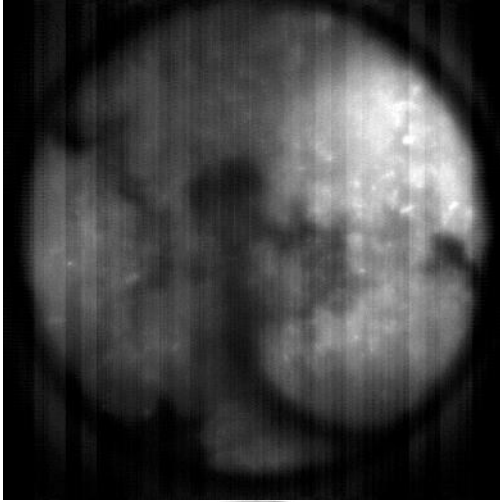


Temperature [K]: 400 800 1200 1600 2000

Temperature [K]: 400 800 1200 1600 2000

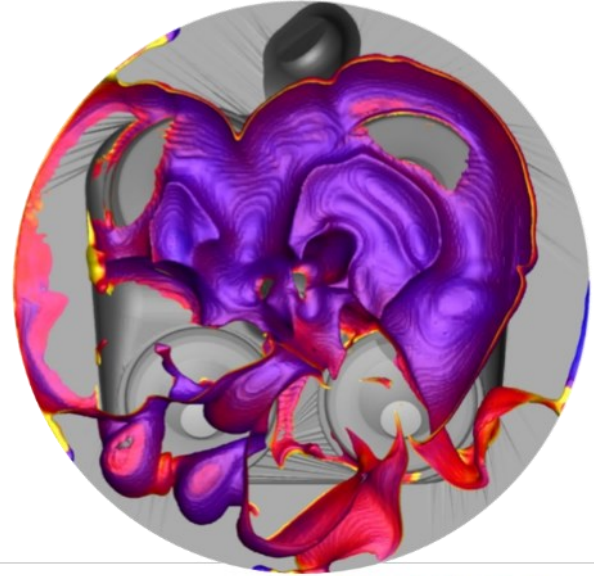
Figure 59-Experimental and numerical flame visualization at -5 CAD.

Figure 60-Experimental and numerical flame visualization at 0 CAD.



**Temperature [K]:** 400 800 1200 1600 2000

*Figure 61 - Experimental and numerical flame visualization at 3 CAD.*



**Temperature [K]:** 400 800 1200 1600 2000

*Figure 62-Experimental and numerical flame visualization at 5 CAD.*

As a conventional practice, the radius of a spherical propagating flame is measured in optically accessible engines by averaging the distance between the spark and the boundary of the flame, as schematized in Figure 63. Such measurement evaluated over the time is proportional to the flame speed and, consequently, to the burn rate.

Despite an analogous discussion can be performed for the pre-chamber engine, such approach may not consider the actual dimension of the flames. Indeed, by comparing the numerical flame radii (computed as in the experiments) with the mass burnt fractions, reported in Figure 64, one can observe that the actual burnt mass appears to be in late with respect to the flame, especially for the pre-chamber engine. Moreover, the shape of the plot of the flame radius for the pre-chamber engine is quite un-usual.

This is due to a lack of information about the actual shape of the flame (cf. Figure 59-Figure 62). As an alternative, one may consider the flame volume in order to compare the actual flame velocity. Such volume represents the volume of the domain with  $G$  less than or equal to 0, that is, the actual burned zone or the flame front.

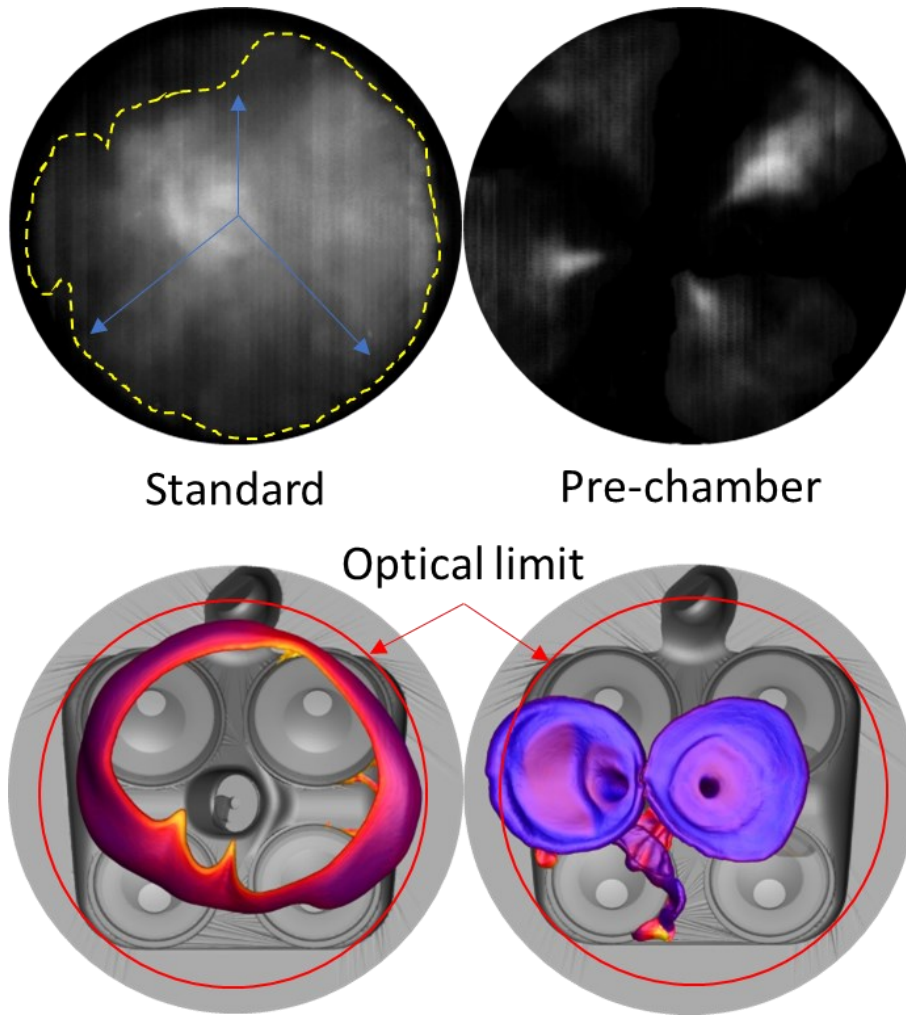


Figure 63- Experimental and numerical flame visualization and radius evaluation.

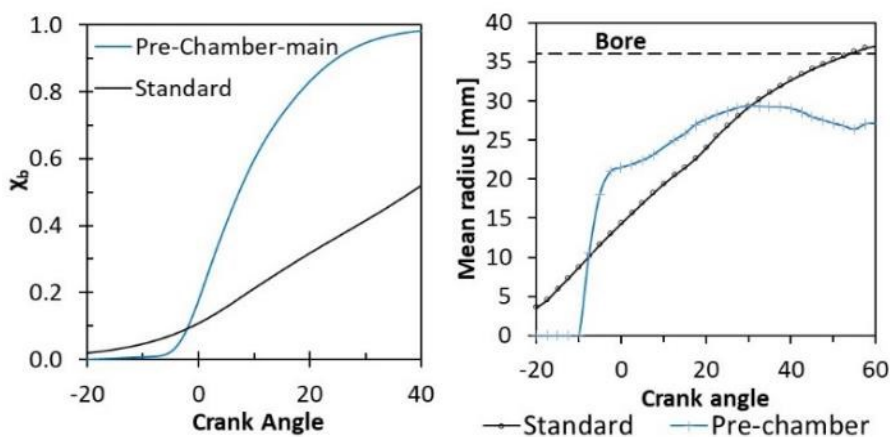


Figure 64- Left, mass burnt fractions in the main chamber of the pre-chamber engine and of the standard engine; Right, flame radii of the modeled engines.

By dividing it with the actual volume of the combustion chamber, one obtains an instantaneous measurement on the extension of the burned zone in the main chamber. The results are presented in Figure 65.

As could be expected, the trace obtained for the standard engine is in accord with the measurement of the

flame radius. A better agreement with the actual mass burnt fraction is also achieved for both engines. The flame growth behavior of the pre-chamber engine in the cylinder is also well captured. It is worth noting that at the ignition time, when the mass burnt fraction becomes greater than zero, the flame to cylinder volume ratio is nearly zero. This is due to the ignition mechanism: no flame is developing in the early stages of ignition. Also, the slope changes of the mass burnt fraction reflects in the volumes ratio. These observations should make one to reconsider the evaluation of the combustion speed when particular ignition systems, like TJI, are employed. Considering the difficulties to obtain the flame volume by experimental investigation in a real engine, the numerical approach seems to be the most reliable alternative in order to compare the flame growth and the combustion speed between different engine configurations.

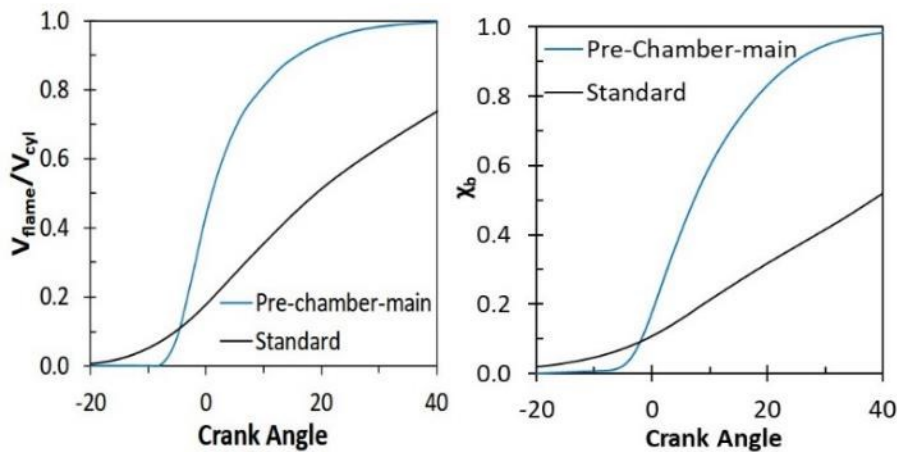


Figure 65- Left, a-dimensional flame volume in the main chamber of the pre-chamber engine and of the standard engine; Right, mass burnt fractions in the main chamber of the pre-chamber engine and of the standard engine.

|             | CA10 | CA50 | CA90 |
|-------------|------|------|------|
| Standard    | -9.4 | 38   | 78.1 |
| Pre-chamber | -2.6 | 6.7  | 24.4 |

Table 8- Combustion progress times

Finally, the combustion duration can also be easily evaluated, and the results are summarized in Table 8. It is worth noting that the CAD corresponding to the 10% burnt fraction is located about 4 CAD after the ejection, that is, about 20 CAD ASOS, against the almost 14CAD ASOS of the standard engine. Nevertheless, as anticipated by Figure 65, the combustion in the pre-chamber engine is completed in about one half of the time with respect to the standard engine.

## 5.5 Future work outlook

The results here presented are referred to an optically accessible research engine. The experimental campaign was both aimed at as assessing the retro-fitting capability of a TJI system and to evaluate its effects on combustion, in terms of combustion speed and flame development.

The next step of the experimental campaign regards the installation of the same prototype on the so-called *metal* engine. Such engine has the same specifications of the optical one, except for the quartz cylinder and the windowed piston, which is replaced with a GDI-type shaped piston. Unfortunately, also due to the COVID situation, the experimental campaign was delayed and, up to now, only preliminar results, achieved with

Gasoline in place of Methane, are available. Such results were gathered at 2000RPM, in WOT and stoichiometric conditions. By the side of the author, the matching of the metal engine, with the domain purposed in Figure 68, fueled with Gasoline was performed.

The kernel model purposed by Dahms et al. [129] was employed to better describe the initial flame kernel growth and transition toward a turbulent flame. Such model deposits the spark energy into an arbitrary number of parcels (1000 in the present computations) sourced, at spark time, between the spark electrodes. The parcels are advected and, at each timestep, the local Karlovitz (Ka) number is evaluated:

$$Ka = \left( \frac{\eta}{s_l^*} \right)^2$$

Where  $\eta$  is the Kolmogorov length scale and  $s_l^*$  is the sum of the local laminar flame-speed and the plasma speed. When the Karlovitz number falls below a specified critical value, the parcels are flag as “burning”. In this state, their dimension is set to 0.5mm and they are allowed to coalesce. When the dimension of a cluster of particles reaches the grid dimension, the cells containing that parcel are flag as burning by setting G=0 in that cells.

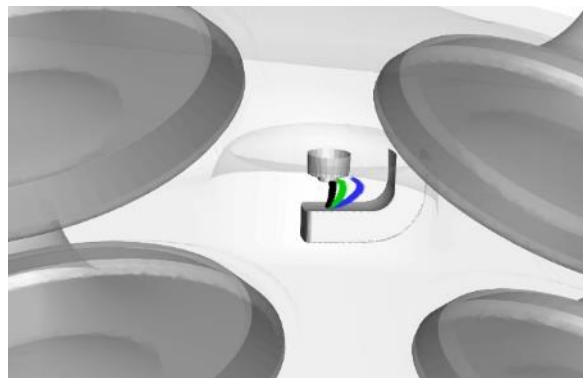
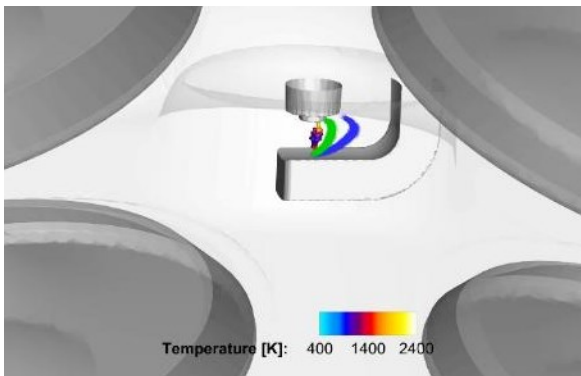
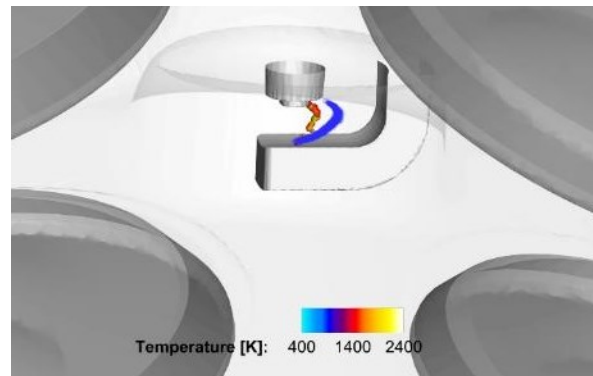


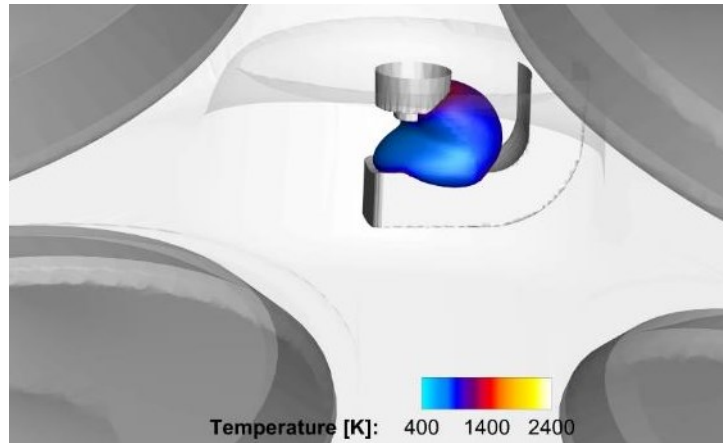
Figure 66 - The kernel particles: Black, 1.5 CAD after SOS; Green, 4.5 CAD after SOS; Blue, 10 CAD after SOS.



(a)



(b)



(c)

Figure 67 - The kernel evolution. (a), 1.5 CAD after SOS; (b) 4.5 CAD after SOS; (c) 10CAD after SOS. The flame is visualized as a  $G=0$  iso-surface colored with temperature

Figure 66 and Figure 67 shows the kernel particles position and the flame kernel development, respectively. The model setup differs, apart of the kernel model, from the ones described in Section 4 for the absence of the crevice model. Of course, also the laminar flame-speed correlation was modified by including the proper coefficient for Gasoline simulations. Gasoline was modeled as a binary mixture of Iso-octane (60.1% vol) and Toluene. Such blend was selected in order to match the LHV and H/C values of a commercial Gasoline. The fuel oxidation was described by the mechanism purposed by Andrae et al. [130], consisting of 123 species and 583 reactions. The model tuning procedure was the same described in Section 4 and 5.

The overall results are showed in Figure 69. As can be noticed, a good agreement is achieved referred both at the pressure trace and at the HRR trace. The combustion appears to be a bit in early, indicating that, probably, the kernel model needs to be tweaked a little bit.

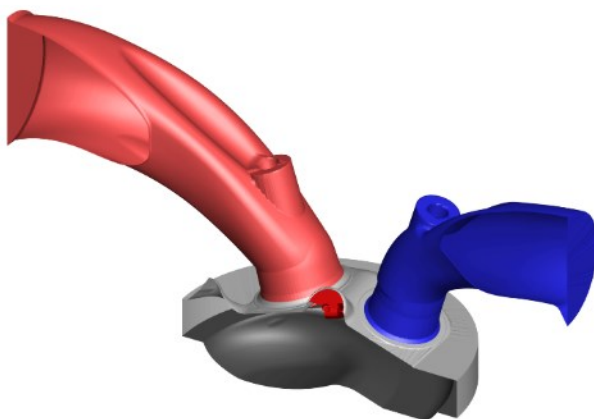


Figure 68 - The computational domain of the metal engine.

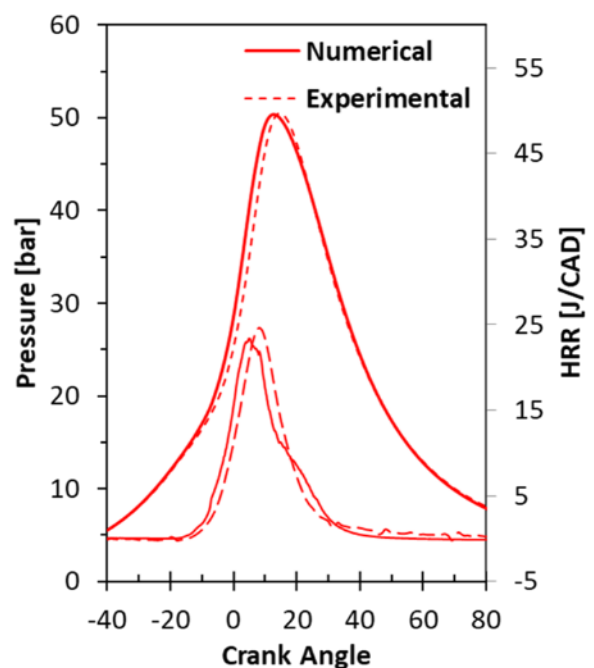


Figure 69 - Comparison between experimental and numerical pressure and heat release rate of the metal engine

The overall engine performances are summarized in Table 9. As can be seen, there is an overall agreement between the experimental and the predicted values.

|                     | <b>IMEP [bar]</b> | <b>Work[J]</b> | <b>IaHR[J]</b> |
|---------------------|-------------------|----------------|----------------|
| <b>Experimental</b> | 8.31              | 207            | 469            |
| <b>Modeled</b>      | 8.27              | 207            | 475            |

*Table 9 - Comparison between the experimental and modeled engines performance, metal engine*

## 5.6 Conclusions of chapter 5

In chapter five, all the results about the engine calculations have been presented.

The chapter opens with the comparison between the experimental and numerical pressure and aHRR traces and, after a brief discussion about the validation, a preliminary analysis of the pre-chamber engine was performed. The fundamental working phases of a TJI engine were identified and described, also by means of the pressure and aHRR traces evaluated separately in the pre and in the main chamber and by the flowrate exchanged between the two chambers. This led to the definition of the following phases: Filling & Scavenging, Mixing, Flame Propagation, Ejection, Reburning and Expulsion. Moreover, a more general approach to evaluate the net Heat Release Rate was purposed. This allowed the computation of the actual energy exchange between the two chambers, comprising the energy made available by the pre-chamber for the main charge ignition and an estimation of the ignition delay.

The cold phases were described singularly, concluding that the scavenging of an active pre-chamber is essentially performed by the fuel injection; by virtue of this, a charge stratification is observed in the mixing phase. Moreover, the poor scavenging capabilities contains in the pre-chamber about the 85% of the residual gasses of the previous cycle, helping to reduce HC emissions.

The combustion regime was, instead, analyzed in a single sub-section which provided information about the main charge ignition mechanism, also considering specific parameters as the Damkohler number, the strain rate and the Takeno Flame Index. The species distribution and evolution were evaluated both globally ( by means of volume averaged distribution) and locally, on lines located in characteristic points of the domain. This allowed to better investigate the ignition mechanism and the species conversion pathways.

The expulsion stage was analyzed separately from the combustion to highlight the pollutant formation pathways pointing out that the combustion in the pre-chamber evolves under moderately rich conditions while the one in the main chamber performs in lean conditions. The fuel rich combustion in the pre-chamber helps to reduce  $\text{NO}_x$  production thanks to the reburning mechanism while the lean condition of the main chamber helps to keep low both CO and HC. Nevertheless, the global  $\text{NO}_x$  production is still high, due to the low air dilution. Then, a check on the compressibility effects was performed, concluding that, for the analyzed configuration, the flow is not choked.

A comparison of the computed engine out emission was also purposed. The pre-chamber engine behaves better, in except for  $\text{NO}_x$ . Also, the fuel conversion efficiency is higher, as highlighted by the lower  $\text{CO}_2$  values per kWh.

Finally, a brief dissertation about the flame radius measurement performed with TJI systems was presented. Although difficult to obtain by means of experiments, a measure of the flame volume would be recommendable in order to compare the flame speed without making any assumption on the flame shape.

## 6. Scramjet simulations results

As introduced in the *Hydrogen combustion: scramjets applications for hypersonic flights* section, a global inspection of the flow path with preliminary validation against the experimental dataset given in [82] is provided, then, a more detailed analysis will be performed.

### 6.1 Overall flow analysis

A global view of the flow-field showing the instantaneous contours of pressure, Mach number and temperature is given in Figure 70 to Figure 72, respectively. Starting from the inlet profile, on the left, after some reflections on the cowl (upper) and body (lower) walls of the combustor, the oblique shocks reach the injection section and interact with the bow shock formed ahead of the  $H_2$  jet.

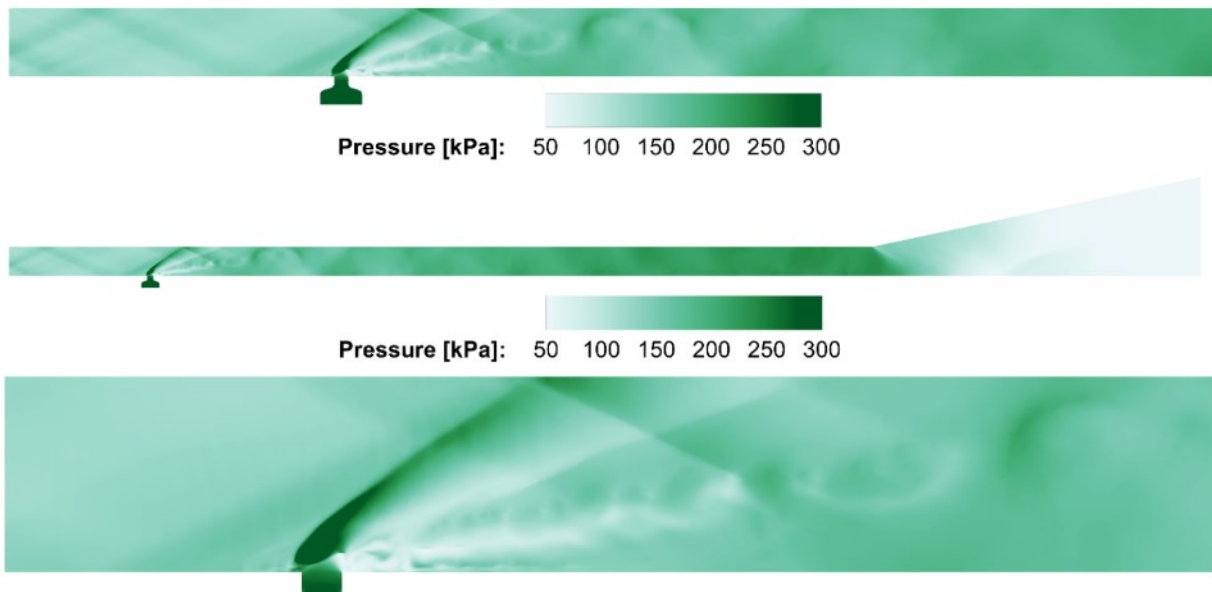


Figure 70 - Pressure contours in the symmetry plane. Top, the first quarter of the combustor; center, the whole combustor; bottom, a particular of the injection section

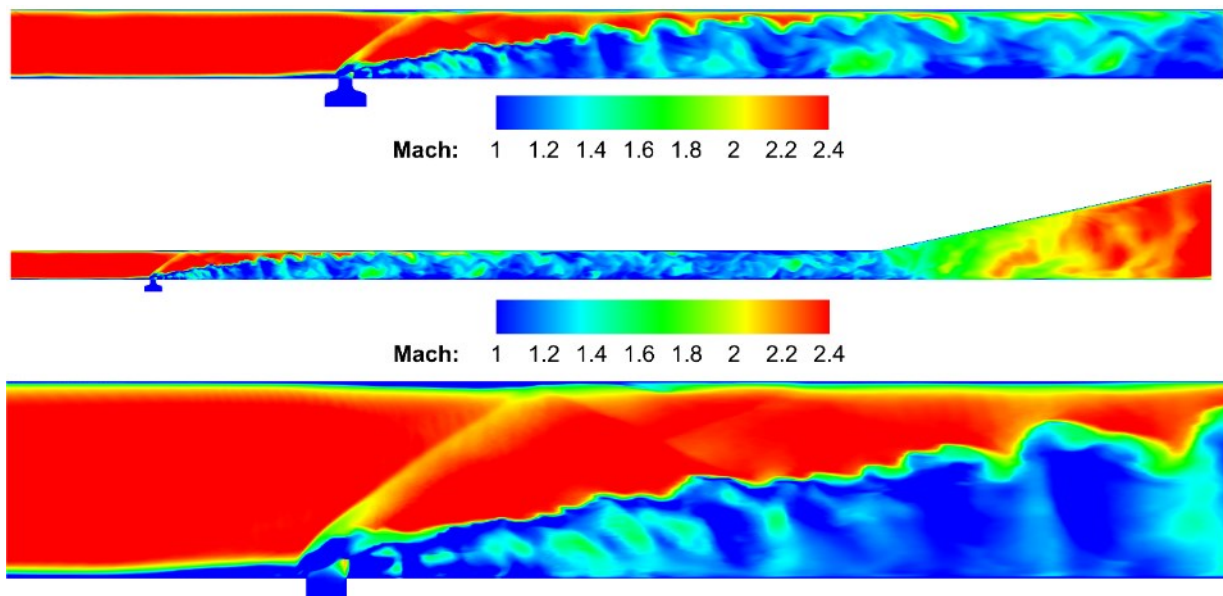


Figure 71 - Mach number contours in the symmetry plane. Top, the first quarter of the combustor; center, the whole combustor; bottom, a particular of the injection section

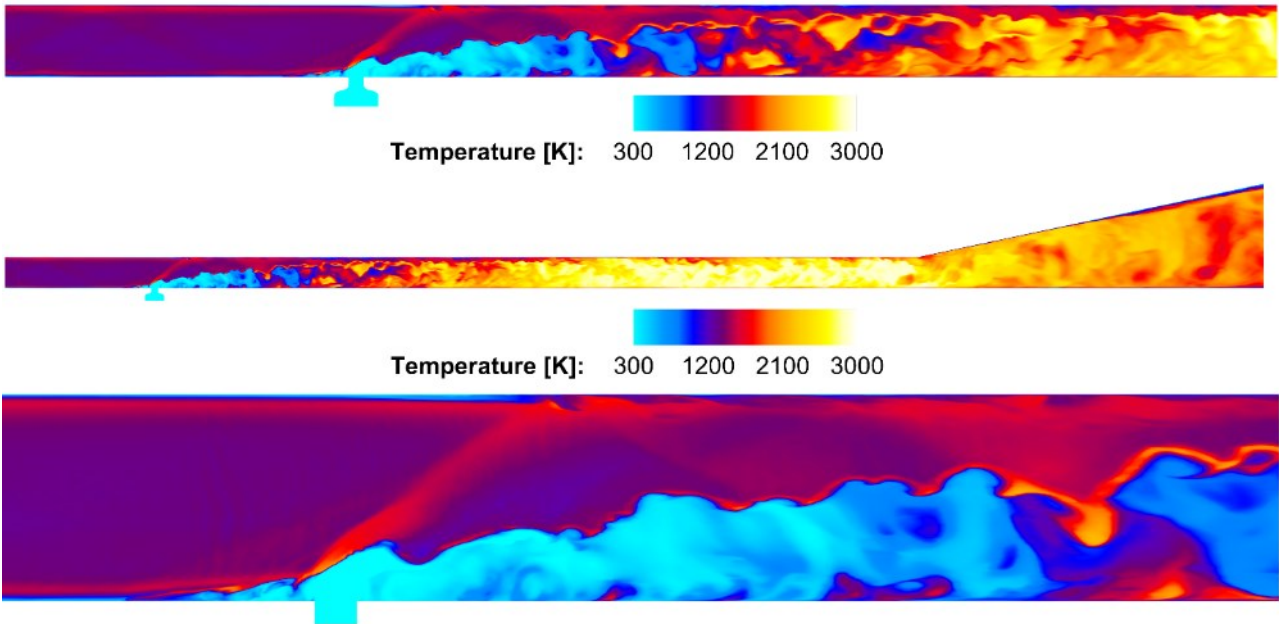


Figure 72 - Temperature contours in the symmetry plane. Top, the first quarter of the combustor; center, the whole combustor; bottom, a particular of the injection section

The high pressure gradient at the base of the bow shock generates a recirculation bubble just ahead of the porthole injector, as showed in Figure 81. Such bubble involves the formation of another weak oblique shock before the bow shock, as barely visible in Figure 72. The separation bubble generated ahead of the sonic Hydrogen injection acts as a mixing region between the fuel and the air contained in the sub-sonic boundary layer and a hovering vortex is established. Such a separation bubble can be also observed in Figure 74, where the density gradient is reported.

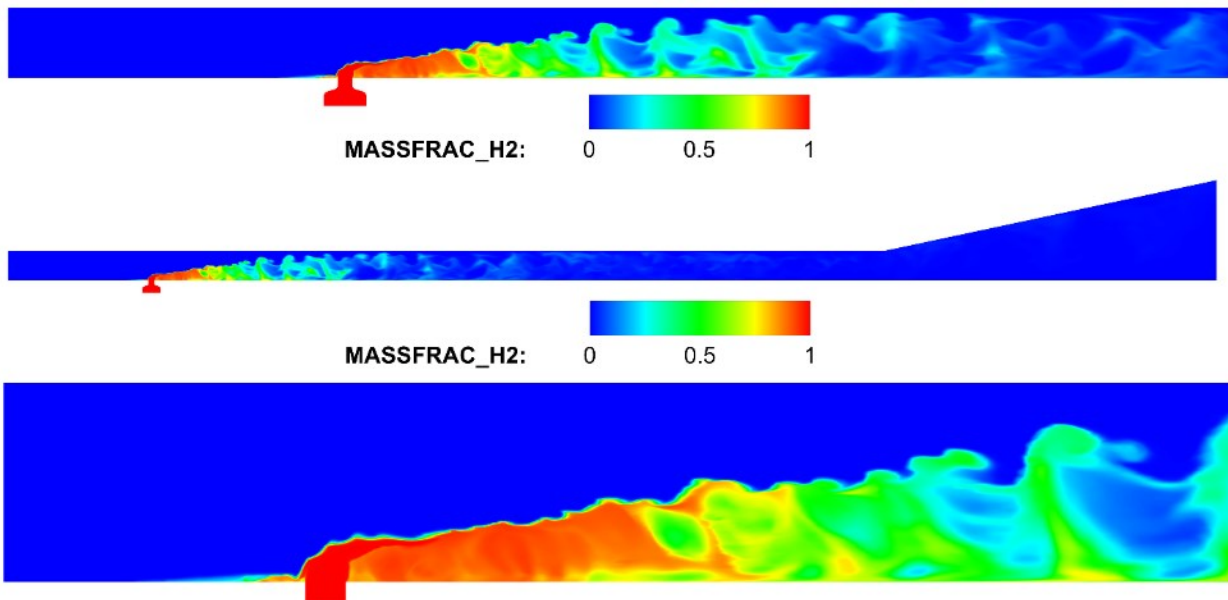


Figure 73 - Hydrogen mass fraction. Top, the first quarter of the combustor; center, the whole combustor; bottom, a particular of the injection section

Also the other structures described in Figure 81, as the expansion fan at the injector outflow, are clearly observable. Moreover, the shear layer streamwise extension can be quantified to be about one half of the combustor length starting from the injection point. Finally, the first shock reflections (the strongest) can be noticed.

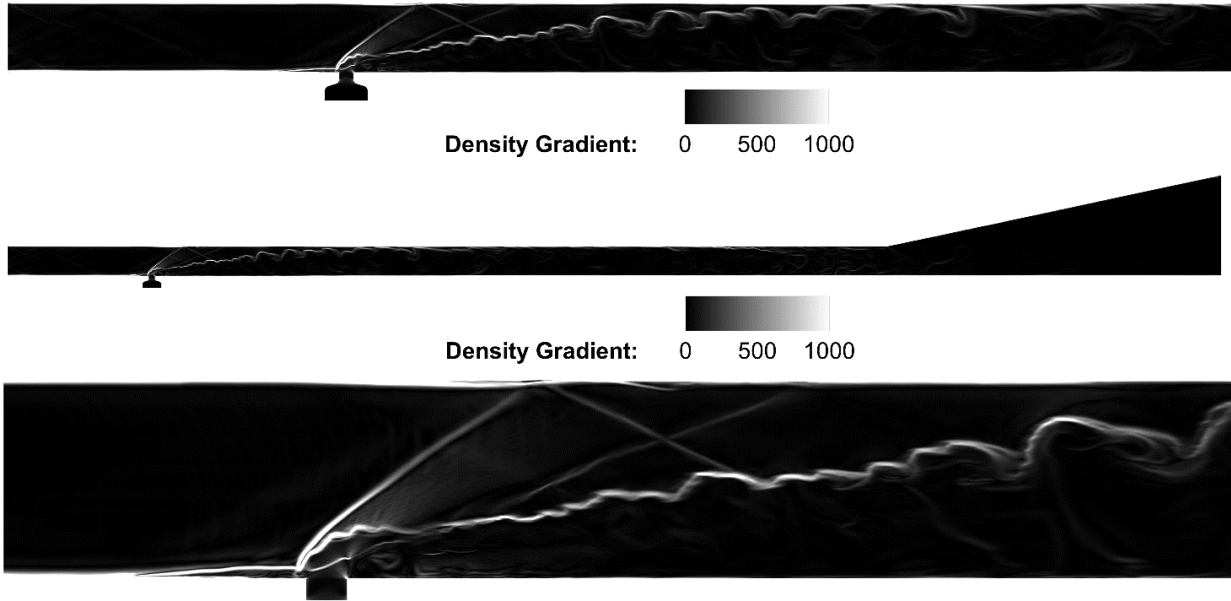


Figure 74 - Density gradient contours. Top, the first quarter of the combustor; center, the whole combustor; bottom, a particular of the injection section

Figure 72 to Figure 74 highlight the presence of a shear layer dividing the Hydrogen, at lower temperature, from the air. Subjected to the Kelvin-Helmholtz instability, large vortices detach from the shear layer promoting and enhancing the mixing between the fuel and the oxidizer. Considering the momentum flux ratio of this specific application,  $J = \frac{(\rho \cdot u^2)_{jet}}{(\rho \cdot u^2)_{air}} \approx 0.54$ , the interaction between the shocks, reflected by the cowl side wall, and the shear layer results in a further reflection [131] on the same shear layer (cf. Figure 74). Such successive shock reflections, together with the combustion progress, makes the pressure to increase along the combustion chamber, as reported in Figure 75. The non-monotonic behavior is due to the shocks reflections on the combustor walls. As can be noticed, the numerical predictions agree well with the experimental data and the shocks reflections are captured quite well [82], [132].

At the beginning of the expansion nozzle, a sudden pressure decrease is observed, followed by a continuous expansion. With respect to the inlet condition, the Mach number after the bow shock gradually reduces always remaining greater than one in the core flow all along the combustor, as shown in Figure 71. Moreover, Figure 72 indicates that peak temperatures of about 3000 K are achieved in the second half of the combustor before the divergent nozzle.

Figure 76 and Figure 77 is provided the comparison between the computed and the measured wall heat fluxes.

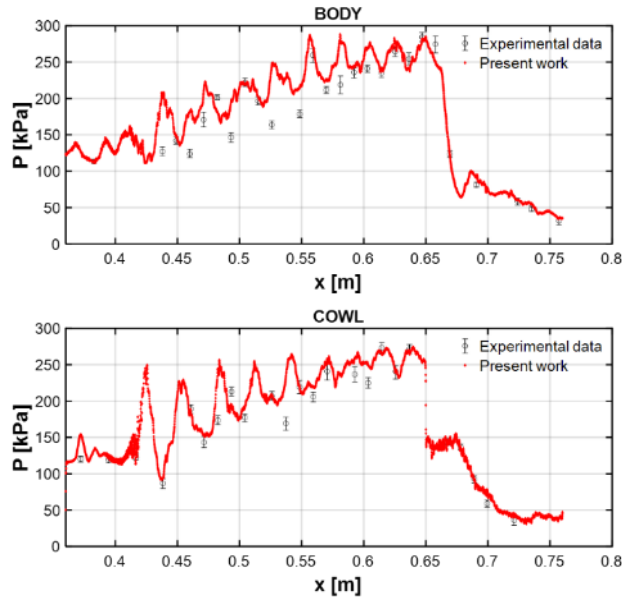


Figure 75 - Comparison between the experimental and numerical pressure distribution along the symmetry line of the combustor. The experimental data are taken from [82].

The values regarding two sections, namely 6 and 9 mm off the symmetry line, are reported. This choice is related on the uncertainty about the thermocouples position in regard of the experimental dataset analyzed in [133] and here employed as reference dataset. Considering the 6mm section, a good agreement is achieved, on the body side, until the injector. Then, the modeled heat flux is consistently under-predicted. The same applies to the cowl side.

Moving the attention on the other section, a qualitative better agreement was achieved. On the body side, in the second half of the combustor, the heat flux is slightly under predicted. It is worth saying that such behavior was not noticed in the preliminary RANS simulations which results are showed in Figure 78.

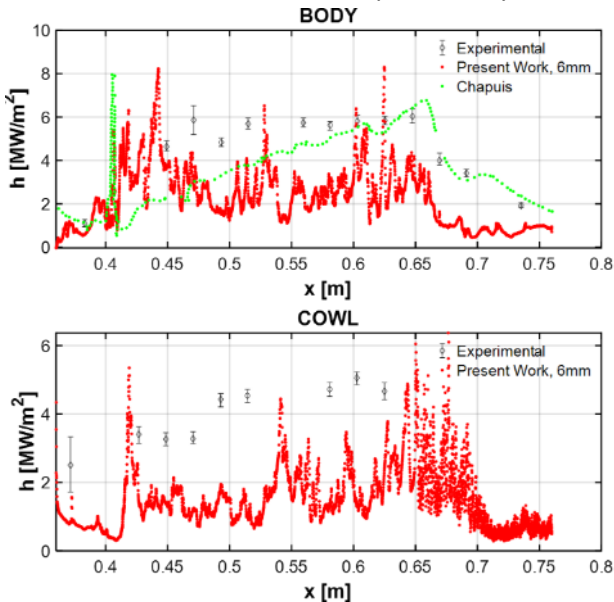


Figure 76 - Comparison between the experimental and numerical heat flux distribution along a line at 6mm from the symmetry line. The experimental data are taken from [82].

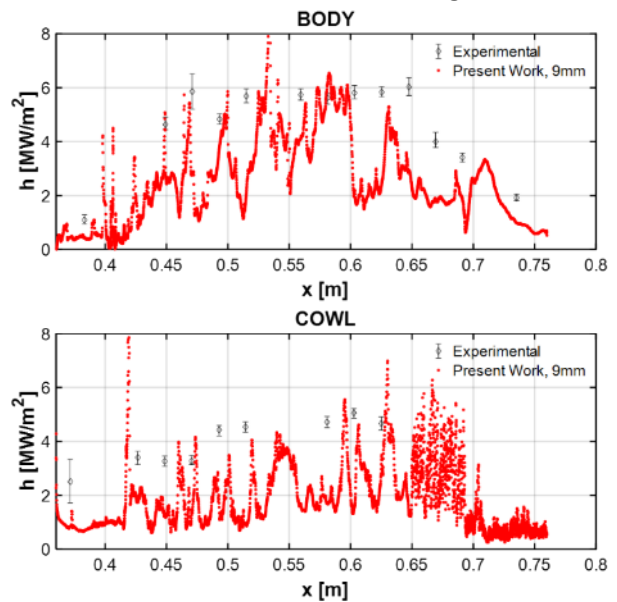


Figure 77 - Comparison between the experimental and numerical heat flux distribution along a line at 9mm from the symmetry line. The experimental data are taken from [82].

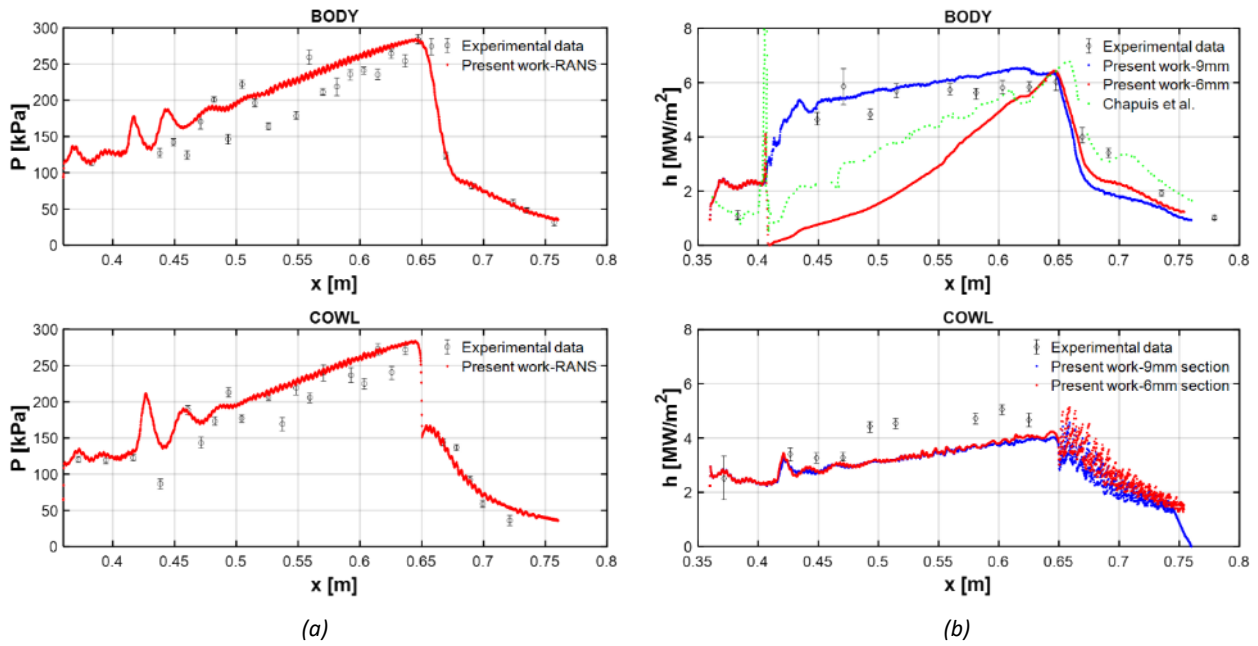


Figure 78 - Preliminary RANS simulation results: (a), pressure distributions; (b) heat-flux distributions.

## 6.2 Detailed flow analysis

A deeper analysis of the flow field will be now performed, focusing the attention on the injection section. By analyzing the second invariant of the velocity gradient tensor, the so-called Q-criterion, a representation of the vortices of major interest can be achieved.

Figure 79 reports the iso-surface of a positive value of Q colored with temperature. Near the injector, left portion of the figure, the horseshow vortex is observed. Such structure is due to the recirculation bubble mentioned in the previous section and gets aligned with the flow at about  $x/D \approx 5$ , where  $D$  is the diameter of the injector ( $D = 2\text{mm}$ ). Moreover, in consequence of the injection, two Counter rotating Vortices forming a Pair (CVP) establish behind the injector and remain coherent until about  $x/D \approx 7$ . Moving along the combustor ( $10 < x/D < 20$ ), smaller vortices detach from the shear layer, generated by the Kelvin-Helmholtz instability, and gradually destroy the CVP [134]. From the interaction between these two families of vortex,  $\Omega$ -shaped vortices are formed at  $x/D > 15$ . Such vortices are intensively stretched by the shear stresses induced by the interaction with walls and are destroyed beyond  $x/D > 70$ , originating a disordered turbulent flow.

On the base of these observations, the flow can be divided in three regions: 1) A near field region ( $x/D < 5$ ) close to the injector characterized by coherent vortex structures including the CVP and vortex rings. 2) A transition region ( $10 < x/D < 20$ ), in which these coherent structures break, originating the  $\Omega$ -shaped vortices. The latter vortices induce bursts in this region leading to the fragmentation of the coherent structures; turbulence is developing and the mixing between air and fuel is enhanced. 3) A turbulent region ( $x/D > 70$ ), in which the fully developed turbulent flow develops [135]. A graphical representation, purposed by You et al. in [136], is reported in Figure 80 for comparison.

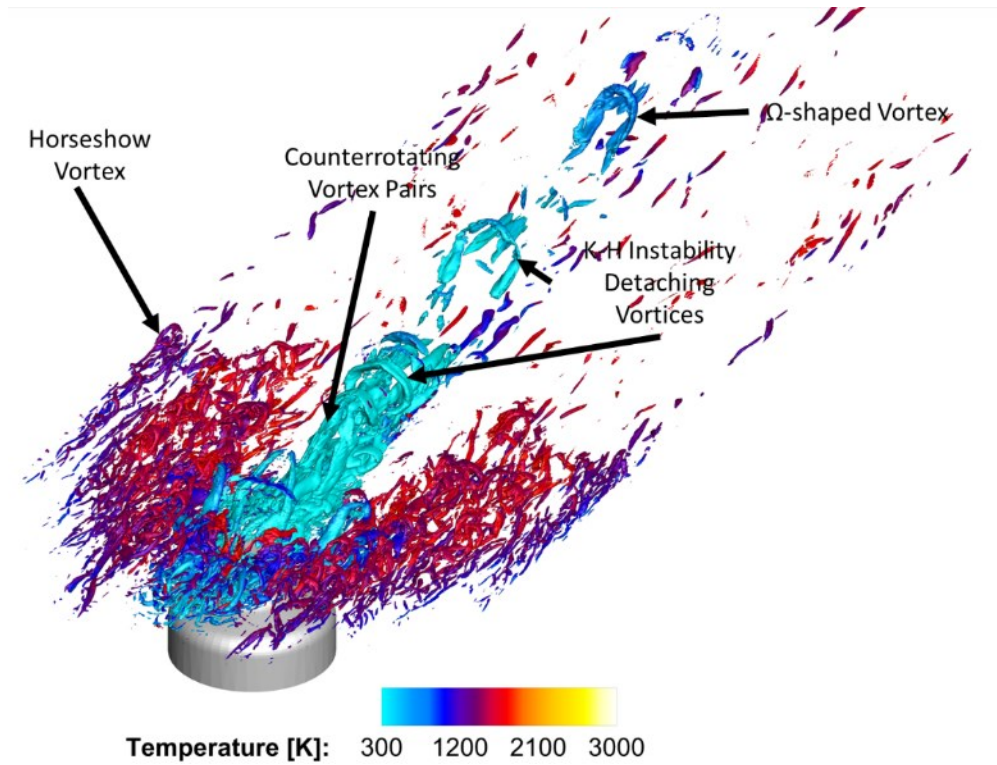


Figure 79 - Q-criterion iso-surfaces colored with temperature.

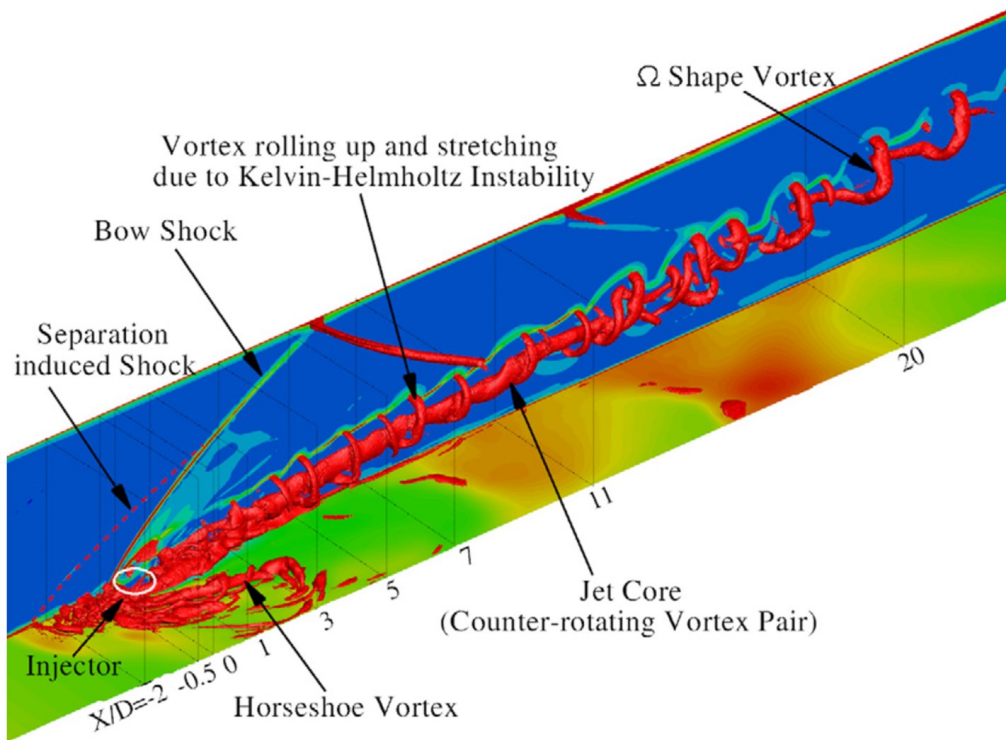


Figure 80 - Representation of the main vortical structures in the HyShot II combustor [136].

In the near field region, the interaction of the two perpendicular flows is very complex, being the pressure at the exit of the injector nozzle, downstream of the bow shock, not uniform. Since the Hydrogen jet behaves like an obstacle for the horizontal air stream, the pressure upstream of the jet is higher than the pressure downstream, also due to the effect of the wake behind the jet. Therefore, the average value of the pressure in the upstream part of the jet (left) is greater than the sonic jet pressure, and the fuel flow is over-expanded

in that region, as can be observed in Figure 70 and Figure 81. Consequently, a compression shock is formed, which has a three-dimensional shape (indicated with a dashed black line in the same figure). A typical flow structure, referred as barrel shock, is found at the downstream part of the jet, composed of a windward shock branch and leeward shock branch [131]. These two branches are connected by a Mach disk. At the downstream part of the jet, where the pressure is lower due to the wake effect, the fuel flow is under-expanded. Therefore, the jet internally expands through a Prandtl-Meyer fan at the downstream corner of the injector. Then, the flow is compressed by the leeward branch of the barrel shock and the Mach disk. Figure 81 also provides the streamlines of the flow in the plane, showing a source (*node*) point in the region downstream of the injector, in agreement with the results of [137], originated from the reattachment of the crossbow traveling around the jet -cf. Figure 79. The streamlines in Figure 81 show that most of the Hydrogen passes through the windward branch of the barrel shock wave instead of the leeward branch. The Hydrogen jet is supersonic inside the barrel-shock region, with a peak Mach number of about 2.15, and then drop to subsonic behind the Mach disk. One can observe that, passing through the windward side of the barrel shock and the Mach disk, the Hydrogen plume bends quickly towards the streamwise direction, remaining quite close to the wall. This is a typical feature of transverse injection with a low value of the momentum flux ratio [131] and is related to the shear layer formation.

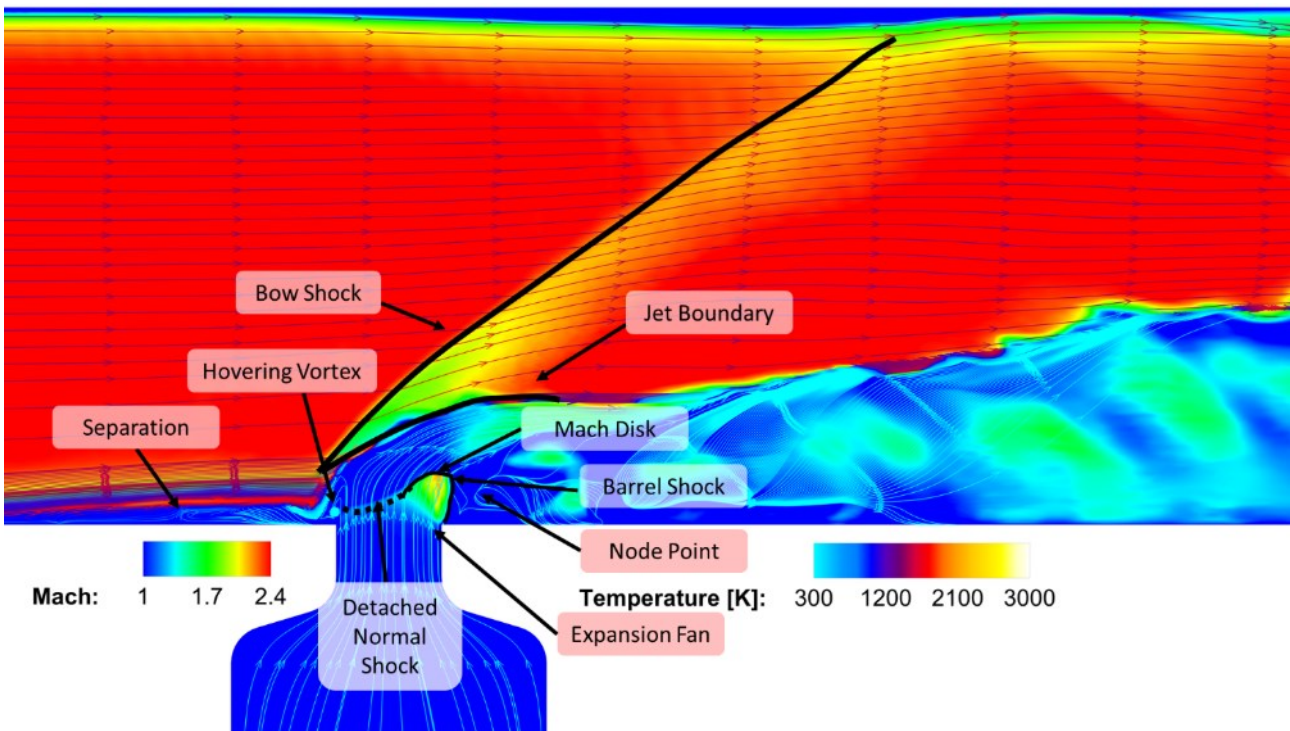


Figure 81 - Flow structures near the injector. Velocity streamlines colored with temperature.

The complex flow interaction is well captured thanks to the AMR algorithm. Indeed, the grid spacing is reduced in correspondence of strong velocity and temperature gradients, as shown in Figure 82.

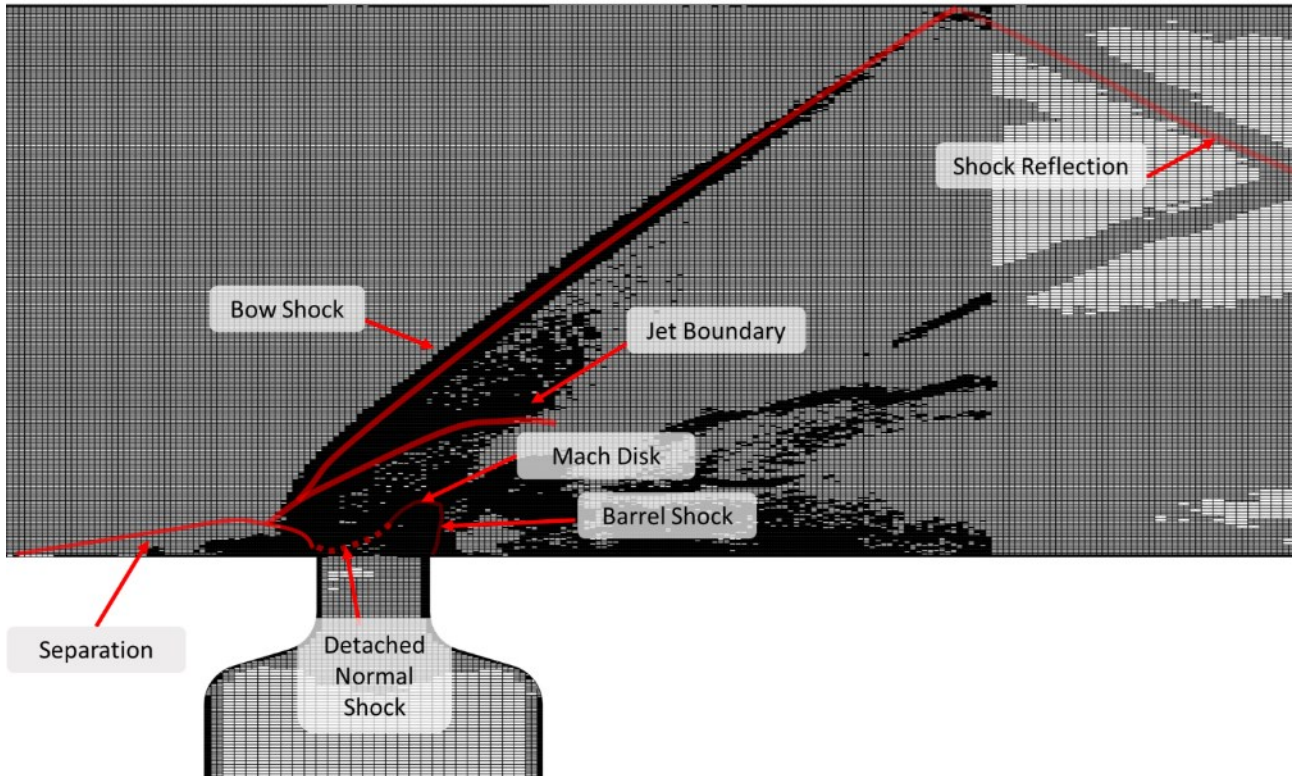


Figure 82 - Snapshot of the computational grid in the injection section.

Figure 83 shows the vorticity contours at  $x = \text{const}$  planes perpendicular to the flow direction for different locations from the injector. At  $x/D = 0$ , the early CVP can be observed in correspondence of the injector outflow. In the same slice, located at about  $z = 1.5D$  from the injector axis, the horseshow vortex can be noticed. Moving to  $x/D = 1$ , the CVP dimension increases, as well as, the dimension of the horseshow. When  $x/D = 2$ , the CVP gets “compressed”, generating the so-called *Tailored Counter Rotating Pair*. The horseshow vortex is now barely noticeable. At  $x/D = 3$ , the CVP vortices starts to lose their coherence and becomes even smaller. The horseshow vortex gets expanded in the transverse direction. From these observations, it appears that the near-field mixing is controlled by convection transport while the far-field mixing is controlled by mass diffusion [138], [139]. At higher distances from the injector, the  $\Omega$ -shaped vortices start to form, as can be observed at  $x/D = 15$ . At  $x/D = 20$  the flow has almost lost its coherence. A tailored vortex can be observed on the upper edges of Figure 83 at  $x/D = 20$ . These flow structures are crucial for combustion development, as will be discussed in the next subsection, being responsible for species exchange between the outer hot and Oxygen rich flow and the colder fuel plume.

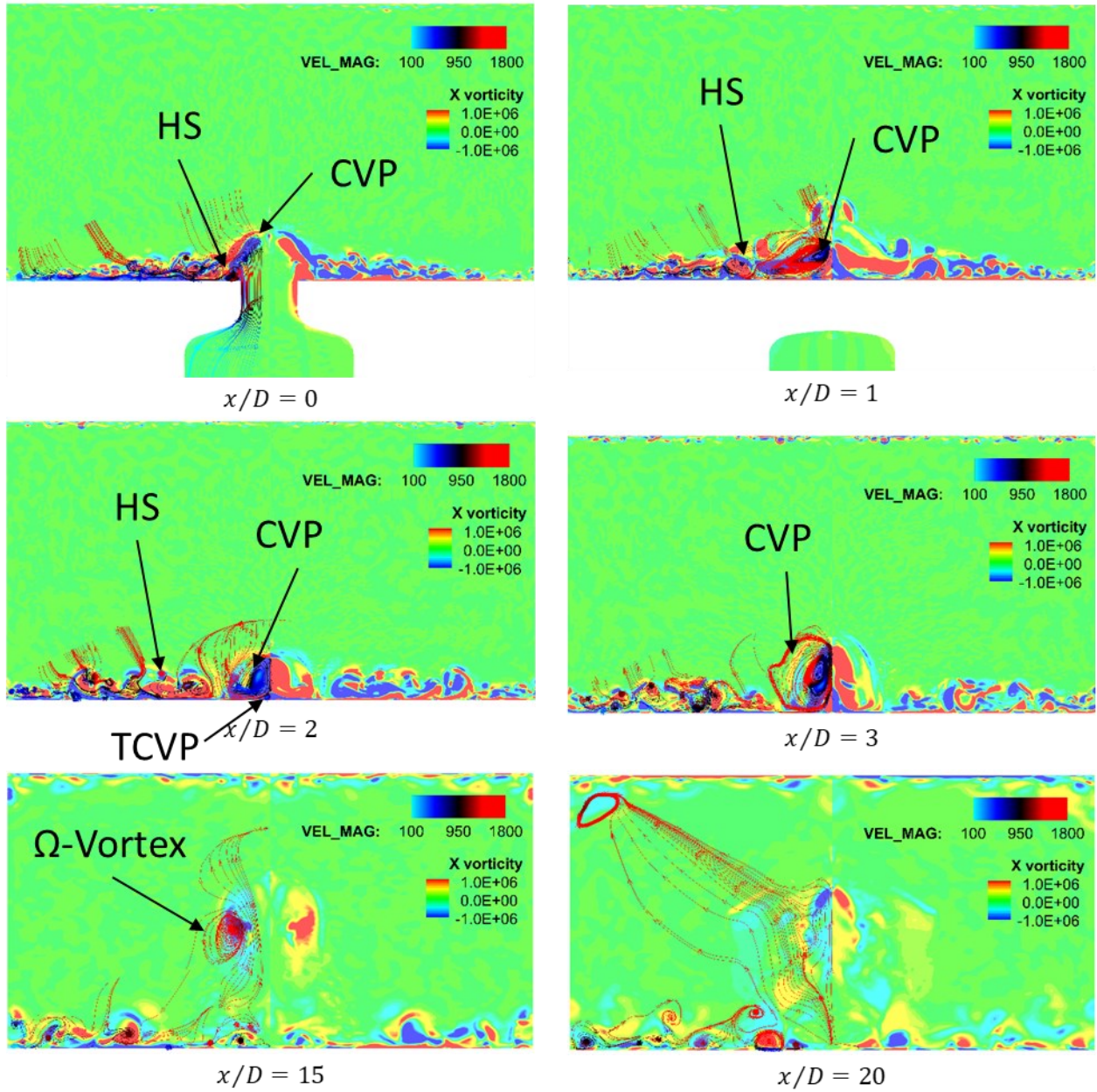


Figure 83 – Vorticity contours and streamlines at different locations in the flow direction.

### 6.3 Combustion regime

Generally, the operation of a scramjet combustor is based on the auto-ignition of the mixture, which depends on four main variables: the static temperature and pressure, the mixture composition and the residence time. If the mixture composition is favorable (i.e., it falls in the ignition limits), higher temperatures and residence times promotes the auto-ignition. However, when considering the ignition of supersonic crossflows, the residence times (also representative of the time available for mixing) and the ignition delay may be of the same order of magnitude.

The local temperature rise due to the shockwaves train in the combustor promotes auto-ignition. For the present case, the total temperature is about 2600K, corresponding to a total enthalpy of about 2.7 MJ/kg, conditions that can lead to auto-ignition.

Due to the low temperature of the injected Hydrogen, a high temperature gradient, opposed to the equivalence ratio gradient, establishes across the mixing layer, around the Hydrogen plume. The colder mixture is then located in the richer zones of the mixing layer.

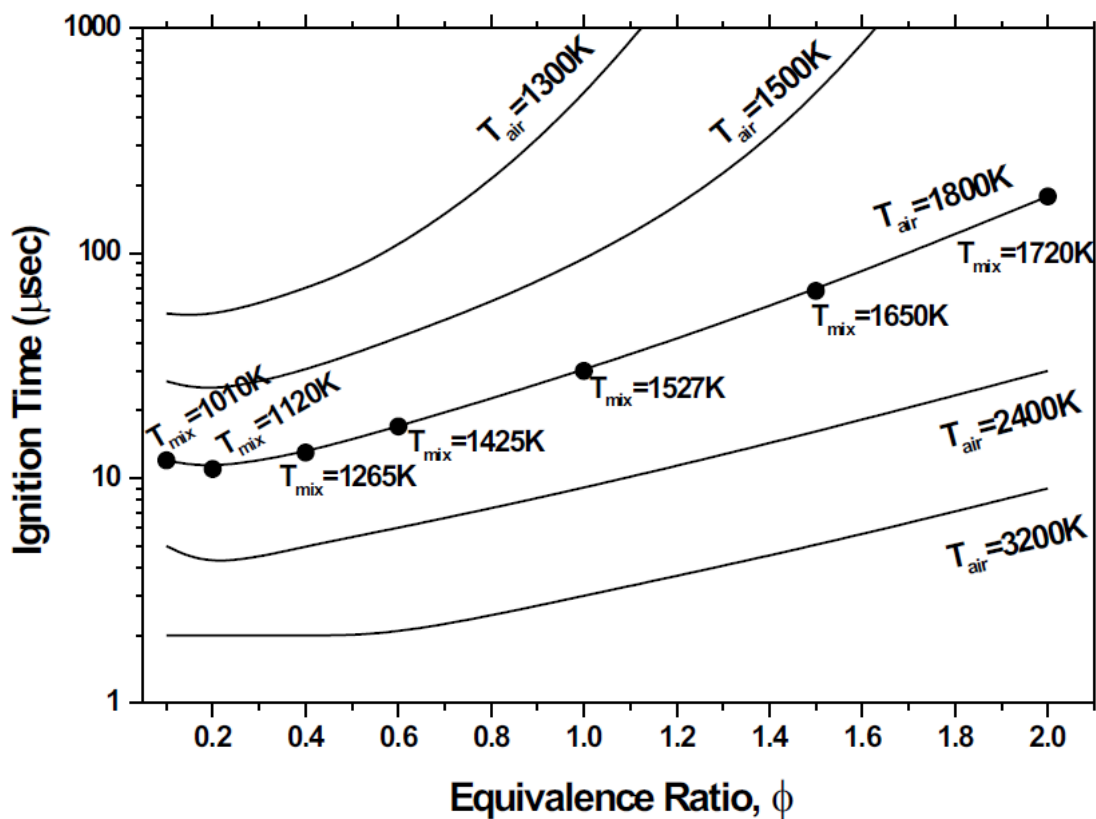


Figure 84 - Ignition time for cold Hydrogen (300K) injected in hot air [134].

As reported in Figure 84, the ignition delay of a mixture of cold Hydrogen and hot air decreases with temperature and achieve the minimum values at low equivalence ratios. Therefore, the auto-ignition points will lay on the lean side of the mixing layer.

By an experimental point of view, combusting zone can be identified by the OH Planar Laser-Induced Fluorescence (PLIF) technique [140], [141]. The hydroxyl radical (OH) is a reactive radical involved in all the high temperature combustion regarding air and Hydrogen-based fuels and is representative of the propagation, branching and termination phases of the combustion. Initiation reactions, instead, are represented by the presence of the hydroperoxyl radical ( $HO_2$ ).

A snapshot of the contours of the OH mass fraction is shown in Figure 85. As can be observed, a continuous thin flow region, corresponding to the shear layer, with high OH concentration is present. It appears that, in the near-field and transition zone, the OH appears confined into such a corrugated thin structure. Such a feature was also identified in the experiments reported in [140], [141].

By comparing the OH observation with the product ( $H_2O$ ) mass fraction, reported in Figure 86, one can conclude that auto-ignition can occur in the shear layer between the two fluids until the transition zone ( $x/D < 20$ ). Indeed, the presence of the OH radicals indicates that the branching reactions have started and initiation has already happened.

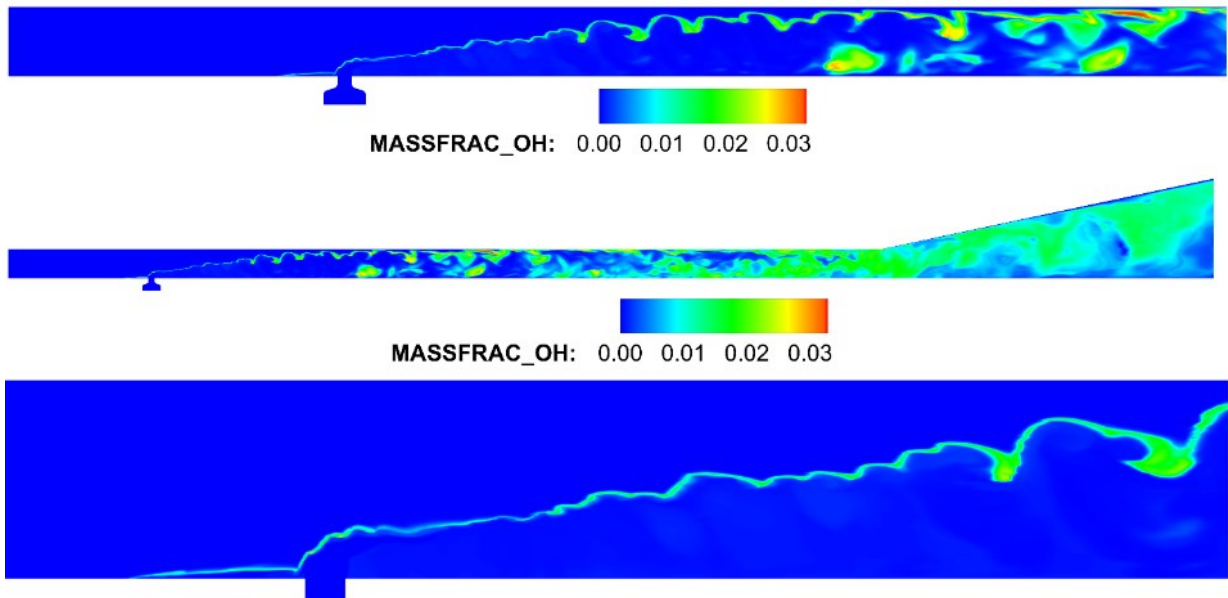


Figure 85 - OH mass fraction contours. Top, the first quarter of the combustor; center, the whole combustor; bottom, a particular of the injection section

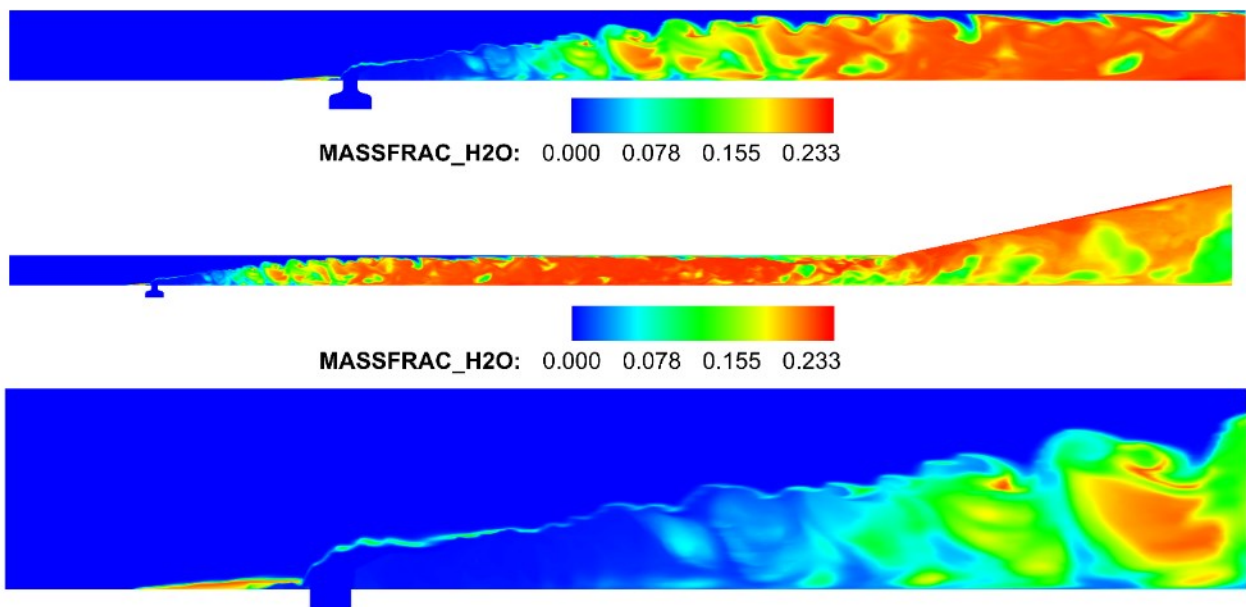


Figure 86 –  $H_2O$  mass fraction contours. Top, the first quarter of the combustor; center, the whole combustor; bottom, a particular of the injection section

The pressure and temperature distributions across the bow shock (cf. Figure 70 and Figure 72) are in the

range of 1-2 bar and 2500-1500K, respectively with an ignition time ranging between 2 and 30  $\mu$ s. The shorter ignition time is found just behind the bow shock, in a region characterized by a relatively high shear rate and low velocity. Considering the low values of the water mass fraction, it is reasonable that ignition is quenched. Moreover, the OH distribution, appears to be not monotone in the combustor. Indeed, there are higher values just behind the bow shock and in the recirculation regions, corresponding to the heads of the  $\Omega$ -vortices, just above the shear layer. Similar considerations can be achieved by considering the chemical source term, shown in Figure 88. Higher values of such term are found to be behind the bow shock and on the mixing layer. The plume is characterized by null values of the chemical source term, indicating poor mixing and ignition-prohibitive conditions. The same appears from the OH concentration.

Further downstream along the shear layer, ignition times are longer, and velocities are higher so that the ignition length can be as high as 50 D, which corresponds to the beginning of the region of high heat release and higher temperatures, where turbulence is developed and the three-body recombination reactions can take place. However, since OH is quickly produced at the beginning of the reaction and has a slow rate of recombination, it is very difficult to determine whether the presence of OH is due to local production or transport from other regions of the flow field. For this reason, the distribution of faster marker of auto-ignition can be analyzed, namely the hydroperoxyl radical  $\text{HO}_2$ , provided in Figure 87. It appears that  $\text{HO}_2$  concentration is negligible outside of the transition zone.

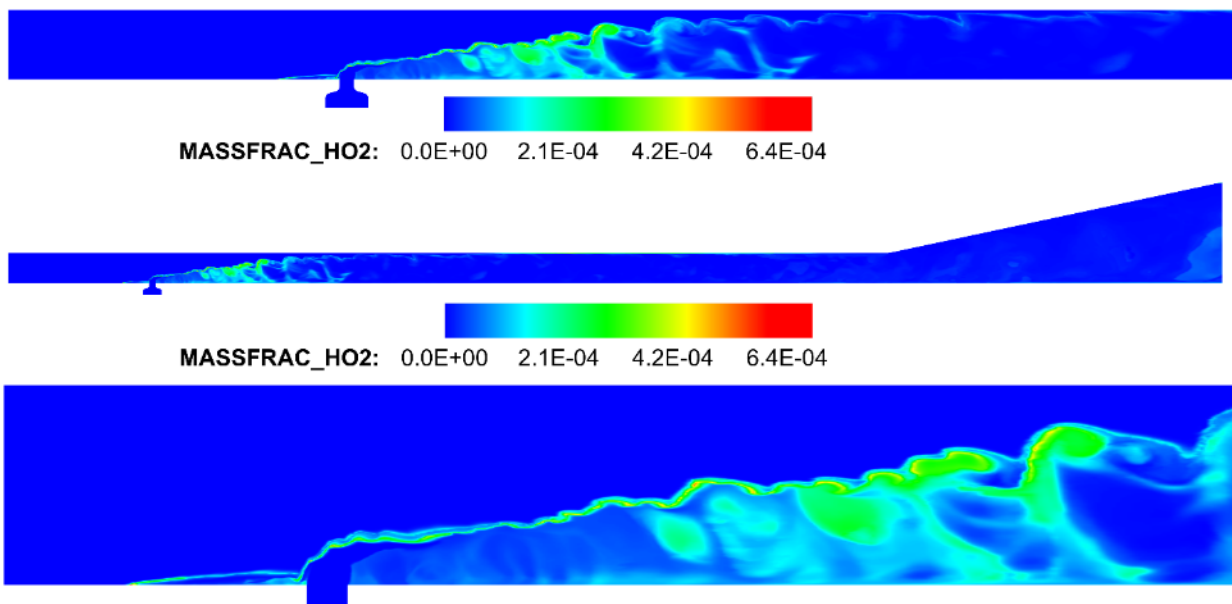


Figure 87 –  $\text{HO}_2$  mass fraction contours. Top, the first quarter of the combustor; center, the whole combustor; bottom, a particular of the injection section

In the transition region ( $x/D < 20$ ), under the shear layer envelope, the mixture temperature raise is also due to the entrainment of air, as can be inferred by considering the water mass fraction (Figure 86). Moreover, the presence of coherent structures, as the  $\Omega$ -vortices, creates high residence time zones. In such zones, mixing has more time to be completed and the mixture ignition and combustion can occur, as demonstrated both by the water mass fraction and by the chemical source term, Figure 86 and Figure 88, respectively.

The separation region ( $-4 < x/D < 0$ ) is instead characterized by high values of OH, concentrated in the shear layer of the recirculation zone, showing also noticeable concentration of  $\text{HO}_2$ . Moreover, the presence of  $\text{H}_2\text{O}$  in the shear layer of the recirculation bubble suggests that the mixture is burning and OH are transported inside of the bubble. Also the chemical source term is positive in the bubble and shows high

values in the mixing layer of the separation zone.

Acting in this way, the bubble can contribute to enhance the combustion efficiency and, above all, the flame stabilization [131]. Such effect is enhanced by the presence of subsonic regions, which are mainly found downstream of the bow shock, downstream of the Mach disk, inside of the  $\Omega$ -vortices and in the boundary layer close to the walls, as can be observed in Figure 71.

Moving to the turbulent region ( $x/D > 70$ ), the iso-surface of the stoichiometric mixture fraction ( $z_{st}$ ), reported in Figure 89, gets wrinkled, indicating a severe mixing, due to the fully developed turbulent flow reigning in that region. At the same time, one can observe both higher temperatures and wider OH concentrations. Considering also the water distribution, it can be observed that moving along the combustor, a great part of the total heat is released before the expanding nozzle.

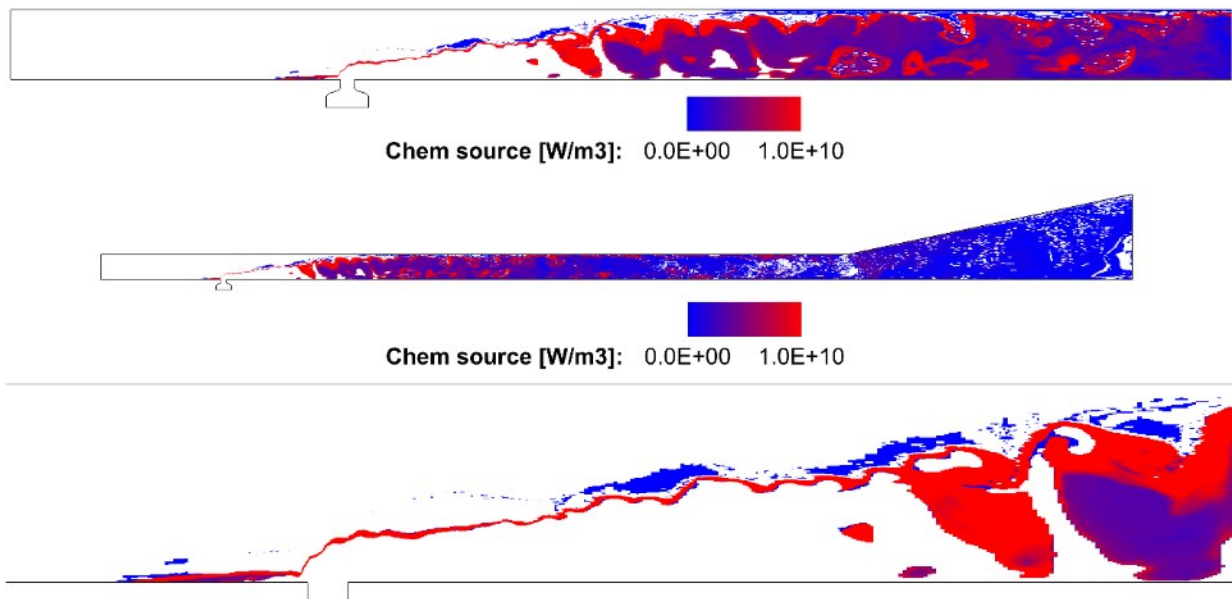


Figure 88 - Chemical source term. The white zones are characterized by null or negative values. Top, the first quarter of the combustor; center, the whole combustor; bottom, a particular of the injection section.

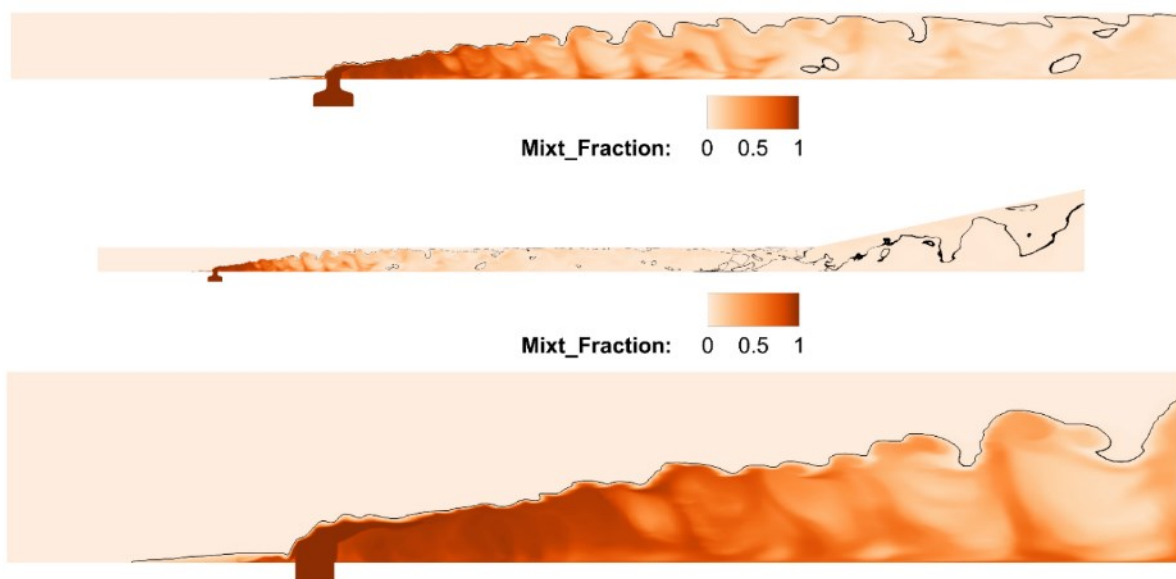


Figure 89 - Mixture fraction contours and stoichiometric iso-line. Top, the first quarter of the combustor; center, the whole combustor; bottom, a particular of the injection section

Figure 90 to Figure 93 provide the chemical source terms contours of  $H_2$ ,  $HO_2$ ,  $OH$  and  $H_2O$ , respectively. Please note that the legend was chosen in order to show only positive and negative values. This causes the spurious oscillations in the representation and some small values being included in the white (zero value) regions.

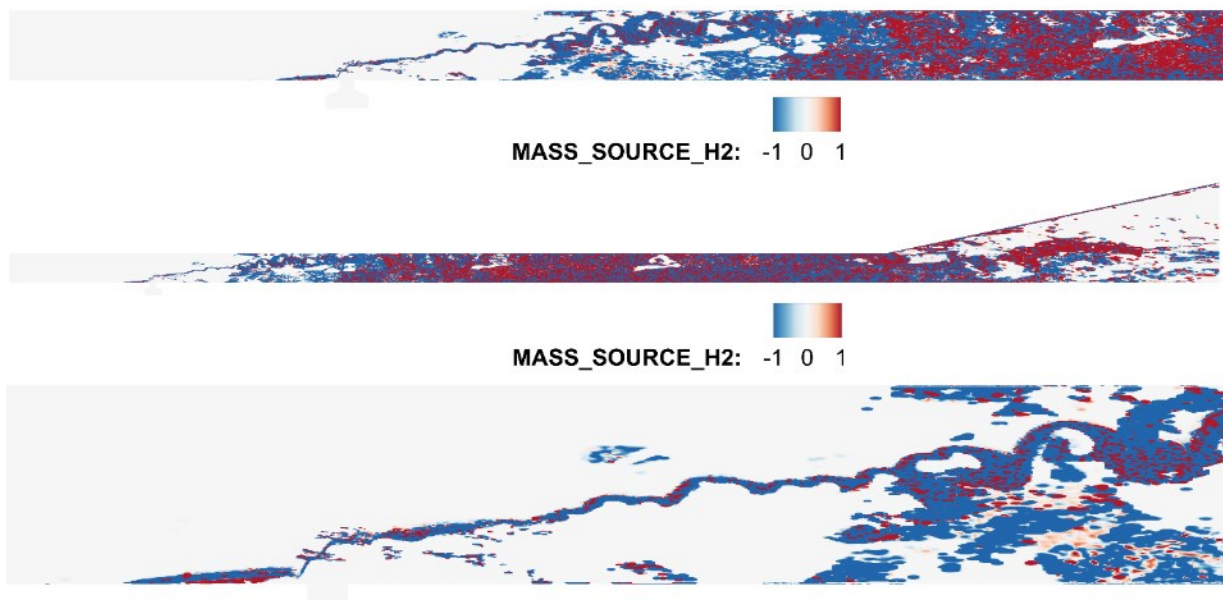


Figure 90 –  $H_2$  Mass source term contours. Top, the first quarter of the combustor; center, the whole combustor; bottom, a particular of the injection section

The Hydrogen mass source term presents negative value, indicating its consumption, in the recirculation zone and just ahead of the bow shock. At the same time, the Hydroperoxyl radical source term distribution, Figure 91, shows that, actually, ignition seems to occur just ahead of the bow shock and across the recirculation zone. Also, the shear layer is characterized by positive values of such term. The region behind the bow shock, also due to unfavorable mixing conditions (cf. Figure 89), is characterized mainly by null or fluctuating values, as can be inferred also to the values of the chemical source term. Moving the attention on the Hydroxyl radical, Figure 95, one can observe that across the bow shock, on its lower portion, there are both positive and negative values. This observation, with the positive values of the water source term in this zone, suggests that, somehow, combustion is proceeding in this thin region. Also the recirculation zone shows both positive and negative values, meaning that ignition and combustion actually occurs in that region. Moving further, along the combustor the source terms of these two radicals are present also in regions characterized by very low concentrations (e.g., in the shear layer plume). This suggests that, probably, the reason why combustion mainly develops across the second and third quarter of the combustor may be related to mixing issues more than on prohibitive flow-field conditions. This also indicates that there is, actually, a production of intermediate species and their presence is not only related to transport. Moreover, the vortices between the transition and the fully turbulent zones, promotes the mixing between the reactive species formed in the shear layer and the Hydrogen plume. This relates with the values of active radicals (like  $OH$ , Figure 85) registered under the shear layer and with the spotted peaks of the chemical source term of Figure 88. The species source terms are fluctuating in this region, indicating that fuel conversion is essentially ongoing. The direct comparison of Figure 92 with Figure 72 relates the severe temperature rise with the intense branching happening in the central portion of the combustor, where the flow is fully turbulent. Such high temperatures may bring to water dissociation, as reported in Figure 93. This can explain the values of water mass fraction reported in Figure 86. The white plumes in the expanding nozzle reported in Figure 91 to Figure

93 are related to imaging issues. As can be deemed by Figure 88, combustion is proceeding and the species source terms are non-zero. Anyway, Hydrogen is still present at the combustor outflow, indicating that the combustion is partially incomplete. About the 6% of the injected fuel is not converted in the combustor. For the sake of completeness, the present combustor section achieved a thrust of about 12 N with a specific impulse of about  $2700 \text{ s}^{-1}$ .

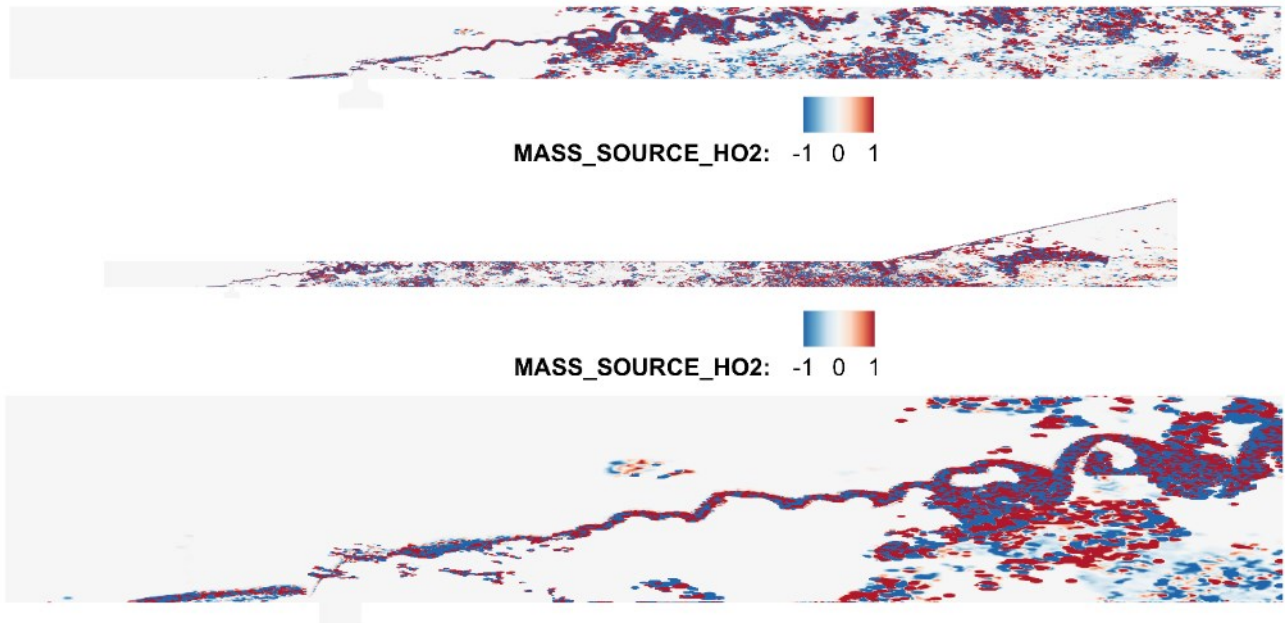


Figure 91 -  $\text{HO}_2$  Mass source term contours. Top, the first quarter of the combustor; center, the whole combustor; bottom, a particular of the injection section

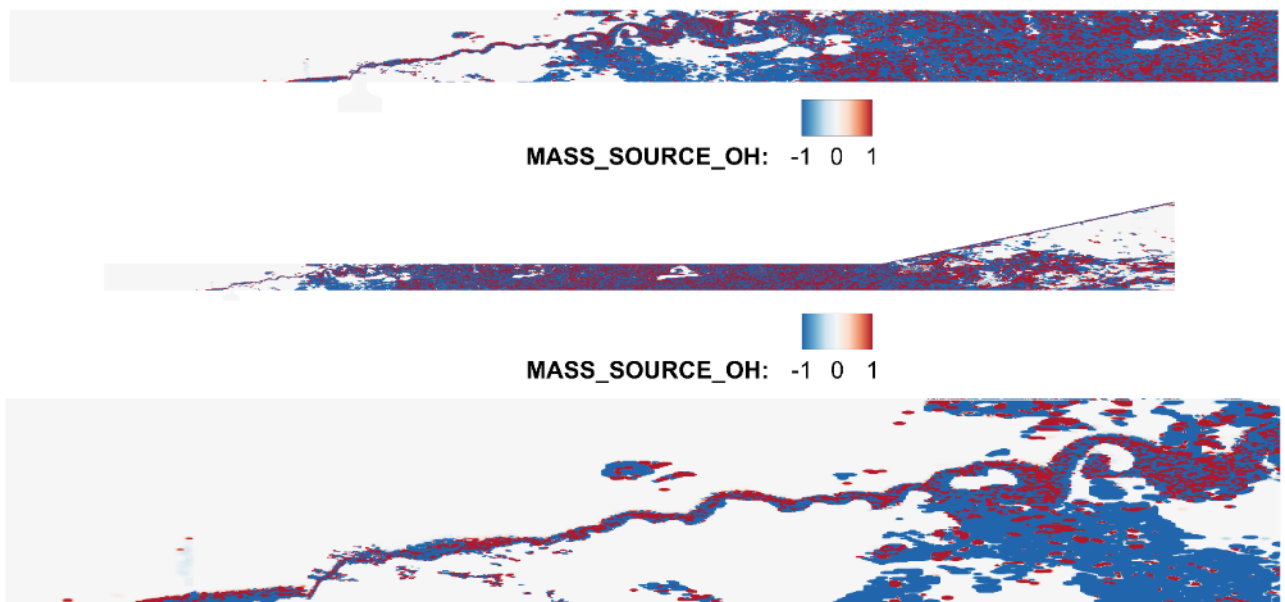


Figure 92 -  $\text{OH}$  Mass source term contours. Top, the first quarter of the combustor; center, the whole combustor; bottom, a particular of the injection section

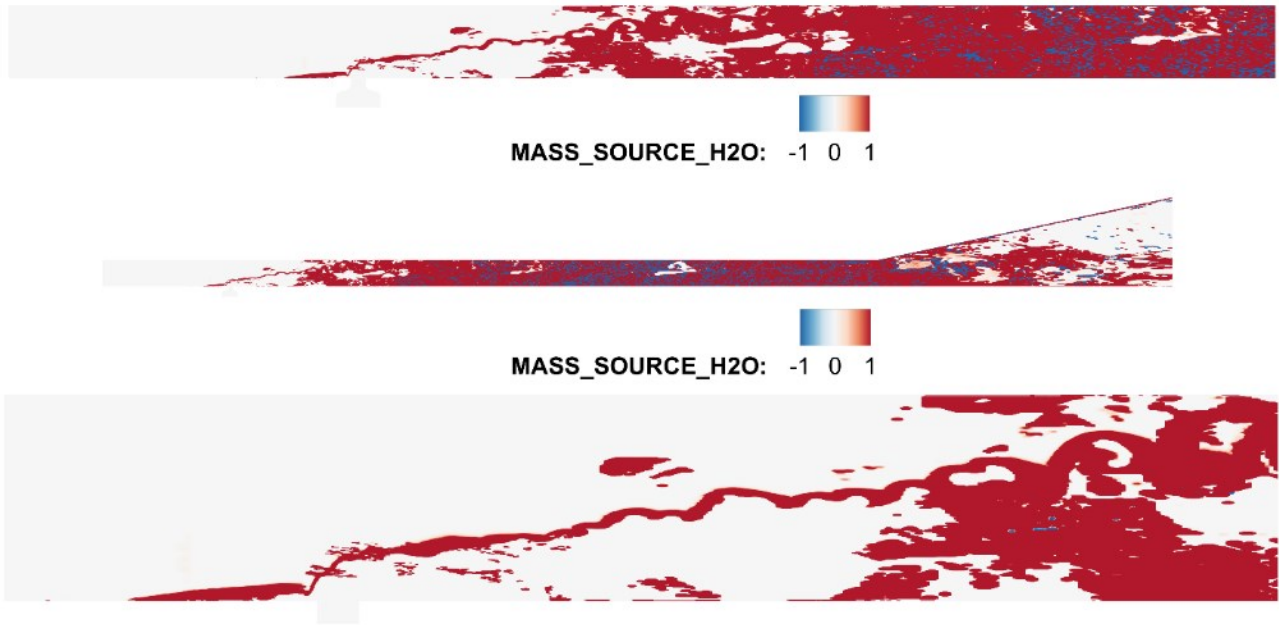


Figure 93 -  $H_2O$  Mass source term contours. Top, the first quarter of the combustor; center, the whole combustor; bottom, a particular of the injection section

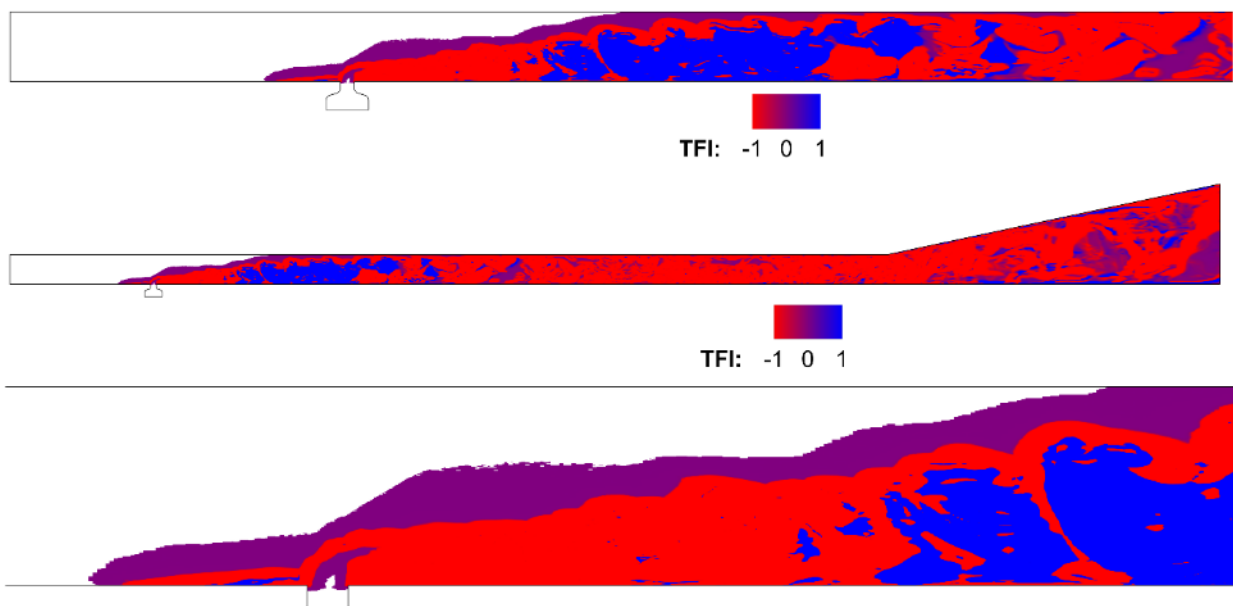


Figure 94 - The computed Takeno Flame Index. Top, the first quarter of the combustor; center, the whole combustor; bottom, a particular of the injection section. The white regions are characterized by null values

Concerning the nature of the combustion, the Takeno Flame Index (TFI), reported in Figure 94, indicates that the combustion is mainly of non-premixed type ( $TFI < 0$ ). However, some premixed zones can be noticed in the transition region, due to the effects of the coherent vortices. In this region, the mixture fraction is greater than the stoichiometric ( $z > z_{st}$ ) and the temperatures are lower than elsewhere, cf. Figure 72, thus the combustion is propagated by heat conduction and species transport from the external burning mixture. Figure 95 reports the scatter-plot of the temperature against the mixture fraction colored with the modulus of the strain-rate tensor, whose contour are reported for comparison purpose in Figure 96. It appears that the regions with high strain rate hindering ignition are below the mixing line (the blue dotted line) and are mainly located just behind the injector, in the Hydrogen plume. The points above the mixing line with  $z$  in

the neighbor of the stoichiometric value can be located by comparing Figure 95 with Figure 89 and Figure 72. Higher temperatures correspond to the regions where auto-ignition and combustion occurs; the medium temperature points are, instead, found in zones where rapid compression occurs. The other intermediate points are located in the transition region, where both temperature and mixing conditions are not favorable for combustion.

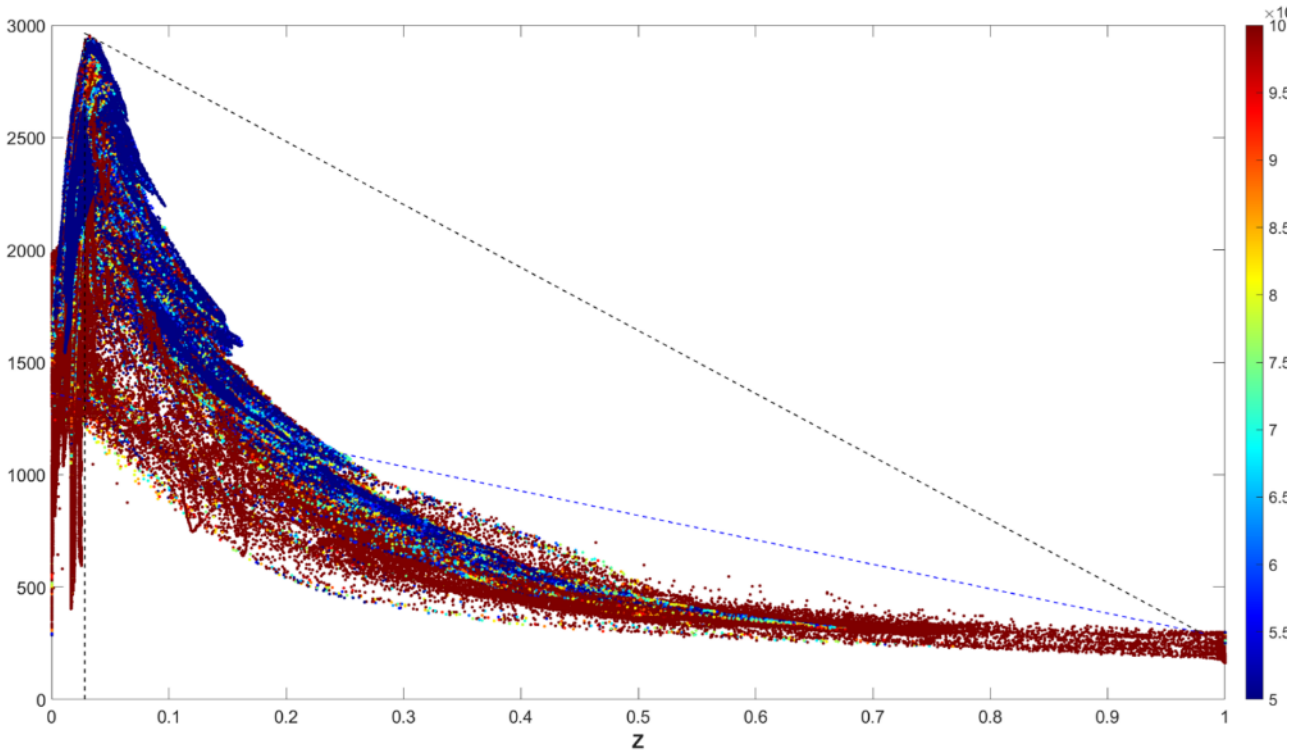


Figure 95 - Scatterplot  $Z,T$ . The markers are colored with the magnitude of the strainrate tensor

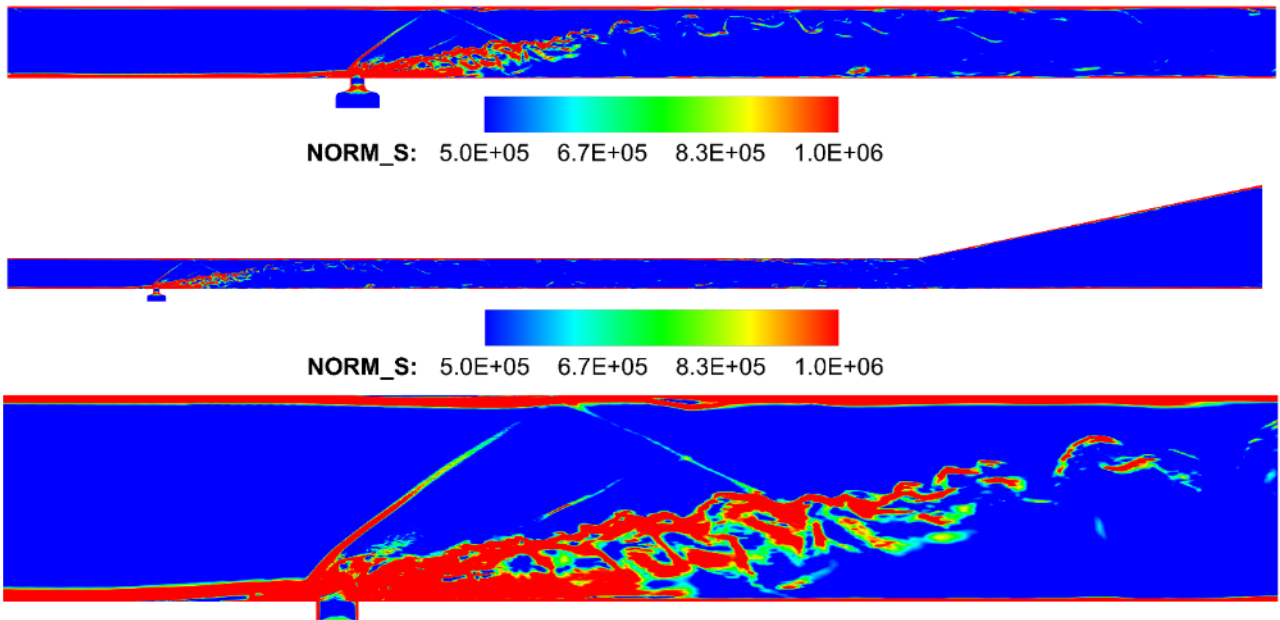


Figure 96 - The Strain rate tensor norm distribution. Top, the first quarter of the combustor; center, the whole combustor; bottom, a particular of the injection section.

## 6.4 Conclusions of chapter 6

Chapter 6 has presented the results of the HyShot II combustor large eddy simulations.

The chapter opens with an overall flow analysis which globally describes the flow field, starting from the air entrance and moving along the combustor, on the symmetry line, toward the expansion nozzle.

The sonic fuel cross-injection interacts with the supersonic air flowing through the combustor generating several shock structures including a closed shock, referred as *barrel shock*, and a  $\lambda$  shaped shock.

The oblique shocks keep reflecting between the body side and the cowl side of the combustor until the expanding nozzle. Before going further, a comparison between the experimental and numerical pressure traces and wall heat-flux measurements was performed. Then, a detailed flow analysis followed.

4 families of vortices, namely the horseshow, the Counterrotating Vortex Pair (CVP), the Kelvin-Helmholtz instability vortices and the  $\Omega$ -shaped vortices, were identified by means of the Q-criterion. They were concentrated in specific region of the domain, going from  $x/D < 5$  to  $x/D \approx 70$ . After such length, at about one quarter of the combustor, the flow loses any coherence becoming fully turbulent. On the basis of this, three flow regions were defined: a near-field region, at  $x/D < 5$ , a transition region, at  $10 < x/D < 20$ , and a fully turbulent region, at  $x/D > 70$ . Each of them is characterized by proper vortices. Such vortices are crucial in ensuring the fuel-air mixing. In virtue of this, a particular attention was paid to the structure proper of the near-field region. The X-vorticity was evaluated in order to quantify the dimension and gather the information about the nature of the vortices composing the horseshow and the CVPs. It was concluded that such structures are responsible for the fuel-air mixing in the near-field region.

Moreover, a Hydrogen recirculation bubble was identified ahead of the injector. Such bubble is recognized to be extremely important in the combustion regime. Indeed, appreciable levels of  $OH$  and  $H_2O$  are found in the bubble.  $OH$  distribution appeared to be not monotone along the combustor. Peak values were recorded in confined regions where the time for mixing was higher, thanks to recirculation phenomena. The inspection of the mass source terms allowed for the identification of the ignition regions, being basically the ones where mixing is possible. The recirculation bubble ahead of the bow shock acts like a radical source and represents a crucial zone for flame and combustion stabilization. Moreover, the Takeno flame index analysis helped to characterize the combustion regime: there are portions of the domain (in the shear layer envelope) where combustion is slightly pre-mixed. Finally, a comparison between the flow-features (namely, temperature and strain rate) against the mixing related one (the mixture fraction) helped to understand the conditions under which auto-ignition occurs.

## 7. Summary and outlook

---

The present work, by means of both numerical and experimental (in minor part) investigations, aimed to provide more insights in understanding the mechanism of ignition and combustion proceeding of an internal combustion engine and a scramjet combustor. After a brief dissertation about the role of combustion and, above all, the need for cleaner combustion systems, in section 1 - *Introduction*, an introduction on the basic principles of combustion modeling is purposed in section 2 - *Fundamentals of combustion modeling*. The next section, 3 - *The experimental data*, describes the experimental setup employed for the engine experimental campaign, conducted by the colleagues of the Istituto Motori CNR di Napoli, and the experiments in the shock tunnel for what concern the scramjet combustor. The acquired engine data were briefly described, highlighting the differences between the two ignition systems. Moreover, the influence of the piston ring on the mass losses was highlighted.

The scramjet data were acquired on the whole vehicle. Thanks to the wide number of installed instruments, it was possible to evaluate the inflow conditions for the combustor, which are employed in the numerical model.

The modelling approaches for the two case-studies are presented in section 4 - *Modeling approach*. Here, the commercial software CONVERGE CFD is introduced, and its features are explained. Then, the two models are described separately. The engines numerical setups are, essentially, equal. They differ only in the definition of some grid density boxes. By one hand, this makes the model more general. By the other, the numerical results were not able to fully match the experimental traces. However, a sufficient agreement, in order to conduce the deeper analysis object of the following chapter, was achieved.

The next two sections describes the numerical results, in particular section 5 - *Engine simulations results* introduces the engine results separately, focusing the attention on the pre-chamber engine. After a discussion about the comparison of the numerical pressure and HRR with the experimental ones, a global analysis is performed. Here the contribution of the pre-chamber on the overall energy balance is highlighted, showing that the pre and the main chamber exchange mass and energy continuously and the energy for the ignition furnished by the pre-chamber is order of magnitude higher than that of a conventional spark-plug. A deep discussion on the main charge ignition mechanism is performed. By evaluating the temperature and the composition of the material ejected from the pre-chamber, it appears that ignition can occur both for thermal and for chemical reasons. However, considering the high velocity of the jet, ignition is delayed, both in space and in time. Namely, the ignition doesn't occur in the vicinity of the pre-chamber and is not "instantaneous". The flow-field is such to excessively stretch the flame bringing it to the extinction, as results from the strain-rate analysis, and the flow velocity is so high that the development of a flame is not possible, as inferred by the Damkohler number computations. Moreover, the TFI index indicates that non-premixed combustion regimes may exist in the early ignition stage.

A particular attention was also paid to the fuel conversion mechanisms and to the pollutant production. Considering the stratification of the charge and the presence of a reburning, interesting observation on the Nitrogen oxides were performed. In particular, it was observed that the rich conditions (in the pre-chamber) and the following reburning can activate the Ammonia pathway and reduce the  $NO_x$  in the pre-chamber. Unfortunately, such effect is negligible in the main chamber.

The emission of both engines were computed and compared, concluding that the pre-chamber engine performs better in terms of emissions (evaluated in  $g/kWh$ ) in respect to the standard engine, except for  $NO_x$ , for which the analyzed dilution ratio is too low to have considerable effects.

Finally a description of the flame shape is performed and a discussion about the comparison of raw

experimental flame images is offered.

Section 6- Scramjet simulations results opens with a global description of the flow-field and of the main phenomena typical of sonic crossflow injection in supersonic flows. Many particular structure (bow shock, barrel shock,  $\lambda$ -shock, Mach disk, vortices of various shape...) are introduced and shown. Moreover, a comparison between the experimental and numerical pressure and wall heat-flux measurements is performed. Then, a more detailed description, with the aid of various visualization, of the vortices families is offered. Going further, the role of such vortices in the mixing between fuel and oxidizer is established. Then, the attention is moved on the combustion regime. Ignition is achieved where favorable conditions of temperature, pressure, mixing and residence time are achieved. By monitoring some species of interest and the overall chemical energy source term, it can be concluded that the crucial regions for the combustion are the recirculation zones: they can enhance the mixing time and have a significant role in ensuring a stable combustion. Indeed, the peak values of the chemical source term and of the combustion products are located in that regions. Similar conclusions arises from the analysis of the chemical species source terms. Moreover, thanks to the Takeno Flame Index, it has been possible to identify region of pre-mixed combustion.

Concluding, this doctoral thesis presented the results obtained with commercially available instruments, thus not providing nothing special in the modelling approach and participating with a restricted contribution to the overall research advancement. The analysis approaches proposed in this work aimed to furnish an insight view of the typical -and, somehow, quite unconventional- phenomena involved in the operation of a pre-chamber engine and of a scramjet combustor by means of numerical simulation. Behind the results presented, the author's sake is purposing food for thought for future works and research on internal combustion engines, scramjets and fluid machinery in general.

## 8. Bibliography

---

- [1] bp, "Full report – Statistical Review of World Energy 2021".
- [2] A. K. Agarwal, "Biofuels (alcohols and biodiesel) applications as fuels for internal combustion engines," *Progress in Energy and Combustion Science*, vol. 33, no. 3, pp. 233–271, Jun. 2007, doi: 10.1016/J.PECS.2006.08.003.
- [3] L. Hentschel, K. Michels, T. Garbe, and M. Hönig, "E-fuels – a central module for future engine design?," Springer Vieweg, Wiesbaden, 2018, pp. 487–489. doi: 10.1007/978-3-658-21015-1\_32.
- [4] A. Ramirez, S. M. Sarathy, and J. Gascon, "CO<sub>2</sub> Derived E-Fuels: Research Trends, Misconceptions, and Future Directions," *Trends in Chemistry*, vol. 2, no. 9. Cell Press, pp. 785–795, Sep. 01, 2020. doi: 10.1016/j.trechm.2020.07.005.
- [5] F. Ausfelder and K. Wagemann, "Power-to-Fuels: E-Fuels as an Important Option for a Climate-Friendly Mobility of the Future," *Chemie Ingenieur Technik*, vol. 92, no. 1–2, pp. 21–30, Jan. 2020, doi: 10.1002/CITE.201900180.
- [6] E. Lindstad, B. Lagemann, A. Rialland, G. M. Gamlem, and A. Valland, "Reduction of maritime GHG emissions and the potential role of E-fuels," *Transportation Research Part D: Transport and Environment*, vol. 101, p. 103075, Dec. 2021, doi: 10.1016/J.TRD.2021.103075.
- [7] S. van Renssen, "The hydrogen solution?," *Nature Climate Change*, vol. 10, no. 9. Nature Research, pp. 799–801, Sep. 01, 2020. doi: 10.1038/s41558-020-0891-0.
- [8] X. Ren, L. Dong, D. Xu, and B. Hu, "Challenges towards hydrogen economy in China," *International Journal of Hydrogen Energy*, vol. 45, no. 59, pp. 34326–34345, Dec. 2020, doi: 10.1016/j.ijhydene.2020.01.163.
- [9] A. Pareek, R. Dom, J. Gupta, J. Chandran, V. Adepur, and P. H. Borse, "Insights into renewable hydrogen energy: Recent advances and prospects," *Materials Science for Energy Technologies*, vol. 3, pp. 319–327, Jan. 2020, doi: 10.1016/j.mset.2019.12.002.
- [10] B. Widera, "Renewable hydrogen implementations for combined energy storage, transportation and stationary applications," *Thermal Science and Engineering Progress*, vol. 16, p. 100460, May 2020, doi: 10.1016/j.tsep.2019.100460.
- [11] A. M. Abdalla, S. Hossain, O. B. Nisfindy, A. T. Azad, M. Dawood, and A. K. Azad, "Hydrogen production, storage, transportation and key challenges with applications: A review," *Energy Conversion and Management*, vol. 165, pp. 602–627, Jun. 2018, doi: 10.1016/J.ENCONMAN.2018.03.088.
- [12] I. Bar-On, R. Kirchain, and R. Roth, "Technical cost analysis for PEM fuel cells," *Journal of Power Sources*, vol. 109, no. 1, pp. 71–75, Jun. 2002, doi: 10.1016/S0378-7753(02)00062-9.
- [13] P. Ahmadi and E. Kjeang, "Realistic simulation of fuel economy and life cycle metrics for hydrogen fuel cell vehicles," *International Journal of Energy Research*, vol. 41, no. 5, pp. 714–727, Apr. 2017, doi: 10.1002/er.3672.
- [14] L. M. Das, *Hydrogen-fueled internal combustion engines*, no. x. Elsevier Ltd., 2016. doi: 10.1016/b978-1-78242-363-8.00007-4.
- [15] Y. Li, W. Gao, P. Zhang, Y. Ye, and Z. Wei, "Effects study of injection strategies on hydrogen-air formation and performance of hydrogen direct injection internal combustion engine," *International Journal of Hydrogen Energy*, vol. 44, no. 47, pp. 26000–26011, 2019, doi: 10.1016/j.ijhydene.2019.08.055.
- [16] R. Amirante, E. Cassone, E. Distaso, and P. Tamburrano, "Overview on recent developments in energy storage: Mechanical, electrochemical and hydrogen technologies," *Energy Conversion and*

- Management*, vol. 132, pp. 372–387, 2017.
- [17] J. O. Abe, A. P. I. Popoola, E. Ajenifuja, and O. M. Popoola, “Hydrogen energy, economy and storage: review and recommendation,” *International Journal of Hydrogen Energy*, vol. 44, no. 29, pp. 15072–15086, 2019.
- [18] R. Amirante, E. Cassone, E. Distaso, and P. Tamburrano, “Overview on recent developments in energy storage: Mechanical, electrochemical and hydrogen technologies,” *Energy Conversion and Management*, vol. 132, pp. 372–387, 2017.
- [19] S. Kuczynski, M. Łaciak, A. Olijnyk, A. Szurlej, and T. Włodek, “Thermodynamic and Technical Issues of Hydrogen and Methane-Hydrogen Mixtures Pipeline Transmission,” *Energies 2019, Vol. 12, Page 569*, vol. 12, no. 3, p. 569, Feb. 2019, doi: 10.3390/EN12030569.
- [20] “European Hydrogen Backbone HOW A DEDICATED HYDROGEN INFRASTRUCTURE CAN BE CREATED,” 2020, Accessed: Nov. 10, 2021. [Online]. Available: <https://transparency.entsog.eu/>
- [21] I. A. Gondal, “Hydrogen integration in power-to-gas networks,” *International Journal of Hydrogen Energy*, vol. 44, no. 3, pp. 1803–1815, Jan. 2019, doi: 10.1016/J.IJHYDENE.2018.11.164.
- [22] J. Runyon *et al.*, “Experimental Analysis of Confinement and Swirl Effects on Premixed CH<sub>4</sub>-H<sub>2</sub> Flame Behavior in a Pressurized Generic Swirl Burner,” *Proceedings of the ASME Turbo Expo*, vol. Part F130041-4B, Aug. 2017, doi: 10.1115/GT2017-64794.
- [23] E. Karlis, Y. Liu, Y. Hardalupas, and A. M. K. P. Taylor, “H<sub>2</sub> enrichment of CH<sub>4</sub> blends in lean premixed gas turbine combustion: An experimental study on effects on flame shape and thermoacoustic oscillation dynamics,” *Fuel*, vol. 254, p. 115524, Oct. 2019, doi: 10.1016/J.FUEL.2019.05.107.
- [24] P. Rajpara, R. Shah, and J. Banerjee, “Effect of hydrogen addition on combustion and emission characteristics of methane fuelled upward swirl can combustor,” *International Journal of Hydrogen Energy*, vol. 43, no. 36, pp. 17505–17519, Sep. 2018, doi: 10.1016/J.IJHYDENE.2018.07.111.
- [25] “HYDROGEN GAS TURBINES”.
- [26] P. Glarborg, J. A. Miller, B. Ruscic, and S. J. Klippenstein, “Modeling nitrogen chemistry in combustion,” *Progress in Energy and Combustion Science*, vol. 67, pp. 31–68, 2018, doi: 10.1016/j.pecs.2018.01.002.
- [27] M. Stefanizzi, T. Capurso, G. Filomeno, M. Torresi, and G. Pascazio, “Recent Combustion Strategies in Gas Turbines for Propulsion and Power Generation toward a Zero-Emissions Future: Fuels, Burners, and Combustion Techniques,” *Energies 2021, Vol. 14, Page 6694*, vol. 14, no. 20, p. 6694, Oct. 2021, doi: 10.3390/EN14206694.
- [28] M. A. Nemitallah, S. S. Rashwan, I. B. Mansir, A. A. Abdelhafez, and M. A. Habib, “Review of Novel Combustion Techniques for Clean Power Production in Gas Turbines,” *Energy and Fuels*, vol. 32, no. 2, pp. 979–1004, Feb. 2018, doi: 10.1021/ACS.ENERGYFUELS.7B03607.
- [29] H. H. W. Funke, N. Beckmann, and S. Abanteriba, “Development and Testing of a FuelFlex Dry-Low-NO<sub>x</sub> Micromix Combustor for Industrial Gas Turbine Applications With Variable Hydrogen Methane Mixtures,” *Proceedings of the ASME Turbo Expo*, vol. 4A-2019, Nov. 2019, doi: 10.1115/GT2019-90095.
- [30] N. O. Kapustin and D. A. Grushevenko, “Long-term electric vehicles outlook and their potential impact on electric grid,” *Energy Policy*, vol. 137, p. 111103, Feb. 2020, doi: 10.1016/j.enpol.2019.111103.
- [31] J. R. Woo, H. Choi, and J. Ahn, “Well-to-wheel analysis of greenhouse gas emissions for electric vehicles based on electricity generation mix: A global perspective,” *Transportation Research Part D: Transport and Environment*, vol. 51, pp. 340–350, Mar. 2017, doi: 10.1016/j.trd.2017.01.005.
- [32] K. V. Singh, H. O. Bansal, and D. Singh, “A comprehensive review on hybrid electric vehicles: architectures and components,” *Journal of Modern Transportation*, vol. 27, no. 2, pp. 77–107, Jun.

2019, doi: 10.1007/s40534-019-0184-3.

- [33] R. D. Reitz *et al.*, "IJER editorial: the future of the internal combustion engine." SAGE Publications Sage UK: London, England, 2020.
- [34] P. K. Senecal and F. Leach, "Diversity in transportation: Why a mix of propulsion technologies is the way forward for the future fleet," *Results in Engineering*, vol. 4, p. 100060, Dec. 2019, doi: 10.1016/j.rineng.2019.100060.
- [35] G. Kalghatgi, "Is it really the end of internal combustion engines and petroleum in transport?," *Appl Energy*, vol. 225, pp. 965–974, 2018.
- [36] R. Amirante, C. Casavola, E. Distaso, and P. Tamburrano, "Towards the Development of the In-Cylinder Pressure Measurement Based on the Strain Gauge Technique for Internal Combustion Engines," *SAE Technical Paper 2015-24-2419*, 2015.
- [37] M. Mofijur, M. G. Rasul, J. Hyde, and M. M. K. Bhuyia, "Role of Biofuels on IC Engines Emission Reduction," *Energy Procedia*, vol. 75, pp. 886–892, Aug. 2015, doi: 10.1016/J.EGYPRO.2015.07.211.
- [38] A. K. Agarwal, "Biofuels (alcohols and biodiesel) applications as fuels for internal combustion engines," *Progress in Energy and Combustion Science*, vol. 33, no. 3, pp. 233–271, Jun. 2007, doi: 10.1016/J.PECS.2006.08.003.
- [39] E. Distaso, R. Amirante, G. Calò, P. De Palma, P. Tamburrano, and R. D. Reitz, "Predicting Lubricant Oil Induced Pre-Ignition Phenomena in Modern Gasoline Engines: the Reduced GasLube Reaction Mechanism," *Fuel*, vol. 281, p. 118709, 2020.
- [40] R. Amirante *et al.*, "Effects of lubricant oil on particulate emissions from port-fuel and direct-injection spark-ignition engines," *International Journal of Engine Research*, vol. 18, no. 5–6, pp. 606–620, 2017, doi: <https://doi.org/10.1177/1468087417706602>.
- [41] R. Amirante *et al.*, "Experimental Investigations on the Sources of Particulate Emission within a Natural Gas Spark-Ignition Engine," *SAE Tech Pap 2017-24-0141*, 2017, doi: <https://doi.org/10.4271/2017-24-0141>.
- [42] E. Distaso, R. Amirante, G. Calò, P. De Palma, P. Tamburrano, and R. D. Reitz, "Investigation of Lubricant Oil influence on Ignition of Gasoline-like Fuels by a Detailed Reaction Mechanism," *Energy Procedia*, vol. 148, pp. 663–670, 2018.
- [43] V. Praveena and M. L. J. Martin, "A review on various after treatment techniques to reduce NOx emissions in a CI engine," *Journal of the Energy Institute*, vol. 91, no. 5. Elsevier B.V., pp. 704–720, Oct. 01, 2018. doi: 10.1016/j.joei.2017.05.010.
- [44] F. Duronio, A. De Vita, A. Montanaro, and C. Villante, "Gasoline direct injection engines--A review of latest technologies and trends. Part 2," *Fuel*, vol. 265, p. 116947, 2020.
- [45] V. Manente, B. Johansson, and Wjjj. Cannella, "Gasoline partially premixed combustion, the future of internal combustion engines?," *International Journal of Engine Research*, vol. 12, no. 3, pp. 194–208, 2011.
- [46] M. Kettner, M. Rothe, A. Velji, U. Spicher, D. Kuhnert, and R. Latsch, "A New Flame Jet Concept to Improve the Inflammation of Lean Burn Mixtures in SI," 2005.
- [47] J. Hwang, C. Bae, J. Park, W. Choe, J. Cha, and S. Woo, "Microwave-assisted plasma ignition in a constant volume combustion chamber," *Combustion and Flame*, vol. 167, pp. 86–96, May 2016.
- [48] T. Briggs, T. Alger, and B. Mangold, "Advanced Ignition Systems Evaluations for High-Dilution SI Engines," *Source: SAE International Journal of Engines*, vol. 7, no. 4, pp. 1802–1807, 2014, doi: 10.2307/26277889.
- [49] T. X. Phuoc, "Laser-induced spark ignition fundamental and applications," *Optics and Lasers in*

- Engineering*, vol. 44, no. 5. Elsevier, pp. 351–397, May 01, 2006. doi: 10.1016/j.optlaseng.2005.03.008.
- [50] D. Bradley, C. G. W. Sheppard, I. M. Suardjaja, and R. Woolley, “Fundamentals of high-energy spark ignition with lasers,” *Combustion and Flame*, vol. 138, no. 1–2, pp. 55–77, Jul. 2004, doi: 10.1016/j.combustflame.2004.04.002.
- [51] T. Briggs, T. Alger, and B. Mangold, “Advanced Ignition Systems Evaluations for High-Dilution SI Engines,” *Source: SAE International Journal of Engines*, vol. 7, no. 4, pp. 1802–1807, 2014, doi: 10.2307/26277889.
- [52] A. Schenk, G. Rixecker, and S. Bohne, “Results from gasoline and CNG engine tests with the corona ignition system EcoFlash,” in *Laser Ignition Conference, LIC 2015*, Apr. 2015, p. W4A.4. doi: 10.1364/lic.2015.w4a.4.
- [53] E. Toulson, H. J. Schock, and W. P. Attard, “A Review of Pre-Chamber Initiated Jet Ignition Combustion Systems,” *SAE Technical Paper Series*, vol. 1, 2010, doi: 10.4271/2010-01-2263.
- [54] C. E. C. Alvarez, G. E. Couto, V. R. Roso, A. B. Thiriet, and R. M. Valle, “A review of prechamber ignition systems as lean combustion technology for SI engines,” *Applied Thermal Engineering*, vol. 128, pp. 107–120, Jan. 2018, doi: 10.1016/J.APPLTHERMALENG.2017.08.118.
- [55] P. Sementa, F. Catapano, S. di Iorio, and B. M. Vaglieco, “Experimental Investigation of a Fueled Prechamber Combustion in an Optical Small Displacement SI Methane Engine,” *SAE Technical Papers*, vol. 2019-Septe, no. September, 2019, doi: 10.4271/2019-24-0170.
- [56] E. Toulson, H. C. Watson, and W. P. Attard, “Modeling Alternative Prechamber Fuels in Jet Assisted Ignition of Gasoline and LPG,” Apr. 2009. doi: 10.4271/2009-01-0721.
- [57] E. Distaso *et al.*, “Analysis of the Combustion Process in a Lean-Burning Turbulent Jet Ignition Engine Fueled with Methane,” *Energy Conversion and Management*, vol. 223, p. 113257, 2020.
- [58] R. Amirante *et al.*, “Effects of natural gas composition on performance and regulated, greenhouse gas and particulate emissions in spark-ignition engines,” *Energy Conversion and Management*, vol. 143, pp. 338–347, 2017, doi: <https://doi.org/10.1016/j.enconman.2017.04.016>.
- [59] G. M. Kosmadakis, D. C. Rakopoulos, J. Arroyo, F. Moreno, M. Muñoz, and C. D. Rakopoulos, “CFD-based method with an improved ignition model for estimating cyclic variability in a spark-ignition engine fueled with methane,” *Energy Convers Manag*, vol. 174, pp. 769–778, 2018.
- [60] R. Amirante, E. Distaso, P. Tamburrano, and R. D. Reitz, “Analytical Correlations for Modeling the Laminar Flame Speed of Natural Gas Surrogate Mixtures,” *Energy Procedia*, vol. 126, pp. 850–857, 2017.
- [61] J. Getzlaff, J. Pape, C. Gruenig, D. Kuhnert, and R. Latsch, “Investigations on pre-chamber spark plug with pilot injection,” Apr. 2007. doi: 10.4271/2007-01-0479.
- [62] J. Vávra, Z. Syrovátka, M. Takáts, and E. Barrientos, “Scavenged Pre-Chamber on a Gas Engine for Light Duty Truck,” in *ASME 2016 Internal Combustion Engine Fall Technical Conference*, Oct. 2016, p. V001T03A014. doi: 10.1115/ICEF2016-9423.
- [63] Z. Syrovatka, O. Vitek, J. Vavra, and M. Takats, “Scavenged pre-chamber volume effect on gas engine performance and emissions,” *SAE Technical Papers*, vol. 2019-April, no. April, pp. 1–17, 2019, doi: 10.4271/2019-01-0258.
- [64] M. Silva, S. Sanal, P. Hlaing, E. Cenker, B. Johansson, and H. G. Im, “Effects of Geometry on Passive Pre-Chamber Combustion Characteristics,” *SAE Technical Papers*, vol. 2020-April, no. April, 2020, doi: 10.4271/2020-01-0821.
- [65] S. Biswas, S. Tanvir, H. Wang, and L. Qiao, “On ignition mechanisms of premixed CH<sub>4</sub>/air and H<sub>2</sub>/air

- using a hot turbulent jet generated by pre-chamber combustion,” *Applied Thermal Engineering*, vol. 106, pp. 925–937, 2016, doi: 10.1016/j.applthermaleng.2016.06.070.
- [66] P. M. Allison, M. de Oliveira, A. Giusti, and E. Mastorakos, “Pre-chamber ignition mechanism: Experiments and simulations on turbulent jet flame structure,” *Fuel*, vol. 230, no. December 2017, pp. 274–281, 2018, doi: 10.1016/j.fuel.2018.05.005.
- [67] F. Qin, A. Shah, Z. wei Huang, L. na Peng, P. Tunestal, and X. S. Bai, “Detailed numerical simulation of transient mixing and combustion of premixed methane/air mixtures in a pre-chamber/main-chamber system relevant to internal combustion engines,” *Combustion and Flame*, vol. 188, pp. 357–366, 2018, doi: 10.1016/j.combustflame.2017.10.006.
- [68] S. A. Tsekenis *et al.*, “Towards in-cylinder chemical species tomography on large-bore IC engines with pre-chamber,” *Flow Measurement and Instrumentation*, vol. 53, pp. 116–125, 2017, doi: 10.1016/j.flowmeasinst.2016.04.006.
- [69] B. Zhang, X. Chang, and C. Bai, “End-wall ignition of methane-air mixtures under the effects of CO<sub>2</sub>/Ar/N<sub>2</sub> fluidic jets,” *Fuel*, vol. 270, p. 117485, 2020.
- [70] Q. Malé, G. Staffelbach, O. Vermorel, A. Misdariis, F. Ravet, and T. Poinso, “Large Eddy Simulation of Pre-Chamber Ignition in an Internal Combustion Engine,” *Flow, Turbulence and Combustion*, 2019, doi: 10.1007/s10494-019-00026-y.
- [71] P. Hlaing *et al.*, “A Study of Lean Burn Pre-Chamber Concept in a Heavy Duty Engine,” pp. 1–13, 2019, doi: 10.4271/2019-24-0107.Abstract.
- [72] L. S. Baumgartner, S. Wohlgemuth, S. Zirngibl, and G. Wachtmeister, “Investigation of a Methane Scavenged Prechamber for Increased Efficiency of a Lean-Burn Natural Gas Engine for Automotive Applications,” *SAE International Journal of Engines*, vol. 8, no. 2, pp. 921–933, 2015, doi: 10.4271/2015-01-0866.
- [73] P. Chinnathambi, M. Bunce, and L. Cruff, “RANS Based Multidimensional Modeling of an Ultra-Lean Burn Pre-Chamber Combustion System with Auxiliary Liquid Gasoline Injection,” *SAE Technical Papers*, vol. 2015-April, no. April, 2015, doi: 10.4271/2015-01-0386.
- [74] E. Shapiro *et al.*, “Experimental and numerical analysis of pre-chamber combustion systems for lean burn gas engines,” in *SAE Technical Papers*, 2019, vol. 2019-April, no. April. doi: 10.4271/2019-01-0260.
- [75] D. Assanis, N. Engineer, P. Neuman, and M. Wooldridge, “Computational Development of a Dual Pre-Chamber Engine Concept for Lean Burn Combustion,” *SAE Technical Papers*, vol. 2016-October, 2016, doi: 10.4271/2016-01-2242.
- [76] J. Urzay, “Supersonic Combustion in Air-Breathing Propulsion Systems for Hypersonic Flight,” *Annual Review of Fluid Mechanics*, vol. 50, no. 1, pp. 593–627, Jan. 2018, doi: 10.1146/annurev-fluid-122316-045217.
- [77] R. Boyce, S. Gerard, and A. Paull, “The HyShot Scramjet Flight Experiment - Flight Data and CFD Calculations Compared,” Dec. 2003. doi: 10.2514/6.2003-7029.
- [78] M. K. Smart, N. E. Hass, and A. Paull, “Flight Data Analysis of the HyShot 2 Scramjet Flight Experiment,” *AIAA Journal*, vol. 44, no. 10, pp. 2366–2375, Oct. 2006, doi: 10.2514/1.20661.
- [79] K. R. Jackson, M. R. Gruber, and S. Buccellato, “Mach 6–8+ Hydrocarbon-Fueled Scramjet Flight Experiment: The HiFiRE Flight 2 Project,” *Journal of Propulsion and Power*, vol. 31, no. 1, pp. 36–53, Jan. 2015, doi: 10.2514/1.B35350.
- [80] J. Steelant, R. Varvill, C. Walton, S. Defoort, K. Hannemann, and M. Marini, “Achievements Obtained for Sustained Hypersonic Flight within the LAPCAT-II project,” Jul. 2015. doi: 10.2514/6.2015-3677.

- [81] A. Vincent-Randonnier, V. Sabelnikov, A. Ristori, N. Zettervall, and C. Fureby, "An experimental and computational study of hydrogen–air combustion in the LAPCAT II supersonic combustor," *Proceedings of the Combustion Institute*, vol. 37, no. 3, pp. 3703–3711, Jan. 2019, doi: 10.1016/J.PROCI.2018.05.127.
- [82] K. Nordin-Bates, C. Fureby, S. Karl, and K. Hannemann, "Understanding scramjet combustion using LES of the HyShot II combustor," *Proceedings of the Combustion Institute*, vol. 36, no. 2, pp. 2893–2900, Jan. 2017, doi: 10.1016/J.PROCI.2016.07.118.
- [83] "CONVERGECFD MANUAL SERIES CONVERGE MANUAL v3.0," 2021.
- [84] R. I. Issa, "Solution of the implicitly discretised fluid flow equations by operator-splitting," *Journal of Computational Physics*, vol. 62, no. 1, pp. 40–65, Jan. 1986, doi: 10.1016/0021-9991(86)90099-9.
- [85] V. Yakhot and S. A. Orszag, "Renormalization group analysis of turbulence. I. Basic theory," *Journal of Scientific Computing*, vol. 1, no. 1, pp. 3–51, 1986, doi: 10.1007/BF01061452.
- [86] J. Smargorinsky, "General circulation experiment with the primitive equations," *Monthly Weather Review*, vol. 91, no. 3, pp. 99–164, 1963, doi: 10.1175/1520-0493.
- [87] M. Germano, U. Piomelli, P. Moin, and W. H. Cabot, "A dynamic subgrid-scale eddy viscosity model," *Physics of Fluids A: Fluid Dynamics*, vol. 3, no. 7, pp. 1760–1765, Jul. 1991, doi: 10.1063/1.857955.
- [88] D. K. Lilly, "A proposed modification of the Germano subgrid-scale closure method," *Physics of Fluids A: Fluid Dynamics*, vol. 4, no. 3, p. 633, Sep. 1998, doi: 10.1063/1.858280.
- [89] Z. Tan and R. D. Reitz, "An ignition and combustion model based on the level-set method for spark ignition engine multidimensional modeling," *Combustion and Flame*, vol. 145, no. 1–2, pp. 1–15, Apr. 2006, doi: 10.1016/J.COMBUSTFLAME.2005.12.007.
- [90] P. K. Senecal *et al.*, "Multi-Dimensional Modeling of Direct-Injection Diesel Spray Liquid Length and Flame Lift-off Length using CFD and Parallel Detailed Chemistry," *SAE Transactions*, vol. 112. SAE International, pp. 1331–1351, 2003. doi: 10.2307/44741357.
- [91] J. Warnatz, U. (Ulrich) Maas, and R. W. Dibble, *Combustion : physical and chemical fundamentals, modeling and simulation, experiments, pollutant formation*. Springer, 2010.
- [92] N. Peters, *Turbulent combustion*. Cambridge university press, 2000.
- [93] R. Amirante, E. Distaso, P. Tamburrano, and R. D. Reitz, "Laminar flame speed correlations for methane, ethane, propane and their mixtures, and natural gas and gasoline for spark-ignition engine simulations," *International Journal of Engine Research*, vol. 18, no. 9, pp. 951–970, Nov. 2017, doi: 10.1177/1468087417720018.
- [94] J. Heywood, *Internal Combustion Engine Fundamentals 2E*. 2018. Accessed: Jan. 13, 2020. [Online]. Available: <https://www.accessengineeringlibrary.com/browse/internal-combustion-engine-fundamentals-second-edition>
- [95] E. Distaso *et al.*, "Experimental and Numerical Analysis of a Pre-Chamber Turbulent Jet Ignition Combustion System," *SAE Technical paper 2019-24-0018*, 2019, doi: <https://doi.org/10.4271/2019-24-0018>.
- [96] A. Paull, H. Alesi, and S. Anderson, "HyShot flight program and how it was developed," *AIAA Paper*, vol. 5248, p. 2002, 2002.
- [97] K. Hannemann, S. Karl, J. M. Schramm, and J. Steelant, "Methodology of a combined ground based testing and numerical modelling analysis of supersonic combustion flow paths," *Shock Waves*, vol. 20, no. 5, pp. 353–366, 2010, doi: 10.1007/s00193-010-0269-8.
- [98] K. Hannemann, J. M. Schramm, S. Karl, and J. Steelant, "Experimental investigation of different scramjet hydrogen injection systems," *European Space Agency, (Special Publication) ESA SP*, vol. 659

SP, no. November 2008, pp. 3–6, 2009.

- [99] C. Fureby, M. Chapuis, E. Fedina, and S. Karl, “CFD analysis of the HyShot II scramjet combustor,” *Proceedings of the Combustion Institute*, vol. 33, no. 2, pp. 2399–2405, 2011, doi: 10.1016/j.proci.2010.07.055.
- [100] E. Pomraning, K. Richards, and P. K. Senecal, “Modeling turbulent combustion using a rans model, detailed chemistry, and adaptive mesh refinement,” in *SAE Technical Papers*, Apr. 2014, vol. 1. doi: 10.4271/2014-01-1116.
- [101] Z. Q. Gregory P. Smith, David M. Golden, Michael Frenklach, Nigel W. Moriarty, Boris Eiteneer, Mikhail Goldenberg, C. Thomas Bowman, Ronald K. Hanson, Soonho Song, William C. Gardiner, Jr., Vitali V. Lissianski, “GRI-Mech 3.0.” <http://combustion.berkeley.edu/gri-mech/version30/text30.html#cite> (accessed Apr. 27, 2019).
- [102] D. D. Thomsen, F. F. Kuligowski, and N. M. Laurendeau, “Modeling of NO formation in premixed, high-pressure methane flames,” *Combustion and Flame*, vol. 119, no. 3, pp. 307–318, Nov. 1999, doi: 10.1016/S0010-2180(99)00062-0.
- [103] J. Luque, G. P. Smith, and D. R. Crosley, “Quantitative CH determinations in low-pressure flames,” *Symposium (International) on Combustion*, vol. 26, no. 1, pp. 959–966, Jan. 1996, doi: 10.1016/S0082-0784(96)80308-0.
- [104] A. C. A. Lipardi, P. Versailles, G. M. G. Watson, G. Bourque, and J. M. Bergthorson, “Experimental and numerical study on NO<sub>x</sub> formation in CH<sub>4</sub>–air mixtures diluted with exhaust gas components,” *Combustion and Flame*, vol. 179, pp. 325–337, May 2017, doi: 10.1016/j.combustflame.2017.02.009.
- [105] G. Xu, Y. M. Wright, M. Schiliro, and K. Boulouchos, “Characterization of combustion in a gas engine ignited using a small un-scavenged pre-chamber,” *International Journal of Engine Research*, vol. 21, no. 7, pp. 1085–1106, Sep. 2020, doi: 10.1177/1468087418798918.
- [106] M. Namazian and J. B. Heywood, “Flow in the Piston-Cylinder-Ring Crevices of a Spark-Ignition Engine: Effect on Hydrocarbon Emissions, Efficiency and Power,” *SAE Transactions*, vol. 91. SAE International, pp. 261–288, 1982. doi: 10.2307/44631945.
- [107] H. Werner and H. Wengle, “Large-Eddy Simulation of Turbulent Flow Over and Around a Cube in a Plate Channel,” *Turbulent Shear Flows 8*, pp. 155–168, 1993, doi: 10.1007/978-3-642-77674-8\_12.
- [108] M. Ó Conaire, H. J. Curran, J. M. Simmie, W. J. Pitz, and C. K. Westbrook, “A comprehensive modeling study of hydrogen oxidation,” *International Journal of Chemical Kinetics*, vol. 36, no. 11, pp. 603–622, Nov. 2004, doi: 10.1002/kin.20036.
- [109] M. Fathi, R. Khoshbakhti Saray, and M. David Checkel, “Detailed approach for apparent heat release analysis in HCCI engines,” *Fuel*, vol. 89, no. 9, pp. 2323–2330, Sep. 2010, doi: 10.1016/j.fuel.2010.04.030.
- [110] S. Biswas, *Physics of turbulent jet ignition : mechanisms and dynamics of ultra-lean combustion*. 2018.
- [111] W. P. Attard, N. Fraser, P. Parsons, and E. Toulson, “A Turbulent Jet Ignition Pre-Chamber Combustion System for Large Fuel Economy Improvements in a Modern Vehicle Powertrain,” *SAE International Journal of Engines*, vol. 3, no. 2, pp. 20–37, 2010, doi: 10.4271/2010-01-1457.
- [112] X. Yang, Y. Cheng, and P. Wang, “The scavenging timing of pre-chamber on the performance of a natural gas engine,” *International Journal of Engine Research*, 2020, doi: 10.1177/1468087420960876.
- [113] N. D. S. A. Santos, C. E. C. Alvarez, V. R. Roso, J. G. C. Baeta, and R. M. Valle, “Lambda load control in spark ignition engines, a new application of prechamber ignition systems,” *Energy Conversion and Management*, vol. 236, p. 114018, May 2021, doi: 10.1016/j.enconman.2021.114018.

- [114] Y. Ikeda, J. Kojima, and T. Nakajima, "Local Damköler number measurement in turbulent methane/air flames by local OH\*, CH\* and C2\* chemiluminescence," Jul. 2000. doi: 10.2514/6.2000-3395.
- [115] J. Heywood, *Internal Combustion Engine Fundamentals 2E*. 2018.
- [116] N. Wang, J. Liu, W. L. Chang, and C. fon Lee, "A numerical study of the combustion and jet characteristics of a hydrogen fueled turbulent hot-jet ignition (THJI) chamber," *International Journal of Hydrogen Energy*, vol. 43, no. 45, pp. 21102–21113, Nov. 2018, doi: 10.1016/j.ijhydene.2018.09.156.
- [117] A. M. Steinberg, B. Coriton, and J. H. Frank, "Influence of combustion on principal strain-rate transport in turbulent premixed flames," *Proceedings of the Combustion Institute*, vol. 35, no. 2, pp. 1287–1294, Jan. 2015, doi: 10.1016/j.proci.2014.06.089.
- [118] H. S. Kim and H. Pitsch, "Scalar gradient and small-scale structure in turbulent premixed combustion," *Physics of Fluids*, vol. 19, no. 11, pp. 1–15, 2007, doi: 10.1063/1.2784943.
- [119] B. Higgins, M. Q. McQuay, F. Lacas, and S. Candel, "An experimental study on the effect of pressure and strain rate on CH chemiluminescence of premixed fuel-lean methane/air flames," *Fuel*, vol. 80, no. 11, pp. 1583–1591, Sep. 2001, doi: 10.1016/S0016-2361(01)00040-0.
- [120] B. Coriton, J. H. Frank, and A. Gomez, "Effects of strain rate, turbulence, reactant stoichiometry and heat losses on the interaction of turbulent premixed flames with stoichiometric counterflowing combustion products," *Combustion and Flame*, vol. 160, no. 11, pp. 2442–2456, Nov. 2013, doi: 10.1016/j.combustflame.2013.05.009.
- [121] and F. E. M. Darabiha, N., S. M. Candel, "The effect of strain rate on a premixed laminar flame," *Combust Flame*, vol. 64, 1986.
- [122] A. M. Steinberg, B. Coriton, and J. H. Frank, "Influence of combustion on principal strain-rate transport in turbulent premixed flames," *Proceedings of the Combustion Institute*, vol. 35, no. 2, pp. 1287–1294, Jan. 2015, doi: 10.1016/j.proci.2014.06.089.
- [123] B. Coriton, J. H. Frank, and A. Gomez, "Effects of strain rate, turbulence, reactant stoichiometry and heat losses on the interaction of turbulent premixed flames with stoichiometric counterflowing combustion products," *Combustion and Flame*, vol. 160, no. 11, pp. 2442–2456, Nov. 2013, doi: 10.1016/j.combustflame.2013.05.009.
- [124] H. Yamashita, M. Shimada, and T. Takeno, "A numerical study on flame stability at the transition point of jet diffusion flames," *Symposium (International) on Combustion*, vol. 26, no. 1, pp. 27–34, Jan. 1996, doi: 10.1016/S0082-0784(96)80196-2.
- [125] Y. An, M. Jaasim, V. Raman, F. E. Hernández Pérez, H. G. Im, and B. Johansson, "Homogeneous charge compression ignition (HCCI) and partially premixed combustion (PPC) in compression ignition engine with low octane gasoline," *Energy*, vol. 158, pp. 181–191, Sep. 2018, doi: 10.1016/j.energy.2018.06.057.
- [126] P. Kilpinen, M. Hupa, and P. Glarborg, "Reburning Chemistry: A Kinetic Modeling Study," *Industrial and Engineering Chemistry Research*, vol. 31, no. 6, pp. 1477–1490, 1992, doi: 10.1021/ie00006a009.
- [127] M. Fikri, S. Meyer, J. Roggenbuck, and F. Temps, "An experimental and theoretical study of the product distribution of the reaction (Equation presented)," *Faraday Discussions*, vol. 119, no. 1, pp. 223–242, Nov. 2002, doi: 10.1039/b102563p.
- [128] W. Feng and J. F. Hershberger, "Experimental and theoretical study of the product channels of the C<sub>2</sub>H + NO reaction," *Journal of Physical Chemistry A*, vol. 117, no. 17, pp. 3585–3592, May 2013, doi: 10.1021/jp401354x.
- [129] R. Dahms, T. D. Fansler, M. C. Drake, T. W. Kuo, A. M. Lippert, and N. Peters, "Modeling ignition

- phenomena in spray-guided spark-ignited engines," *Proceedings of the Combustion Institute*, vol. 32, no. 2, pp. 2743–2750, Jan. 2009, doi: 10.1016/J.PROCI.2008.05.052.
- [130] J. C. G. Andrae and T. Kovács, "Evaluation of Adding an Olefin to Mixtures of Primary Reference Fuels and Toluene to Model the Oxidation of a Fully Blended Gasoline," *Energy and Fuels*, vol. 30, no. 9, pp. 7721–7730, Sep. 2016, doi: 10.1021/ACS.ENERGYFUELS.6B01193/SUPPL\_FILE/EF6B01193\_SI\_004.TXT.
- [131] M. Zhao, T. Ye, C. Cao, T. Zhou, and M. Zhu, "Study of sonic injection from circular injector into a supersonic cross-flow using large eddy simulation," *International Journal of Hydrogen Energy*, vol. 41, no. 39, pp. 17657–17669, Oct. 2016, doi: 10.1016/j.ijhydene.2016.07.018.
- [132] M. Chapuis, E. Fedina, C. Fureby, K. Hannemann, S. Karl, and J. Martinez Schramm, "A computational study of the HyShot II combustor performance," *Proceedings of the Combustion Institute*, vol. 34, no. 2, pp. 2101–2109, Jan. 2013, doi: 10.1016/J.PROCI.2012.07.014.
- [133] M. Chapuis, E. Fedina, C. Fureby, K. Hannemann, S. Karl, and J. Martinez Schramm, "A computational study of the HyShot II combustor performance," *Proceedings of the Combustion Institute*, vol. 34, no. 2, pp. 2101–2109, 2013, doi: 10.1016/j.proci.2012.07.014.
- [134] A. Ben-Yakar, "EXPERIMENTAL INVESTIGATION OF MIXING AND IGNITION OF TRANSVERSE JETS IN SUPERSONIC CROSSFLOWS," 2000.
- [135] Y. You, H. Luedeke, and K. Hannemann, "Injection and mixing in a scramjet combustor: DES and RANS studies," *Proceedings of the Combustion Institute*, vol. 34, no. 2, pp. 2083–2092, Jan. 2013, doi: 10.1016/J.PROCI.2012.10.001.
- [136] Y. You, H. Luedeke, and K. Hannemann, "Injection and mixing in a scramjet combustor: Des and RANS studies," *Proceedings of the Combustion Institute*, vol. 34, no. 2, pp. 2083–2092, 2013, doi: 10.1016/j.proci.2012.10.001.
- [137] X. Chai, P. S. Iyer, and K. Mahesh, "Numerical study of high speed jets in crossflow," *J. Spacecr. Rockets*, vol. 785, no. 2, pp. 1658–1665, 2015, doi: 10.1017/jfm.2015.612.
- [138] Z. bo Du, W. Huang, L. Yan, L. quan Li, Z. Chen, and S. bin Li, "RANS study of steady and pulsed gaseous jets into a supersonic crossflow," *International Journal of Heat and Mass Transfer*, vol. 136, pp. 157–169, Jun. 2019, doi: 10.1016/j.ijheatmasstransfer.2019.02.103.
- [139] W. Huang, Z. bo Du, L. Yan, and Z. xun Xia, "Supersonic mixing in airbreathing propulsion systems for hypersonic flights," *Progress in Aerospace Sciences*, vol. 109. Elsevier Ltd, Aug. 01, 2019. doi: 10.1016/j.paerosci.2019.05.005.
- [140] A. Ben-Yakar, M. G. Mungal, and R. K. Hanson, "Time evolution and mixing characteristics of hydrogen and ethylene transverse jets in supersonic crossflows," 2006, doi: 10.1063/1.2139684.
- [141] F. Vergine, L. Maddalena, V. Miller, and M. Gamba, "Supersonic Combustion and Flame-Holding Characteristics of Pylon Injected Hydrogen in a Mach 2.4 High Enthalpy Flow," 2012.